Title
Fundamental Study on Nanoparticle Interaction with Hot Crack Susceptible Aluminum Alloys during Arc Welding

Author
Sokoluk, Maximilian

Publication Date
2020

Peer reviewed|Thesis/dissertation

UNIVERSITY OF CALIFORNIA

Los Angeles

Fundamental Study on Nanoparticle Interaction with Hot Crack Susceptible Aluminum Alloys during Arc Welding

A dissertation submitted in partial satisfaction of the

requirements for the degree Doctor of Philosophy

in Mechanical Engineering

by

Maximilian Sokoluk

2020

ABSTRACT OF THE DISSERTATION

Fundamental Study on Nanoparticle Interaction with

Hot Crack Susceptible Aluminum Alloys during Arc Welding

by

Maximilian Sokoluk

Doctor of Philosophy in Mechanical Engineering

University of California, Los Angeles, 2020

Professor Xiaochun Li, Chair

In today's society, the manufacturing of complex structures and assemblies is of vital importance in the design and engineering process. In this context, fusion welding has proven to be an invaluable method from large scale automotive assembly lines to high tech aerospace applications. With the growing call for energy-efficient solutions, the demand for high strength aluminum alloys in these applications is evident. Therefore, when incorporating these materials into profitable production processes, a material‘s weldability becomes crucial.

While high strength aluminum alloys such as AA7075 and AA2024 are considered unweldable due to their high susceptibility to hot cracking, the medium strength AA6061 is only weldable with limitations. The dissimilar filler metals used to mitigate hot crack susceptibility leave the weld metal with limited strength, ductility, corrosion resistance, and heat treatability.

Therefore, this study aims to eliminate the intrinsic susceptibility of introduced aluminum alloys using filler metal of similar chemical composition treated with refractory nanoparticles, i.e., nano-treating (NT). Filler metal containing a volume fraction of 0.8 v% of TiC (7075NT-C, 2024NT-C, and 6061NT-C) and a volume fraction of 0.8 v% TiB_2 (7075NT-B, 2024NT-B, and 6061NT-B) nanoparticles were produced, matching the constituent element composition of their respective commercial aluminum alloys. In addition, the industrially applied filler metal ER5356 was nano-treated with 0.8 v% TiC (5356NT-C) and 0.8 v% TiB_2 (5356NT-B), respectively. The welds performed with similar nano-treated filler metal showed a remarkable grain refinement and morphology control, whereas the use of TiC-containing filler metals was deemed more effective than their TiB_2 -bearing counterparts.

The transversal tensile properties of the welded joints showed an increased weld metal hardness in as-welded condition and virtually wrought transversal tensile properties by applying a post-weld heat treatment to the specimens.

The Houldcroft hot crack susceptibility tests conducted showed a significant reduction in the weld metals' susceptibility to hot cracking when comparing tests performed with nano-treated filler metal to tests performed with the respective base metal as filler metal. It was noted that the crack reduction achieved with NT-C filler metal slightly exceeded that of tests performed with NT-B.

An in-depth thermal analysis investigating the solidification behavior of nano-treated alloys revealed a three-fold mechanism caused by the refractory nanoparticles. It was shown that nanoparticles significantly alter an aluminum alloys solidification process from liquidus to solidus temperature and cause unprecedentet changes to the materials resultant microstructure. This new finding strongly contradicts observations made with the use of conventional grain refiners and mitigate an aluminum alloys susceptibility to hot cracking.

The dissertation of Maximilian Sokoluk is approved.

Tsu-Chin Tsao

Rajit Gadh

Yongjie Hu

Xiaochun Li, Committee Chair

University of California, Los Angeles

2020

To my parents for their unconditional love and support.

Table of Contents

Acknowledgments

First and foremost, I want to express my deepest gratitude to my advisor Professor Xiaochun Li, for his guidance throughout my Ph.D. journey. Without his continuous motivation, scientific rigor, and resources made available to me, this work would not have been possible. I am grateful for the opportunity to work in his lab and the knowledge that was shared with me.

I also have to sincerely thank Professors Tsu-Chin Tsao, Rajit Gadh, and Yongjie Hu for serving on my doctoral committee. I truly appreciated their valuable insights by evaluating my research from a diverse perspective.

I am also grateful to my colleagues and friends in this research group. I could not have asked for a more supportive and caring group of people to accompany me on this journey.

I am thankful for Benjamin Tan’s and Travis Widick’s technical support and valuable discussions regarding my research.

Lastly, I want to thank Valentina for her understanding and invaluable support throughout this challenging time.

Vita

2016, Dipl. Ing. Mechanical Engineering, Karlsruhe Institute of Technology, Germany

Publications

- Sokoluk, Maximilian; Cao, Chezheng; Pan, Shuaihang; Li, Xiaochun (2019): *Nanoparticle-enabled phase control for arc welding of unweldable aluminum alloy 7075*. In *Nature communications* 10 (1). DOI: 10.1038/s41467-018-07989-y.
- Sokoluk, Maximilian; Yao, Gongcheng; Pan, Shuaihang; Cao, Chezheng; Li, Xiaochun (2020): *High Strength Nanotreated Filler Material for TIG Welding of AA6061*. In Alan Tomsett (Ed.): *Light Metals 2020*. Cham: Springer International Publishing (The Minerals, Metals & Materials Series), pp. 380–385.
- Li, Xiaochun; Sokoluk, Maximilian (2020): *Nanotechnology in The Welding of High-Strength Aluminum Alloys*. In *Welding Journal* 99 (3), 28-31
- Zuo, Min; Sokoluk, Maximilian; Cao, Chezheng; Yuan, Jie; Zheng, Shiqi; Li, Xiaochun (2019): *Microstructure Control and Performance Evolution of Aluminum Alloy 7075 by Nano-Treating*. In *Scientific reports* 9 (1), p. 10671. DOI: 10.1038/s41598-019-47182-9.
- Pan, S., Sokoluk, M., Cao, C., Guan, Z., & Li, X. (2019). *Facile fabrication and enhanced properties of Cu-40 wt% Zn/WC nanocomposite.* In *Journal of Alloys and Compounds.* doi:10.1016/j.jallcom.2019.01.022
- Zheng, Shiqi; Sokoluk, Maximillian; Yao, Gongcheng; Rosa, Igor de; Li, Xiaochun (2019): *Fe–Ni Invar alloy reinforced by WC nanoparticles with high strength and low thermal expansion*. In *SN Appl. Sci.* 1 (2), p. 783. DOI: 10.1007/s42452-019-0182-4.
- Lin, T., Cao, C., Sokoluk, M. *et al. Aluminum with dispersed nanoparticles by laser additive manufacturing*. In *Nature communications* **10,** 4124 (2019). https://doi.org/10.1038/s41467-019-12047-2
- Pan, S., Yao, G., Sokoluk, M., Guan, Z., & Li, X. (2019). *Enhanced thermal stability in Cu-40 wt% Zn/WC nanocomposite*. In *Materials & Design*, 180, 107964. doi:10.1016/j.matdes.2019.107964
- Cao, C., Yao, G., Sokoluk, M., & Li, X. (2020). *Molten salt-assisted processing of nanoparticle-reinforced Cu. Materials Science and Engineering: A, 139345.* doi:10.1016/j.msea.2020.139345
- Cao, C., Yao, G., Jiang, L., Sokoluk, M., Wang, X., Ciston, J., *et al.* (2019). *Bulk ultrafine grained/nanocrystalline metals via slow cooling. Science Advances, 5(8), eaaw2398.* doi:10.1126/sciadv.aaw2398

- Pan, S., Saso, T., Yu, N., Sokoluk, M., Yao, G., Umehara, N., & Li, X. (2020*). New study on tribological performance of AA7075-TiB2 nanocomposites*. Tribology International, 106565. doi:10.1016/j.triboint.2020.106565
- Pan, S., Yao, G., Yuan, J., Sokoluk, M., & Li, X. (2020). *Manufacturing of Bulk Al-12Zn-3.7Mg-1Cu Alloy with TiC Nanoparticles.* In *Procedia Manufacturing* Volume 48, 2020, Pages 325-331
- Pan, S., Yuan, J., Zhang, P., Sokoluk, M., Yao, G., & Li, X. (2020). *Effect of electron concentration on electrical conductivity in in situ Al-TiB2 nanocomposites. Applied Physics Letters, 116(1), 014102.* doi:10.1063/1.5129817
- Yuan, J., Zuo, M., Sokoluk, M., Yao, G., Pan, S., & Li, X. J. (2020). *Nanotreating High-Zinc Al–Zn–Mg–Cu Alloy by TiC Nanoparticles*. In *Light metals 2020*., 318-323.
- Hu, Z., Pozuelo, M., Sokoluk, M., Mathaudhu, S., Roach, C., Li, X., & Yang, J.-M. (2019). *Micro-mechanical properties of homogeneous- and inhomogeneous-structured pillars in Al–TiC nanocomposite: An in-situ study.* In *Materials Science and Engineering: A, 762, 138084.* doi:10.1016/j.msea.2019.138084
- Hu, Z., Cao, C., Pozuelo, M., Sokoluk, M., Yang, J.-M., & Li, X. (2019). *Microstructure Formation and Micropillar Compression of Al-TiC Nanocomposite Manufactured by Solidification Nanoprocessing.* In *Metallurgical and Materials Transactions A.* doi:10.1007/s11661-019-05389-5
- Pan, S., Yao, G., Guan, Z., Yu, N., Sokoluk, M. and Li, X., (2020). *Kinetics and dynamics of surface thermal oxidation in Al-ZrB2 nanocomposites*. In *Corrosion Science*, p.108890.
- Yao, G.; Cao, C.; Pan, S., Cao, Chezheng; Sokoluk, M.; Li, X (2019) *High-performance copper reinforced with dispersed nanoparticles.* In *J Mater Sci* **54,** 4423–4432. https://doi.org/10.1007/s10853-018-3152-0

1 Introduction

1.1. Background and Motivation

Engineering is not an exact science. It is more the pursuit to model and control unclear and highly complex systems while keeping the error as small as possible. However, these models are often but a rough approximation of the reality they are destined to conquer. Modern manufacturing processes are assembling structural devices using a variety of techniques to mate parts to an assembly, such as clinching, bolting, riveting, brazing, and welding. The right choice of techniques when designing structural assemblies is of paramount importance in many ways. Bolting, for example, is one of the most predictable mating processes available.

In contrast, its application is limited due to its enormous cost in assembly lines and its additional design effort. Welding alternatively requires minimum effort in design and causes a fraction of the cost in assembly, while process control becomes a challenge. It is astonishing that within the field of manufacturing, arc welding of metals is amongst the most challenging fusion processes to predict while being widely applied in today's industry.

According to a market survey published in January 2017, the overall welding market was estimated at 20.67 billion U.S dollars in 2016 and is expected to reach USD 32.63 billion in 2022, which connotes a market growth of 7.5% between 2017 and 2022 [1]. It is of great interest to further improve the controllability and safety of existing welding processes or expand the range of weldable materials to afore considered unweldable materials to accelerate this shown trend.

Heat treatable high strength Aluminum alloys are notorious for their susceptibility to crack during arc welding. Due to their high strength to weight ratio, these materials, especially the 2000 and 7000 series, find broad application in today's aerospace industry [2]. Figure 1 shows the percentage of aluminum content used in Boeing's airplane range. Although at first glance, resin-fiber composites are thought to be the preferable material for wing and fuselage structures due to their high specific strength, the matter is deemed to be more complicated. For their higher certification and production costs, relatively low resistance to impact, complicated mechanical behavior caused by changes in environmental conditions (moisture absorption, softening, or embrittlement when exposed to hot/cold environments), and difficulty to repair, composites are a double-edged sword.

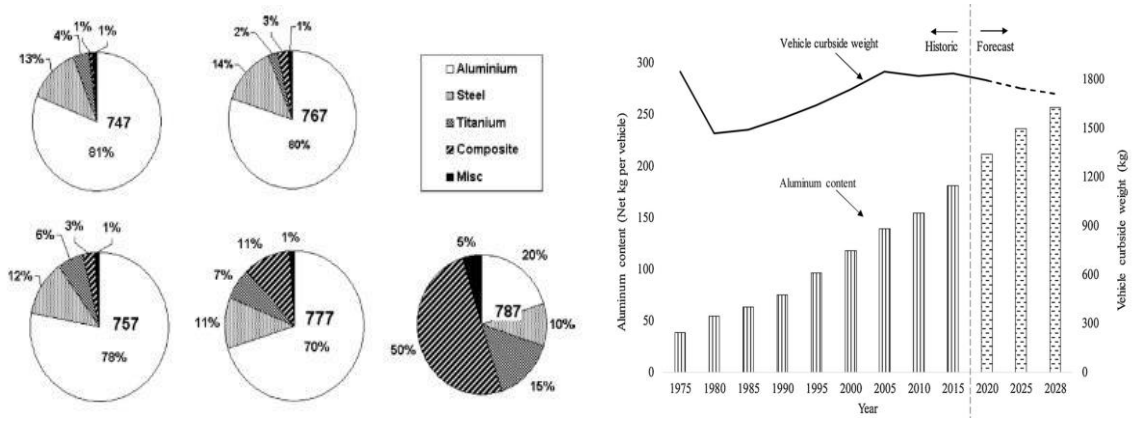

Figure 1 Combination of materials used in Boeing aircraft (left) [2] and aluminum used in the automotive industry (right) [3]

Figure 1 further shows a massive demand increase in aluminum alloys within the automotive industry. Due to stricter environmental regulation and the need to compensate for heavy battery technology in electric vehicles, an 75 % increased demand in aluminum from 2015 to 2028 is forecasted. It is commonly accepted that with appropriate design measures, 1 kg of aluminum can replace 2 kg of steel in automotive structures.

In the U.S., transportation accounts for approximately 28 % of the country's energy consumption, with most of the energy derived from fossil fuels. A detailed model correlating the weight of a vehicle with its fuel consumption concluded that a 10% reduction in weight results in a 6.9% improved fuel economy for cars and a 7.6% improvement in fuel economy for light trucks. [4].

These industries strongly rely on riveting and bolting, while for other, weldable materials, mainly Gas Tungsten Arc Welding (GTAW) and Gas Metal Arc Welding (GMAW) is applied to join these materials to an assembly. The process of GTAW is widely spread in today's high-tech applications such as aerospace and nuclear industry and is extensively used in the fabrication of spacecraft [5]. Even though its throughput is slower than GMAW, the increased controllability of the arc and more precise heat input make it more suitable for the high-quality requirements of this industry. It is therefore understandable that a significant amount of research has been conducted in order to understand and mitigate the hot crack susceptibility of high strength aluminum alloys, especially AA7075 and AA2024. [6–9,9–11].

Moreover, due to good mechanical properties, corrosion resistance, and extrudability, 6000 series aluminum alloys, such as aluminum alloy (AA) 6061 and AA6063, are extensively used in architectural, structural, automotive, and transportation industries [12,13]. While the crack susceptibility of these alloys can be controlled with the use of dissimilar filler metals, this practice comes with drawbacks regarding mechanical properties, heat treatability, and corrosion performance of the welded joint.

Lately, a new approach has been introduced to manipulate weld behavior in GTAW. With an increasing understanding of the effects of nanoparticles on the properties, and especially the solidification behavior of metals, filler metals containing nano reinforcements have been studied [14–20]. These filler metals commonly seek to enhance the properties of the melt zone material. However, nanoparticles are not only known to enhance the properties of the

resultant metal matrix nanocomposite (MMNC) but strongly influence grain growth and solid fraction of alloys while solidifying, as well as viscosity and thermal properties of the melt [21,22]. Choi et al. discovered positive effects of nanoparticle addition on a hot tear susceptible cast aluminum alloy. In light of this, the introduction of MMNC filler wires to GTAW welding of generally considered unweldable aluminum alloys can have so far unprecedented impact on the weldability of this material. It is therefore of great need to study the solidification mechanics of aluminum alloy nanocomposites in general, as well as the application of a nanocomposite filler wire in GTAW of hot crack susceptible aluminum alloys. Solving the intrinsic hot crack susceptibility of high strength aluminum alloys such as AA7075, AA2024, and AA6061 aluminum alloys with this rather simple twist in the overall process could open a tremendous opportunity for the manufacturing capabilities of these materials.

1.2. Research objectives

The objectives of this study include: (1) Investigating the use of nanoparticle enhanced filler metal of similar composition in the arc welding of hot crack susceptible aluminum alloys. Specifically, investigate the change in grain morphology of the weld metal, the mechanical properties of welded joints, and their response to post-weld heat treatment; (2) Quantifying the impact of nanoparticles on the hot crack susceptibility of such aluminum alloys; (3) Investigating the fundamental mechanisms induced by nanoparticles on the changes of solidification behavior and hot crack susceptibility of aluminum alloys.

1.3. Work summary

The remaining part of the dissertation will be organized as follows.

- Chapter 2 reviews hot crack theories and existing work of high relevance to this study.
- Chapter 3 describes the evaluation and fabrication of nanoparticle containing filler metal.
- Chapter 4 presents experimental results on mechanical performance and response to post-weld heat treatment of joints welded with nanoparticle-containing filler metal
- Chapter 5 quantifies the hot crack susceptibility of nanoparticle containing filler metal
- Chapter 6 investigates the changes nanoparticles bring to the solidification process of crack susceptible aluminum alloys
- Chapter 7 draws conclusions
- Chapter 8 recommends future work

2 Literature Review

2.1. Arc welding of aluminum alloys

In arc welding of aluminum and its alloys, the most applied techniques are Gas Metal Arc Welding (GMAW) and Gas Tungsten Arc Welding (GTAW). The use of GMAW is preferred in volume production, where slight sacrifices regarding the quality of the weld can be made to take advantage of the process's high deposition rate and throughput. In contrast, GTAW is commonly chosen in critical high tech applications where control over the weld puddle and superior quality control are required [23]. Figure 2 shows a schematic of the welding torch used in GTAW. The energy necessary to melt and fuse the base metal is generated by an electric discharge between the tungsten electrode and base metal. To understand the polarity option used in aluminum welding, the materials tendency to form an insulating oxide layer on the surface of the melt pool is crucial.

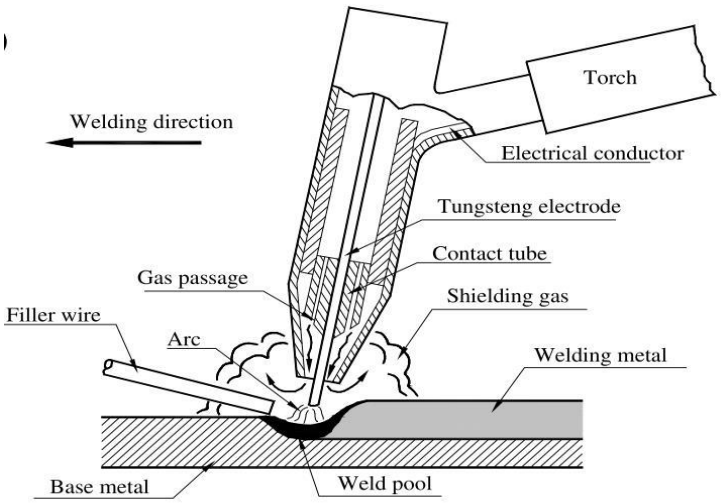

Figure 2: GTAW schematic [23]

While in the welding of steel, a standard-setting of Direct Current Electrode Negative (DCEN) is used to promote the heat input into the base metal by electrons, aluminum is generally welded using Alternating Current (AC) [24]. Here the Electrode Positive (EP) cycle bombards the melt puddle with heavy shielding gas ions and brakes up the oxide layer, and the Electrode Positive Cycle (EN) facilitates the heat input into the base metal. Common shielding gases used for aluminum are argon and helium or a mixture of both. In general applications, the use of argon is preferred for offering a higher cleaning action, greater resistance to cross draft, an easier arc start, and lower cost [25].

The extensive heat input during GTAW influences not only the material properties of the weld metal but also the heat-affected zone (HAZ) of the welded base metal (BM) adjacent to the molten pool, as seen in Figure 3. It is seen that aluminum alloys are generally divided into age-hardened or precipitation-hardened alloys (2000, 6000, and 7000 series alloys) and work-hardened alloys (1000, 3000, 4000, and 5000 series alloys).

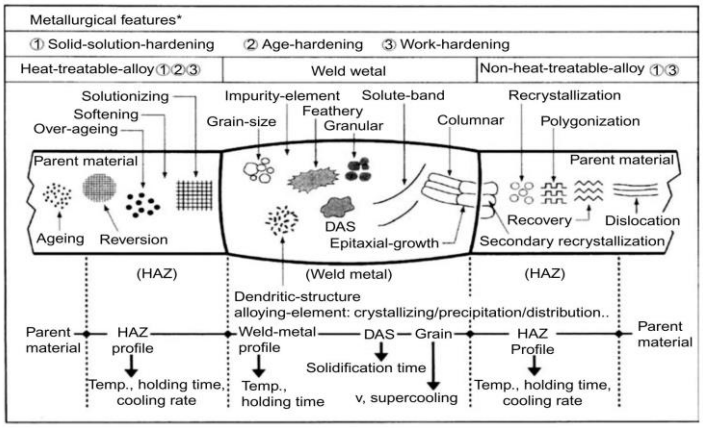

Figure 3: Welding overview [26]

For work-hardened materials, the heat input of the welding process generally causes recrystallization of the grain structure and the loss of strengthening dislocation. The HAZ of strain-hardened materials commonly shows a fully annealed soft zone adjacent to the weld metal, followed by a partially annealed zone where the metal base metal is partially softened.

The strain-hardened microstructure of the material, therefore, deteriorates with decreasing distance from the weld metal. In the case of age-hardened aluminum alloys, the solid-state diffusion facilitated by the excessive heat of the welding process allows the nano-sized secondary phases, the main strengthening mechanism of the material, to grow and become ineffective. Therefore, when determining the resulting strength of a welded joint, these occurrences must be considered. A further crucial point in the welding of aluminum alloys is the choice of filler metal added to the melt pool, as shown in Figure 2.

Unlike in fusion welding of steel, where the filler metal used generally matches the chemical composition of the welded base metal and is only used to fill gaps and build up material [24], the compositions of filler metals used in aluminum welding mostly differ from the chemical composition of the base metal to improve weldability. Due to the high coefficient of thermal expansion, a high degree of solidification shrinkage, and low melting point constituent phases, the chemical composition of many higher strength aluminum alloys is prone to crack during solidification and must be diluted with dissimilar filler metal of low crack susceptibility to yield a defect-free joint. The fundamental reasons for this phenomenon are discussed in detail in the following.

2.2. Hot cracking of Aluminum Welds

A materials susceptibility to hot cracking is influenced by numerous variables and factors that are interconnected and displayed in Figure 4. It is, therefore, difficult to quantify a material's hot crack tendency analytically by its chemical composition alone.

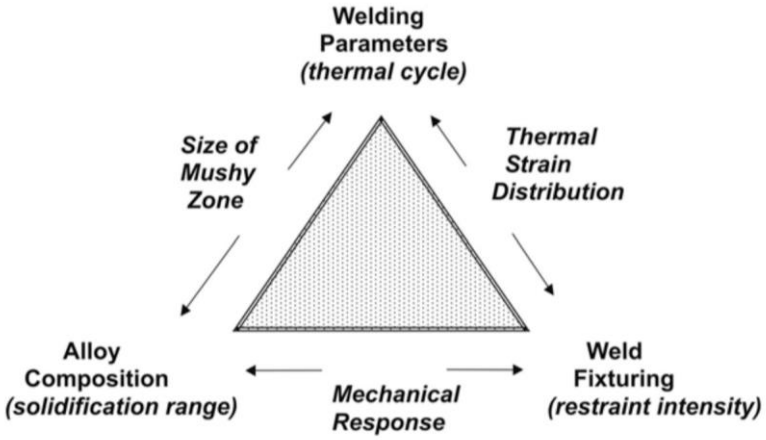

Figure 4: Diagram indicating complex interaction between process parameters affecting weld solidification cracking [27]

Numerous test procedures have been developed to link all existing impact factors and yield valuable insights into their interplay, causing hot cracking. A selection of such procedures will be introduced in the following.

The term hot cracking is generally a category of different types of welding defects that occur before the weld bead has fully solidified. The entirety of this phenomenon is subdivided into solidification and liquation cracking. A schematic of the different conditions occurring during welding is shown in Figure 5.

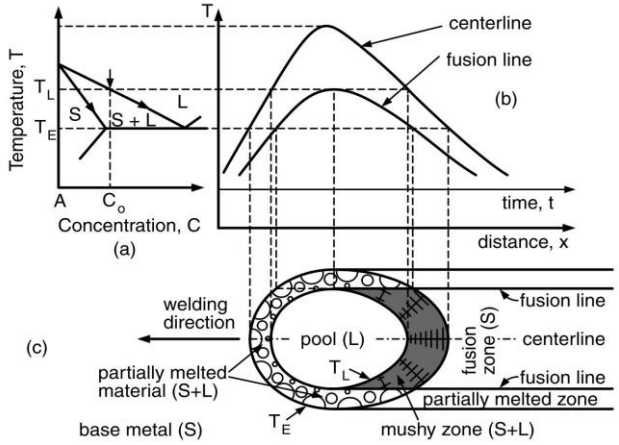

Figure 5: Varying temperatures and compositions along the fusion boundary and partially melted zone [25]

Solidification cracks are linked to solidification events within the mushy zone composed of a mixture of welded base material trailing the melt pool. The dark grey zone indicates this area in the figure. Here the metal solidifies from a fully molten state as epitaxially growing grains at the liquid-solid interface or heterogeneously nucleated grains growing within the weld metal. The tendency for solidification cracking of a welded metal is therefore strongly dependent on the chemical composition of the filler metal used and the dilution ratio of filler metal and weld metal, determining the final chemical composition of the solidifying weld metal. Liquation cracking occurs in the region indicated as “partially melted material” in Figure 5. In this region, the eutectic melting of the base material weakens the linkage between grains, resulting in delamination and cracking. Both concepts are discussed in detail in Chapter 2.2.5.

Even though an extensive amount of research has been conducted to investigate the reasons for solidification cracking, the precise mechanisms responsible for cracking are still not well understood [28]. Models developed to explain the occurrence, and the influence of material properties, as well as the solidification parameters, are generally in agreement that the solidification process can be divided into four distinct stages [29]:

In the first stage, the solidification is governed by mass feeding of liquid towards the growing grains, while the solid fraction is low, and the nucleated grains flow freely.

In the second stage, the growing dendrites form a coherent network forcing the liquid through channels to account for solidification shrinkage within the network. Governed by interdendritic feeding, a pressure gradient can occur, depending on the depth of the formed network. However, the flowability through the network is still considered large enough to avoid the formation of porosity.

The onset of the third stage is initiated by interdendritic separation. Here, liquid pockets are formed, which are either entirely cut off from the melt pool or are unable to back-feed due to

surface tension considerations of the shrinking passages. With the decreased permeability of the network, at this stage, hot cracking and pore formation may occur.

In the last stage, the dendritic network has developed considerable strength, and the fraction of the remaining liquid is low. The liquid pockets are completely isolated, and only high-temperature creep can account for increasing thermal stresses and solidification shrinkage.

Based on this framework, different models have been developed, seeking to quantify the occurrence of hot tearing.

2.2.1. Embrittlement Theory

According to Borland, a materials solidification process is divided into four stages that determine its susceptibility to hot cracking [30]. In Figure 6, the phase diagram of a binary alloy is shown, indicating these stages. The first stage depicts the nucleation and free growth of primary dendrites. Here hot cracks cannot occur by definition. In stage 2, a coherent network of dendrites forms, while the inter-dendritic liquid network is still considered continuous. Hence, the breakage of grains due to stresses caused by solidification can be healed. This liquid network becomes discontinuous in stage 3.

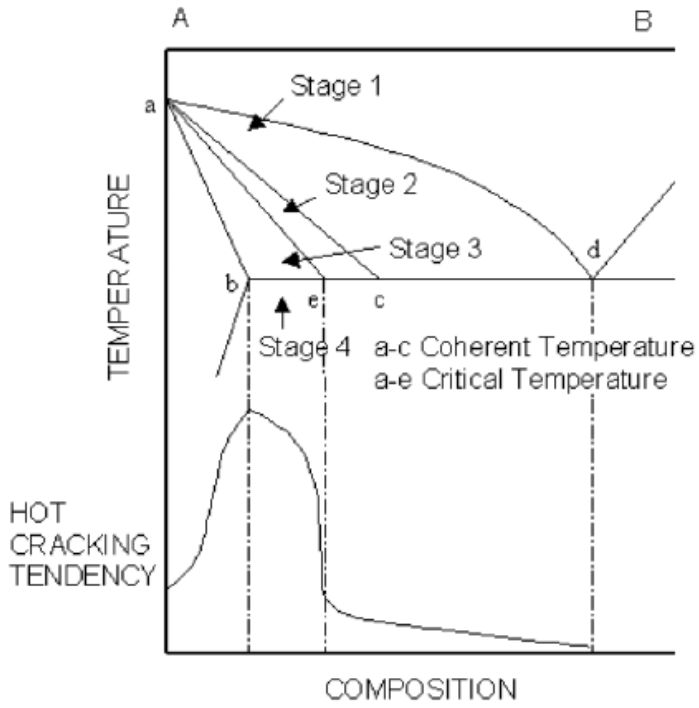

Figure 6 Borland's solidification crack criterion [30]

With the increase in solid fraction, the solid network becomes rigid but brittle. In this stage, the reduced amount of discontinuous interdendritic liquid films cannot sufficiently fill emerging cracks and micro- or macroscopic hot cracks form. Once solidification is completed in stage 4, hot cracks can no longer form due to the lack of liquid phases. Borland defined stage 3 of his model the critical solidification range (CSR). Matsuda refined Borland's model and extended the temperature range of stage 3. It was proposed that cracks are initiated at higher temperatures than projected in the initial model, and that crack propagation is possible at even lower temperatures. This revised model, therefore, extended the CSR [31].

Prokhorov defined a hot crack model by specifying a maximum strain that a material can undergo throughout solidification without cracking [32]. As shown in Figure 7, this model shares similarities with Borland's approach. The upper limit of the defined brittle temperature range (BTR) starts below the liquidus line. With decreasing temperature, the semi-solid network's temperature-dependent critical strain function P(T) decreases, implying

embrittlement of the structure with increasing solid fraction, since the backfilling of inter-dendritic cavities and, therefore, the liquids ability to heal cracks decreases.

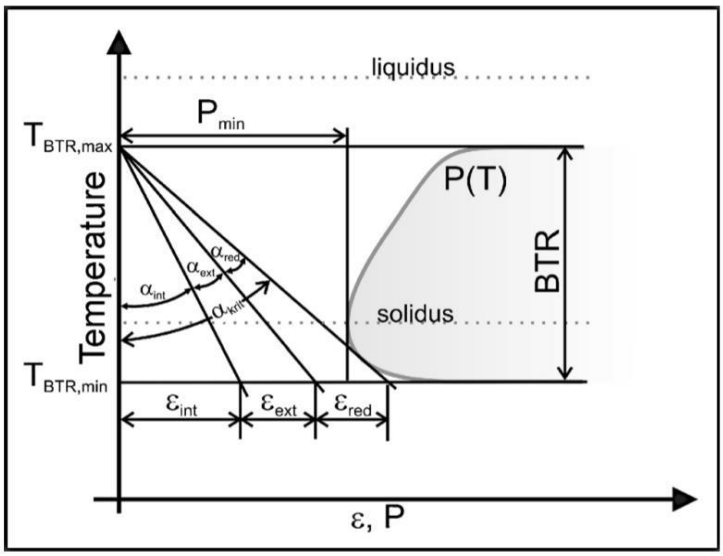

Figure 7: Brittle Temperature Range (BTR) [32]

On the contrary, the acting strain ε, composed of internal strain ε_{int} caused by restrained solidification shrinkage and thermal contraction and external strain ε_{int} caused by mechanical loads or augmented strain increases with decreasing temperature. If during the solidification process, the critical strain is reached, the technological safety $\varepsilon_{red} = 0$, the criterion for hot crack initiation is met. Since the increasing strain ε during solidification follows a linear approximation, Equation (1) can be derived:

$$\frac{d\varepsilon}{dT} = \frac{\frac{d\varepsilon}{dt}}{\frac{dT}{dt}} \tag{1}$$

Where $\frac{d\varepsilon}{dT}$ is the strain increase with decreasing temperature, $\frac{d\varepsilon}{dt}$ is the strain rate and $\frac{dT}{dt}$ cooling rate. An advantage of this model is that hot crack tests using externally augmented strain can be quantified.

2.2.2. Rate of Feeding (ROF) Rate of Shrinkage (ROS) model

The Rate of Feeding – Rate of Shrinkage model, was initially developed to describe solidification cracking in cast aluminum alloys by Feurer [33]. It was later adopted to model solidification cracking in arc welding based on a dynamic equilibrium condition governed by thermal and solidification shrinkage of intergranular channels, which must be backfilled with liquid from the melt pool. As illustrated in Figure 8, the model assumes a dendritic network of liquid channels with restricted permeability.

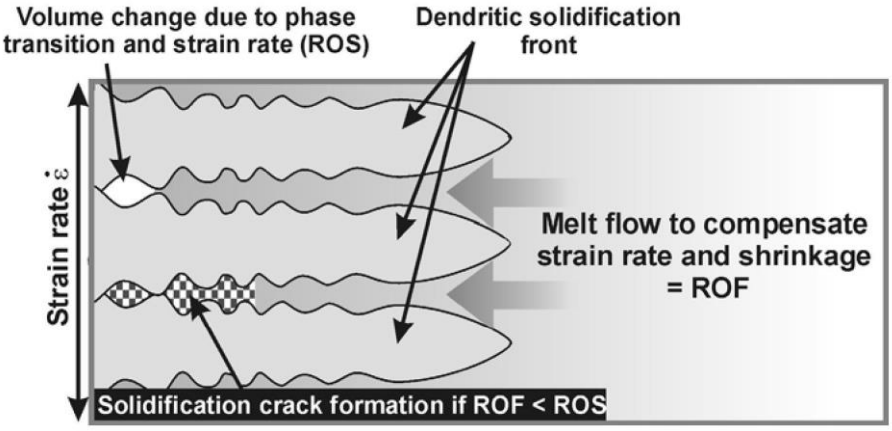

Figure 8: Rate of Feeding (ROF) – Rate of Shrinkage (ROS) model [27]

The condition for hot cracking is given once the permeability of the liquid network is no longer able to compensate for thermal and solidification shrinkage, and therefore, the possible Rate of Feeding drops below the Rate of Shrinkage. Feurer described the Rate of Feeding as given in equation (2) based on Darcy law by modeling the intergranular network as a porous media.

$$ROF = \left(\frac{\delta lnV}{\delta t}\right)_{feeding} = \frac{{f_l}^2 {\lambda_2}^2 P_S}{24\pi c^3 \mu L^2} \tag{2}$$

Here the effective feeding pressure $P_S = P_0 + P_M - P_C$, is derived from the atmospheric pressure P_0, the metallostatic pressure P_M and the capillary pressure P_C. f_l is the volume of the liquid network, c is the tortuosity constant of the liquid network, L is the size of the semi-solid

zone, λ_2 is the secondary dendrite arm spacing, and μ is the viscosity of the liquid phase. The counteracting Rate of Shrinkage was defined as:

$$ROS = \left(\frac{\delta lnV}{\delta t}\right)_{Shrinkage} = \frac{(\rho_0 - \rho_S + \alpha k C_L) T {f_L}^{2-k}}{\rho(1-k) m_L C_0} \quad (3)$$

Where, ρ_0 and ρ_S are the densities of the liquid phase at the melting point, C_0 is the alloy composition, C_L is the composition of the liquid at the solid-liquid interface, k is the equilibrium partitioning coefficient, m_L is the slope of the liquidus line, α is the composition coefficient of liquid density. Clyne and Davis further combined Borland's theory with the RoF-RoS model and postulated a critical time period where RoF<RoS, where developing strain cannot be compensated [34]. The model defines a vulnerable time period t_V where the impinged grains are easily separated between 90 and 99 % of solid fraction and a time t_r where stress and strain can easily be compensated between 40 – 90 % of solid fraction. The ratio t_V/t_r gives the crack susceptibility coefficient (CSC).

2.2.3. Rappaz - Drezet – Gremaud (RDG) model

The RDG hot crack criterion was introduced by Rappaz et al. in 1999. The fundamental cause of hot cracking in this model is given if the pressure of the solidifying liquid in between dendrites falls below its cavitation pressure. Cavities initiating hot cracks are formed [35].

The model is based on the following assumptions. During solidification, the dendritic structure is subjected to thermal stresses that change the volume of the interdendritic liquid. Further, the ongoing liquid-solid phase transition decreases the volume of the liquid fraction. Since the model assumes a state of dendrite coherency, the backfilling of this volume relies on the permeability of the skeleton network. If interdendritic feeding becomes insufficient, cavitation pores are formed, which act as nuclei for hot cracks. The model is formulated based on the pressure equilibrium shown in the following equation;

$$\Delta p_{max} = \Delta p_{\varepsilon} - \Delta p_{sh} = p_m - p_c \tag{4}$$

Here the metallostatic pressure p_m represents the pressure within the melt bath without external influences. With increasing difficulty to back-fill cavities the thermal strain (Δp_{ε}) and solidification shrinkage (Δp_{sh}) decrease the absolute pressure, therefore the difference between p_m and the cavitation pressure (p_c) results in the maximum allowable pressure drop(Δp_{max}).

This pressure drop is modeled in detail in the following equation

$$\frac{180}{\lambda^2}\frac{(1+\beta)\mu}{G}\int_{T_S}^{T_L}\frac{E(T)f_S(T)^2}{(1-f_S(T))^3}dT + \frac{180}{\lambda^2}\frac{v_T\beta\mu}{G}\int_{T_S}^{T_L}\frac{f_S(T)^2}{(1-f_S(T))^2}dT \tag{5}$$

Where $E(T) = \frac{1}{G}\int f_S(T)\dot{\varepsilon}_P(T)dT$, μ is the liquid viscosity, β is the shrinkage, λ is the secondary dendrite arm spacing, v_T is the velocity of the isotherms, G is the thermal gradient, $f_S(T)$ is the temperature-dependent fraction of solid, T_S is the solidus temperature and T_L is the liquidus temperature. The results of an experimental investigation on the crack susceptibility of a binary Al-Cu alloy with varying copper content were found to be in good agreement with the predictions of the RDG model. However, the model has been criticized for its lack of universal applicability [36]. Hot cracking is mostly initiated on intergranular grain boundaries, and not as modeled in the inter-dendritic boundaries of columnar dendrites. At these intergranular grain-boundaries, growing dendrites are not aligned but impinge on each other at varying angles, and significantly different temperature and concentration conditions are given under these circumstances. To highlight this misconception, the authors found that hot cracking predominantly occurs if a critical grain boundary angle is exceeded. Moreover, essential variables of the model, such as v_T, λ or G are dependent on the welding conditions, and therefore are not intrinsic material constants, and most importantly vary along the solidification front, as shown in Figure 5. Since the RoF-RoS model is making use of similar parameters and

assumptions, both models are only applicable under very restrictive boundary conditions and show limited applicability to universally model the occurrence of hot cracking.

2.2.4. Liquation cracking

Aluminum alloys typically show a tendency to liquation cracking if subjected to fusion welding. These types of cracks are typically found outside the WM in the PMZ shown in Figure 9a. In this region, the material is not fully melted but is exposed to a temperature above the BM's eutectic temperature, causing eutectic liquation. Since the presence of a PMZ does not necessarily result in cracks, Huang et al. formulated the following conditions for the occurrence of liquation cracking [37]:

1. The material must exhibit a significant tendency to contract during solidification and cooling
2. The welding setup must be significantly restraint to keep it from moving freely
3. The welded BM must be sufficiently alloyed to exhibit significant liquation and weakening in the PMZ
4. No solidification cracking in the WM should be present to relief tensile strain from the PMZ

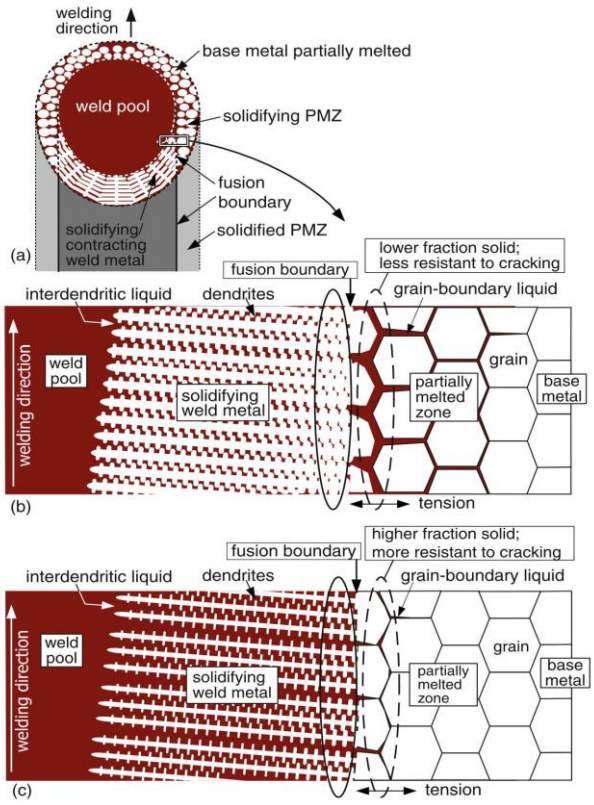

Figure 9: Liquation cracking during fusion welding [38]

Once these conditions are met, a force balance can be formulated depending on the solid fraction of WM and PMZ. If during solidification, the temperature depended solid fraction ($f_s(T)$) of the WM, is larger than the solid fraction of the PMZ, and therefore solidifies later than the BM, the condition for liquation cracking $WM\ f_s(T) > PMZ\ f_s(T)$ is met. As shown in Figure 9b, the contraction forces of the earlier solidifying WM lead to a liquid rupture in the PMZ. Figure 9b shows a schematic example for $WM\ f_s(T) \leq PMZ\ f_s(T)$. Here, the formation of solid within the WM is slower than the solidification of liquated eutectic films within the PMZ. The recovering strength of the PMZ, therefore, exceeds the increasing tensile strength exerted by the WM, and liquation cracking is prevented. The fraction of solid in both regions is almost exclusively governed by the chemical composition of BM and used filler metal. Hence, welding with dissimilar filler materials, too, e.g., prevent solidification cracking, may very well lead to liquation cracking [39].

2.2.5. Factors influencing solidification susceptibility

In practice, the susceptibility to hot cracking in aluminum weld generally depends on the aluminum alloys' intrinsic material properties and external parameters dictated by the welding process. The most critical factors within these categories are introduced in the following.

2.2.5.1. Material properties

Surface Tension

Borland further investigated the influence of liquid distribution within the semisolid network on hot crack susceptibility [30]. He quantified the dependence of solute distribution with the following expression:

$$\tau = \frac{\gamma_{SL}}{\gamma_{SS}} = \frac{1}{2\cos(\frac{\theta}{2})} \tag{6}$$

Where τ is the liquid wettability, γ_{SL} the solid-liquid surface tension, γ_{SS} the solid-solid surface tension, and θ the dihedral wetting angle. Figure 10 shows the relation between the dihedral wetting angle and the solute distribution on the grain surface.

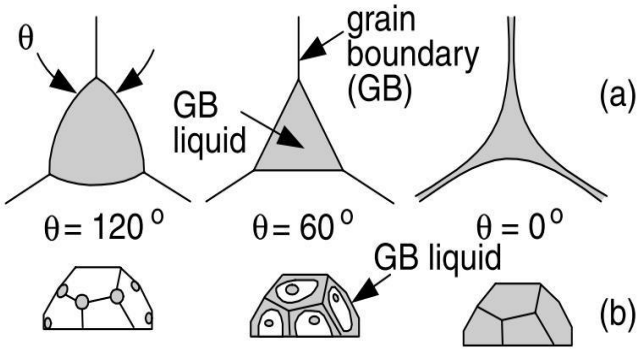

Figure 10: Grain boundary liquid: (a) dihedral angle; (b) distribution of liquid at grain boundary [25]

The two extreme dihedral wetting angle values of 180˚ and 0˚ provide the greatest resistance to cracking. For a maximum angle, for low γ_{SL}, a continuous network providing backfilling is

likely, while a minimum angle implies, for high γ_{SL}, strong bonding between the grains is promoted, and therefore, cracking is mitigated [27]. Seveiko further concluded that the surface tension of the solidifying material has an impact on the rupture resilience of the liquid film itself. The following expression correlates the force necessary to separate two parallel faces wetted by a liquid film:

$$F = c_l \frac{\gamma A}{t} \tag{7}$$

Where F represents the force, A the wetted surface area, γ is the vapor-liquid surface tension, and t the distance between the faces. Therefore, high surface tension, in combination with a thin liquid film, should have the highest crack resistance [40].

Eutectic composition

The fraction of interdendritic liquid present at the eutectic temperature, and therefore, the terminal stage of solidification increases with the addition of constituent elements[25]. This correlation can be described with the Scheil Equation for non-equilibrium solidification:

$$f_E = (\frac{C_O}{C_E})^{\frac{1}{(1-k)}} \tag{8}$$

Where f_E is the fraction of eutectic, C_O is the solute content, k is the partition coefficient and C_E is the eutectic composition. As shown in Figure 11, it has been proven that with an increasing amount of eutectic liquid at the terminal stages of solidification, the crack susceptibility of solidifying aluminum alloys decreases.

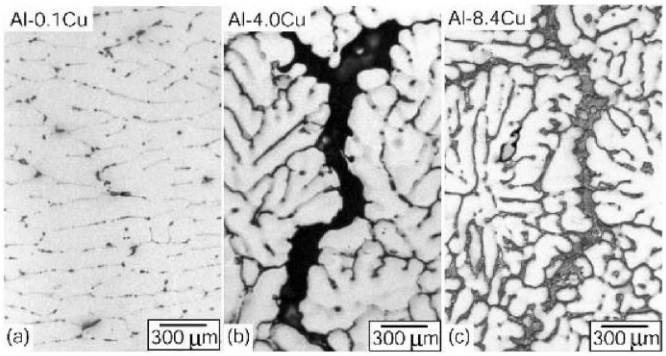

Figure 11: Aluminum welds with three different wt% of copper [25]

The study hypothesized that an increasing amount of eutectic promotes a less coherent dendritic structure, which offers a higher permeability to backfill and heal cracks as displayed for the solidified Al-8.4Cu alloy. Therefore, typical filler metals that significantly lower the hot crack susceptibility during welding such as ER2319 (Al-6.3Cu) and ER4043 (Al-5.3Si), generate large amounts of eutectic liquid during the solidification of the weld metal [41][24]. However, it is noted that filler metals such as ER5356 (Al-5Mg) that exhibit a very low eutectic fraction also improve the weldability of aluminum alloys. It is theorized that the large solidification range, in combination with a low amount of eutectic generated, a high level of coherency, can resist stresses during solidification [27].

Grain Size

In aluminum alloys, a large number of studies found a strong correlation between the susceptibility of a material to hot cracking and its grain size. It was shown that by employing grain refiners, the weldability of aluminum alloys was significantly improved over unrefined reference welds. A common explanation can be found in the strain distribution caused by solidification and thermal shrinkage. A smaller grain size and, therefore, an increased number of grain boundaries facilitate a more even distribution of stress and strain throughout the semi-

solid network. Hence, the maximum occurring stress per grain boundary is reduced, and the system is less likely to show cracking.

Janaki Ram et al. conducted GTAW experiments with AA7020 (Al–4.5%Zn–1.2% Mg–0.15% Zr) using an Al-2.8% Zn-4% Mg filler metal with various grain refiner additions ([42]. Using a Varestraint test, it was shown that with the addition of 0.5w% Ti and 0.1w% B to the filler metal, the total resultant crack length was reduced from 11 mm to 4.5 mm, compared to the weld performed with the pure Al-2.8% Zn-4% Mg filler metal.

In the Selective Laser Melting of AA7075, Martin et al. decorated the feedstock powder with zirconium hydride particles to improve the printability of the material [7]. The resulting parts in T6 heat treatment condition showed an Ultimate Tensile Strength of 383 – 417 MPa, which is well below 570 MPa, the value for wrought AA7075-T6 [43]. Since no HIP treatment was performed before testing, which is known to heal microcracking within additively manufactured parts [44], it is unknown whether this loss in strength is attributed to micro cracking, loss of strengthening elements during processing, or other material imperfections.

The influence of various amounts of grain refiner addition on the Hot Tear Susceptibility (HTS) of AA7136 is shown in Figure 14. While with increasing amounts of titanium up to 0.1w%, the crack tendency is decreased; this trend was found to be reversed upon further titanium addition [45].

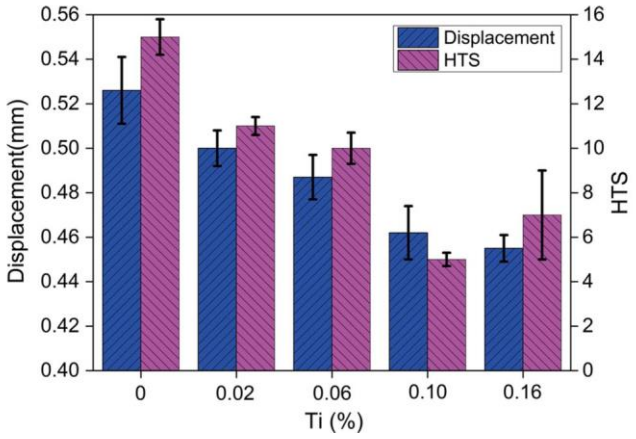

Figure 12: Effect of grain refinement on hot crack susceptibility [45]

These findings are in agreement with Warrington's study, which found a turning point in crack susceptibility for AA7050 and AA7010 with increasing levels of titanium [46]. The authors concluded that while grain refinement is theoretically beneficial to suppress hot cracking, the presence of a eutectic liquid network cannot be neglected, as discussed before. Easton et al. found this occurrence in agreement with the RDG model [47]. Thermal analysis of solidifying Al-Si-Cu and Al-Cu alloys further investigated the decrease in non-equilibrium eutectic phases with increasing grain refinement. Figure 13 shows the eutectic portion of cooling curves of an AlSi7Cu3Mg alloy refined with 100 ppm Sr, 100 ppm Sr + 0.125 wt.% Ti and 100 ppm Sr + 0.175 wt.% Ti.

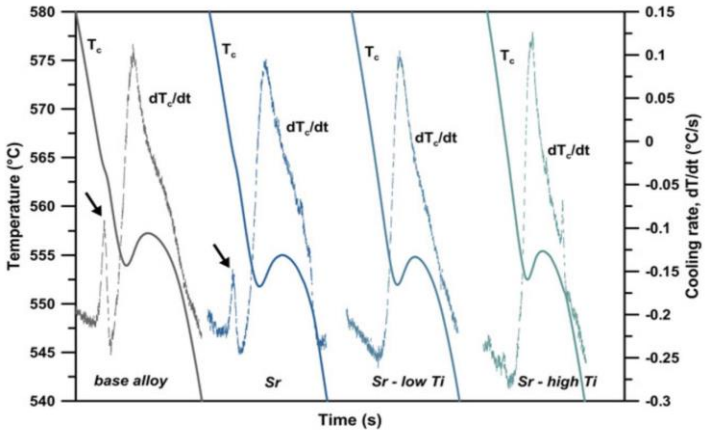

Figure 13: Eutectic peaks with an increasing amount of TiB grain refiner [48]

It is shown that the fraction of eutectic solidifying is reduced with increasing grain refinement [48]. The decrease in grain size leads to an increased grain surface area and decreased diffusion path the grain center due to grain refinement. Therefore, a larger fraction of constituents diffuse into the growing aluminum grains, leaving less non-equilibrium eutectic as intergranular liquid. A similar trend was found in Al-3.7Cu and Al-4.8Cu alloys refined with 0.1% of Al-5Ti-1B alloy [49].

As an alternative to the conventional Al-TiB grain refiner, the addition of scandium showed promise in reducing aluminum alloys' susceptibility to hot cracking. Here the primary Al_3Sc acts as a heterogeneous nucleation site for the aluminum alpha grain [50]. To facilitate this effect, the addition of more than 0.5w% Sc is necessary to form a hypoeutectic composition [51]. However, Mousavi et al. showed a sufficient impact of scandium on the crack susceptibility of AA7010 at additions below 0.2w% [52] while Reddy et al. showed similar results for the same alloy upon 0.25w% scandium addition [53].

The crack suppressing effect of scandium addition to aluminum alloys was further utilized by Qbau et al. in Selective Laser Melting of AA6061 [54]. By the addition of 0.15w% Sc to AA6061, a relative density of 99.98 % was achieved. Tensile testing of the modified alloy system showed a remarkable improvement over its commercial counterpart. While the fabricated A6061 reference fractured at 50 MPa, below 1% strain, the AA6061-0.15Sc sample exhibited a yield strength of 300 MPa, an Ultimate Tensile Strength of 350 MPa, and elongation at break of 31 % in as printed condition.

However, despite the promising effects on hot cracking, the lack of reliable and predictable production in combination with the high price of scandium has so far limited the widespread industrial application of scandium in aluminum alloys [55].

Porosity

Porosity in aluminum welding is generally caused by the dissolution of organic residues or moisture in the shielding gas combined with aluminum's high affinity to dissolve hydrogen in the liquid state. Upon solidification, the solubility of hydrogen drops by an approximate factor 20, causing excessive hydrogen to precipitate in the form of gas pores.

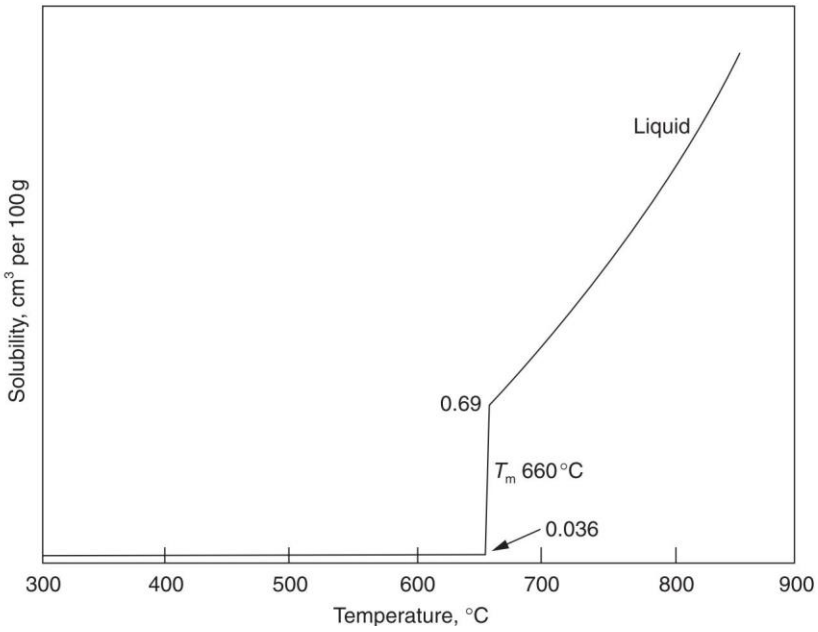

Figure 14: Solubility of hydrogen in aluminum [24]

As previously discussed, the RGB model explains the occurrence of hot cracking during solidification with the formation of cavitation, which is theoretically further facilitated by the precipitation of porosities. Coniglio et al.'s study into this matter concluded that with the additions of small amounts of hydrogen, the weldability of aluminum alloys was reduced, whereas the additions of larger quantities ultimately enhanced the resistance to solidification cracking. The authors found a critical range of approximately 0.47 – 1.28 ml/100g of hydrogen dissolved in the weld metal, where the precipitation of micropores caused continuous solidification cracking[56].

Alloy composition

As previously discussed in the paragraph on the effects of "Eutectic composition" on the weldability of aluminum alloys, an alloy's intrinsic susceptibility to hot cracking is dictated by the selection and amount of constituent elements. Figure 15 gives a general impression of binary aluminum systems and their crack sensitivity dependent on the amounts of constituent elements added.

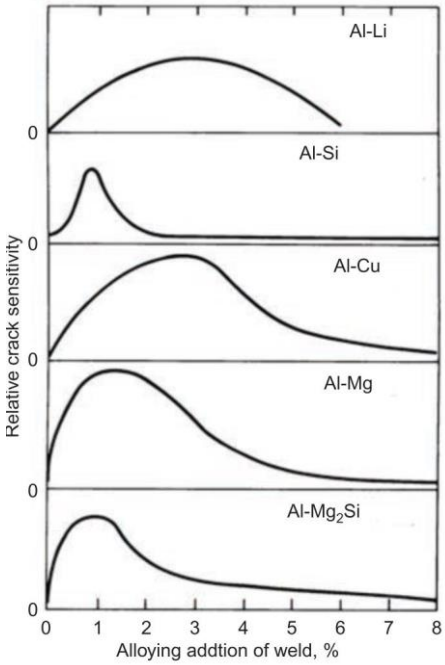

Figure 15: Effect of alloy content on crack sensitivity of select binary aluminum alloys [57]

It is understood that all shown constituent elements cause a peak susceptibility between 1-3 wt%, which further supports the practice of using highly alloyed filler metal to mitigate the hot crack susceptibility of aluminum alloys during solidification. Therefore, binary aluminum-copper alloys are generally considered weldable with the use of filler metal containing 6 wt% copper or more [24]. A more detailed display of the impact constituent elements have in ternary Al-Cu-Mg, Al-Mg-Si, and Al-Zn-Mg systems are shown in Figure 16. The graphs show crack length invariant maps, where a higher number suggests a higher susceptibility to hot cracking of the respective alloy composition. The high crack susceptibility of 6000 series alloys at peak

strength composition becomes apparent, which is comparable to Al-Zn-Mg alloys [26]. However, the shown hot crack mappings easily illustrate the beneficial effects of dissimilar filler metal on the susceptibility to solidification cracking in aluminum welds. Similarly to the previous binary aluminum-copper example, beneficial effects regarding the weldability of AA2014 (Al-4.5Cu-0.5Mg) with the use of ER2319 (Al-6.3Cu) filler metal have been reported [58].

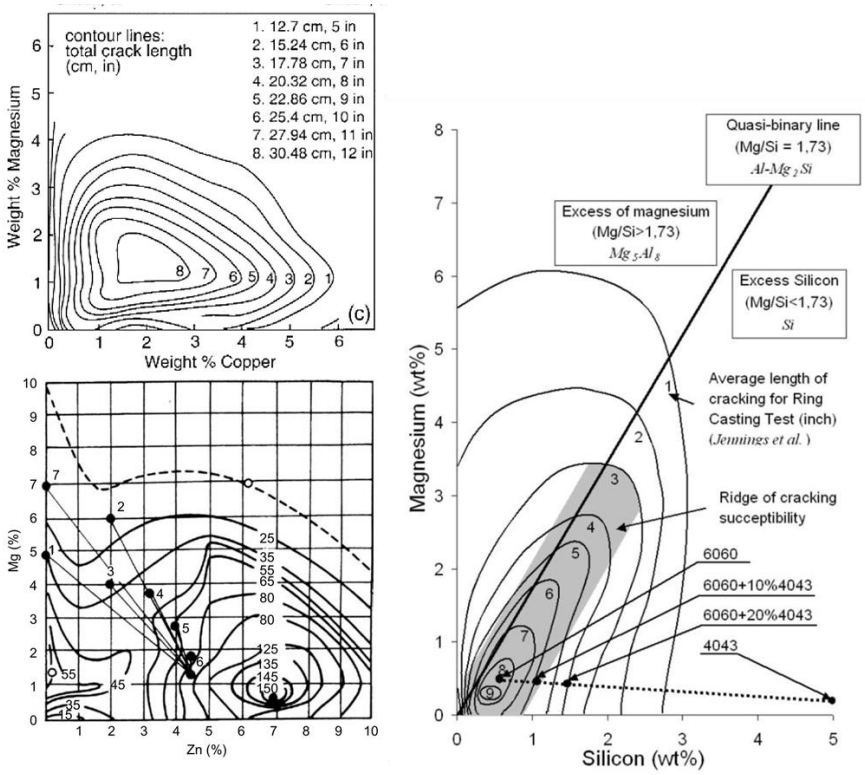

Figure 16 Hot crack susceptibility of the Al-Cu-Mg system [25], Al-Mg-Si system [59], and Al-Zn-Mg system[26]

It is seen that the crack susceptibility correlated with 4.5Cu-0.5Mg decreases with an increasing amount of copper, and a decreasing amount of magnesium, shifts to a lower crack invariant. In the case of 6000 series aluminum, the Al-Mg-Si map demonstrates the reasoning behind the significant weldability improvement when welded with ER4043 (Al-5.3Si).

The chemical composition of the welded AA6060 is easily shifted to significantly to a lower crack invariant by the addition of ER4043 [59]. Examples for the weldability improvements

using dissimilar filler metal can further be found in the Al-Zn-Mg system. The binary AA7005 (Al-4.5Zn-1.6Mg) is in practice generally welded with high magnesium filler metals, such as ER5183 (Al-4.8Mg) [60]. However, it must be noted that with the addition of copper, the Al-Zn-Mg system, as found in AA7075, the solidification range of the resulting alloys significantly increases, making this approach obsolete. Furthermore, as aforementioned, the use of dissimilar filler metals brings drawbacks concerning the weld metals mechanical, corrosion, and thermal properties, while possibly generating liquation cracking during welding.

2.2.5.2. Process parameters

The second category of significant influences on the crack susceptibility are parameters and conditions introduced by the welding process itself. The grain structure of the weld metal generated during arc welding highly depends on the temperature gradient G and the growth rate R, as shown in Figure 17. The temperature gradient G across the liquid-solid interface is strongly connected to the heat input of the welding process and eventual pre-heating of the weld metal, while the growth rate R is determined by the speed at which the solidification front progresses and, therefore, the forward speed during welding.

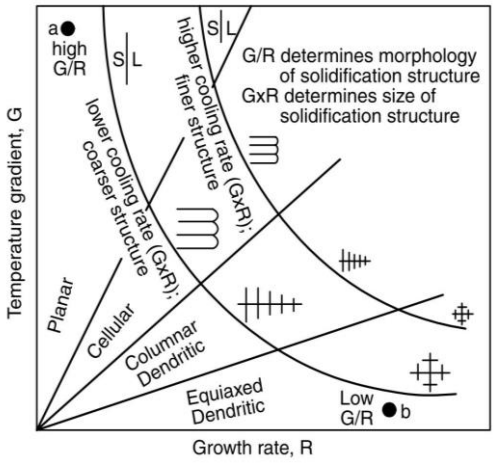

Figure 17: G/R schematic [25]

As described earlier, to reduce the weld metal's susceptibility to hot cracking, a fine equiaxed grain structure is highly desired over a columnar dendritic growth, defined as crack susceptible morphologies in the RDB and Rof-RoS model. In the following, methods are introduced which modify the solidification conditions during welding.

Oscillation of Arc

Kou et al. showed the effects of transversal arc oscillation on the crack growth of AA 5052. This technique leads to alternating columnar grains, which inhibit crack growth and grain refinement in the MZ. Using this technique, the crack, if occurred, cannot easily trail the MZ, but is stopped by the continually changing direction of the columnar grain growth. In this approach, grains are refined due to the increase of the absolute velocity of the MZ and therefore increase of cooling rate, while the welding speed remains the same [61].

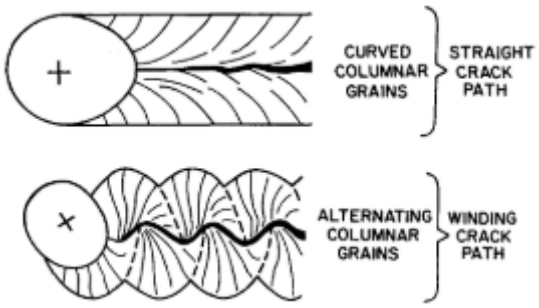

Figure 18: Schematic of the effects of oscillating arc [61]

Biradar et al. used this approach to weld AA2014 joints with remarkable improvement of the liquidation and solidification cracking. At an optimum oscillation amplitude of 0.9 mm and an optimum oscillation frequency of 0.49 Hz, the total crack length improved, as shown in Figure 19.

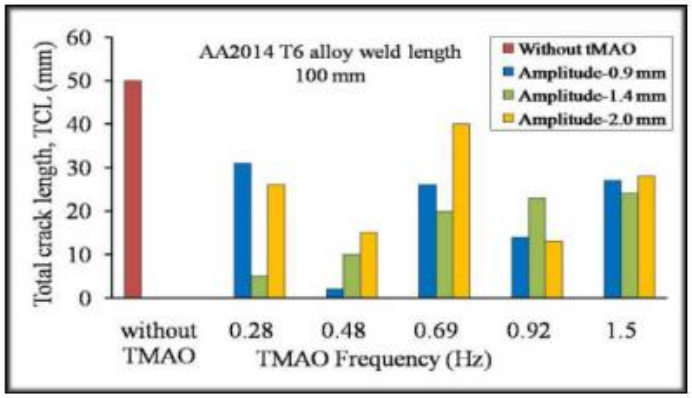

Figure 19: Effects of different oscillation frequencies and amplitudes on crack length [62]

The grain size, compared to welding without oscillation, was reduced from 21.9 µm to 12 µm, while yield strength, tensile strength, and ductility improved by 16.6%, 5.6%, and 34%, respectively [62].

Arc Pulsing

Using a pulsed current of the GTAW arc in combination with ER5356 filler metal, it was shown that AA7075 sheets were weldable in butt weld configuration. While the weld efficiency was low, yielding a UTS of 295, the welds were considered sound. However, the susceptibility to hot cracking was not quantified [63,64].

Pereita et al. quantified the effect of arc pulsing on the hot crack susceptibility of AA6351 [65]. In this study, a Houldcroft test was performed without filler metal. It was shown that the common trend of increasing crack length with increasing weld forward velocity was significantly impacted by the introduction of arc pulsing. It was concluded that pulse frequency and welding speed are competing parameters in the development of solidification cracks.

Thermal manipulation

As a further adjustment to the welding process, it was found that introducing a heat sink that trails the weld bead reduced the crack susceptibility in AA2024 [66]. The authors implemented a nozzle spraying liquid nitrogen onto the solidified weld metal. The enhanced thermal gradient refined the grain structure and reduced the BTR. In contrast, Doumanidis et al. implemented a secondary welding torch to manipulate the weld bead geometry and yield an improved weld metal microstructure with lowered residual stress and distortion [67].

2.2.6. Methods for hot crack evaluation

To date, a variety of test procedures to evaluate a material's susceptibility to hot cracking are available. A review found that Varestraint, Gleeble, Houldcroft, and Circular patch tests (in declining order of research published) were the most widely used tests in research applications between 1938 and 1989 and have established a wide acceptance [68].

2.2.6.1. Circular groove test

The circular grove test is a self-restrained hot crack test, where a groove is machined into square sheet metal, as shown in Figure 20 left. The crack susceptibility of Filler metal/base metal combinations can further be evaluated by performing a continuous circular weld following the machined notch. It is noted that the level of restraint and, therefore, the intensity of solidification cracking is variable with sheet thickness and groove depth. An additional level of restraint can be realized by mounting the sample in a jig, shown in Figure 20 right. Due to the circular shape of the weld bead, the stress caused by thermal expansion and solidification shrinkage increases with the progression of the weld bead.

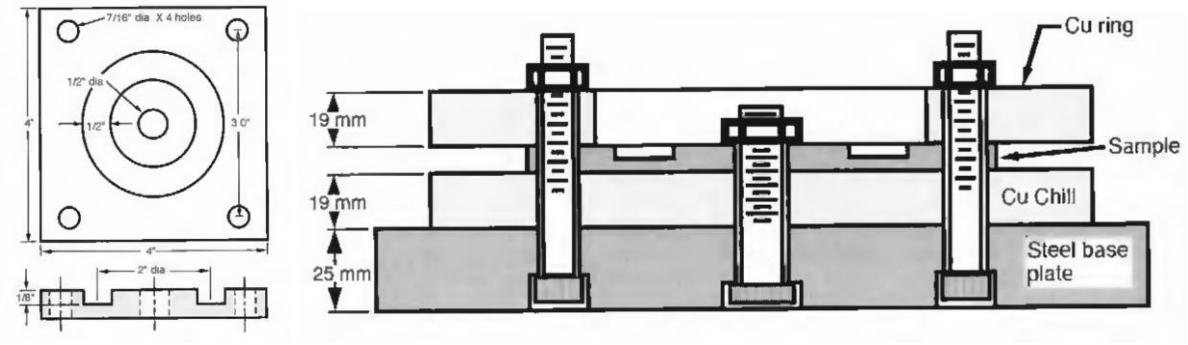

Figure 20: Circular groove test [69]

While some consider the circular groove test a simple go-no-go hot crack test [70], other results showed success in quantifying the distance of crack-free solidification from the start point to the onset of solidification cracking in degrees (0-360˚) observed in different systems investigated [69]. This testing method is considered simple to conduct and proved insensitive to welding parameters applied [68]. However, the material and machining cost necessary for a detailed study cannot be neglected.

2.2.6.2. Houldcroft test

Developed by Houldcroft in 1955 [71], the Houldcroft test was designed to evaluate the hot crack susceptibility of thin metal sheets during arc welding, with a test specimen shown in Figure 21. During the test, the restraint of the sheet caused on the weld bead decreases with increasing relief slot depth. The sheet metal's susceptibility to hot cracking is subsequently quantified by dividing the resultant crack length by the length of the specimen. It is further possible to evaluate filler metal/base metal interactions on hot crack susceptibility by feeding filler metal into the melt pool with a "bead-on-plate" approach, ensuring a full penetration weld [72].

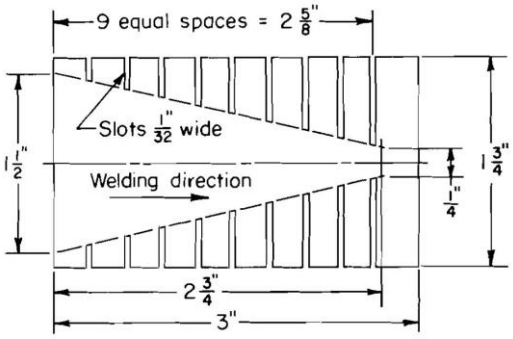

Figure 21 Houldcroft test specimen [70]

For this test, it was found that the crack length is inversely proportional to the heat input divided by the specimen thickness, expressed by the following equation:

$$\frac{1}{C_l} \propto \frac{Q}{t} = \frac{\frac{I * E}{v}}{t} \tag{9}$$

Where, C_l is the crack length, Q is the heat input, t is the sample thickness, I is the welding current, E is the welding voltage, and v is the welding forward speed. Therefore, by employing this test, the influence of processing parameters on the crack susceptibility can be quantified [73]. The Houldcroft test is considered easy to conduct, and the material cost is lower than for the circular groove test, while due to the complex geometry of the specimen, machining costs may be increased [68].

2.2.6.3. Varestraint test

The Varestraint test was developed by Lundin and Savage in 1965 [74], and a schematic is shown in Figure 22. Its name is an abbreviation of the term *vari*able *restraint*. The setup consists of a die, a mechanism to forcefully bend the welded sheet over the die, and a welding tractor. During testing at a defined moment, the mechanism bends the welded sheet downwards at a relative deformation speed much higher than the welding forward speed. The schematic illustrates the Varestraint test (left), where bending strain is augmented perpendicular to the

welding direction, and the Transvarestraint test (right), where the strain is augmented parallel to the welding direction. With this testing method, theoretical hot crack criteria such as Prokhorov's embrittlement theory involving external strain can be experimentally investigated [75]. Here the MCL (Maximum crack length) observed during the Varestraint test is strongly correlated with a material's brittle temperature range, while the TCL (Total crack length) is used as a metric to quantify a materials crack susceptibility.

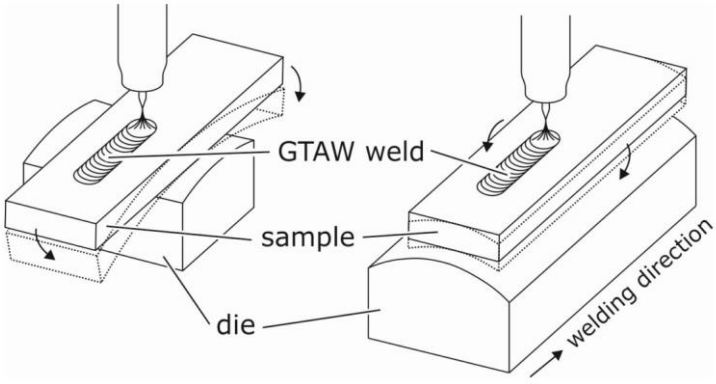

Figure 22: Varestraint test [76]

When testing the crack susceptibility of a filler metal/base metal combination, a U-shaped notch is machined into the sheet [76]. Utilizing this test setup, it is possible to obtain a material's crack susceptibility in relation to the externally augmented strain and generate so-called "Ductility curves"[77].

2.2.6.4. Gleeble test

The proprietary Gleeble welding simulator apparatus is shown in Figure 23. In this test setup, a rod-shaped specimen is clamped between water-cooled jaws and heated by electrical resistance.

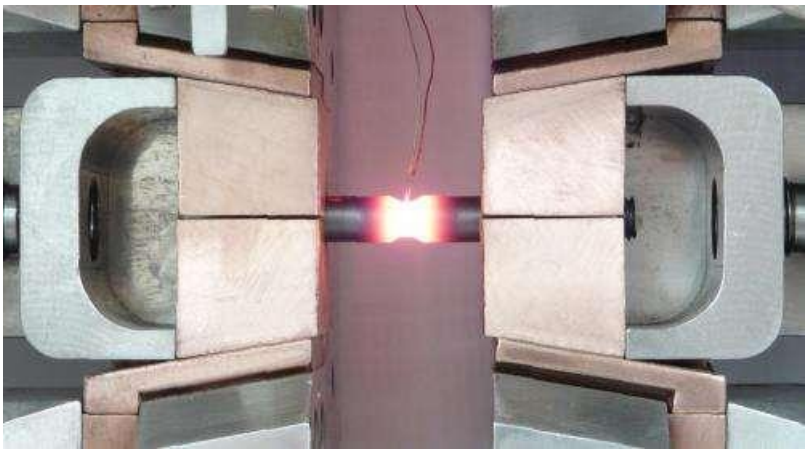

Figure 23: Gleeble welding simulator [78]

The mechanism is housed in a chamber filled with protective gas. Input parameters such as the number of welding passes, welding current, welding voltage, welding speed, and heat input [79] are translated to heating and cooling curves, as well as different types of thermal gradients throughout the sample by adjusting current and water cooling of the jaws. At any given of the testing cycle, a tensile or compressive force can be augmented onto the specimen. The thermal gradients during the test can be recorded with several thermocouples attached to the specimen. The system is, therefore, able to determine a materials Brittle Temperature Range, quantify a material's susceptibility to hot cracking, and determine critical augmented amounts of strain and strain rates at which hot cracking occurs. [27].

2.3. Metal matrix nanocomposites

In the past decades, the research into metal matrix nanocomposites, especially aluminum-based nanocomposites, has experienced significant growth. While, in theory, aluminum matrix nanocomposites (AMNCs) exhibit the potential to enhance the material's mechanical properties and thermal stability, the route to manufacture said materials, especially in a large-scale fashion, remains challenging. Non-homogeneous particle dispersion and the interface bonding between reinforcement and matrix remain issues that require scientific and engineering solutions. Here

the processing route plays a crucial role, which typically starts with the distinction between in-situ and ex-situ incorporated reinforcements. For the ex-situ method, already fabricated nanoparticles are incorporated into a metal matrix. This commonly happens via powder metallurgy, such as ball milling, where large force drives the particles into the metal particles, or simply the decoration of metal powders with nanoparticles. In a following step, these preliminary composites are compacted and consolidated, using sintering, melting, hot extrusion, or laser processing to create stronger bonding between particle and matrix and form a bulk material.

Another ex-situ approach to “assemble” particles and the metal matrix is by using microfabrication processes such as CVD, PVD, or electrical deposition. While these methods generate MMNCs of outstanding quality regarding the dispersion and distribution of particles, their scalability remains limited. To achieve a better yield of material quantity, the route of liquid metallurgy is employed. Here, nanoparticles are introduced to the metal matrix in the liquid state. The major challenge with this approach is clustering and poor dispersion of the reinforcements due to Van der Walls attraction [80]. To overcome this issue, e.g., high processing temperatures or ultrasonic mixing are applied to introduce energy to counteract the attractive force. With the help of ultra-sonic cavitation to break up the formation of particle clusters, MMNCs containing, for example, SiC, Al2O3, TiB_2, TiC have been successfully fabricated [81–85]. To further enhance the incorporation success rate by limiting burning and clustering during the feeding process, flux assisted incorporation was developed. Here, nanoparticles are mixed with a suitable salt mixture and then fed to a molten metal pool. The molten salt protects the nanoparticles from burning, dissolves the hindering oxide layer on the metal surface, and pushes the nanoparticles into the metal due to a favorable salt-TiC / metal-TiC wetting angle ratio (Liu et al. 2016). However, perfect dispersion is difficult to achieve with this method, as during solidification, some particles are pushed to the grain boundary.

In-situ fabrication is the second route to create MMNC. Here, the nanoparticles are generated inside the metal matrix during the fabrication process via, e.g., reactive hot pressing, combustion synthesis, and direct metal oxidation [86]. These methods strongly rely on processing parameters such as temperature, time, external force, or pressure to control the size distribution of the generated reinforcements.

The ability to stability suspend nanoparticles within a liquid metal matrix further depends on the balance of attractive and repulsive forces involved, as shown in Figure 24.

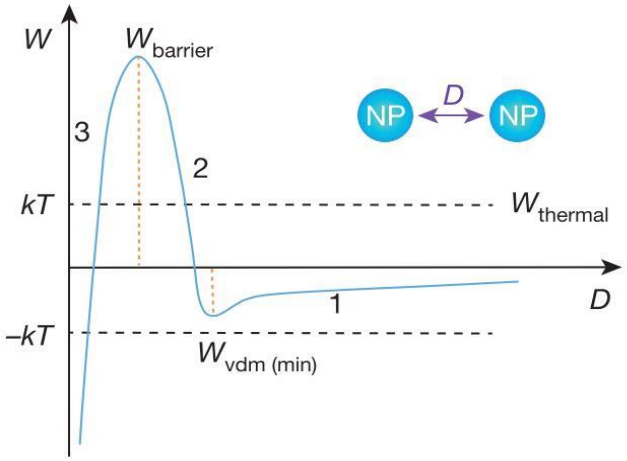

Figure 24: Interaction potential W for nanoparticle dispersion [80]

Here, the energy balance of two nanoparticles, depending on their inter-particle distance D, is plotted. In segment (1), the attractive van der Waals force dominates the particle interaction. Segment (2) represents the touching of the nanoparticles and, therefore, the increase in interfacial energy caused by displacing the liquid in-between particles, generating a particle-particle interface. Lastly, the energy-drop in segment 3 accounts for the reduction of the surface area during particle sintering. It is, therefore, evident that nanoparticles' tendency to agglomerate is governed by the particles van der Walls force and Brownian motion caused by thermal energy (kT). Hamaker quantified this particle-particle attraction by modifying the general Van der Walls formula to the following expression:

$$\theta = \frac{-Ar}{12D^2} \tag{10}$$

In this formulation, θ yields the reduction in Gibbs free energy, while r is the particle radius, D is the distance between particles, and A is the Hamaker constant, an intrinsic material property [87]. For particles suspended in a liquid phase, this expression is expanded to the following relation, which accounts for the intrinsic properties of the surrounding phase:

$$W_{vdw} = -\frac{r(\sqrt{A_{np}} - \sqrt{A_{liquid}})^2}{12D^2} \tag{11}$$

This equation shows that the attractive forces between nanoparticles are dependent on the nanoparticles' Hamaker constant A_{np}, as well as the surrounding media's Hamaker constant A_{liquid} [88]. In order to minimize detrimental clustering effects of nanophases, the material combination shall be chosen where W_{vdw} is minimized and therefore $\sqrt{A_{np}} \approx \sqrt{A_{liquid}}$. Considering this condition, the use of carbide particles in solidification processing of aluminum appears favorable for the low Hamaker constants of oxides, to avoid clustering [89]. Moreover, since a scalable fabrication approach is sought to underline the industrial significance of this study the commonly used processes to incorporate oxide particles in metal matrices, such as ball milling, accumulative roll bonding, or ultrasonic assisted incorporation, are not desirable [19,84,85,90–92]. In the case of TiB_2 and TiC, the literature reports a multitude of in-situ synthesis or ex-situ salt assisted incorporation methods [93–100]. These methods are generally favorable for being largely scalable and guaranteeing a clean particle-matrix surface after incorporation. Besides, the literature reports that both TiB_2 and TiC exhibit sufficient chemical stability when exposed to liquid aluminum [101–103], and the Hamaker constants of aluminum, TiB_2, and TiC, are reported as 266 zJ[104], 256 zJ and 238 zJ [88], respectively. Therefore,

considering equation 11, both particles are expected to show sufficient dispersion within molten aluminum.

2.3.1. Enhancement of properties

It is well known that MMNCs can significantly alter the base materials properties. The introduction of nanoparticles influences the matrix' electrical, thermal, and mechanical behaviors in ways beyond the reach of classical metallurgy. As for the mechanical properties, Wang et al. summarized the mechanisms behind the advancement to be the Hall-Petch effect, load transfer effect, Orowan effect, a thermal mismatch effect, which will be further elucidated in this Chapter [105].

Hall-Petch effect

The mechanism behind the Hall-Petch effect is commonly described as the increase of yield strength of a material with a decrease of its grain size. Here, an increase in the number of grains leads to an increase in grain boundaries, interfaces between crystal structures of usually different lattice orientations. These interfaces will cause dislocations to change their direction while moving through the material, which increases the overall energy needed for a dislocation to move from A to B, compared to a more coarsely grained material. This theory follows the empirical Hall-Petch equation [105]:

$$\sigma_y = \sigma_0 + \frac{K}{\sqrt{d_m}} \quad (1)$$

Where σ_0 represents the materials yield strength, disregarding dislocations, K is a material constant, and d_m represents the materials grain size.

The advantage of nanocomposites over conventional materials regarding this correlation is the constrained grain growth caused by the particles. Nanoparticles pin the advancing grain

boundaries during heat treatment and recrystallization, restricting their movement and therefore restricting grain growth. This effect strongly relies on the amount and size of the particles introduced into the matrix material and is theoretically modeled by the Zenner-Smith pinning equation [106]:

$$d_m = \frac{4\alpha d_p}{3V_p + \beta} \quad (2)$$

Where α and β are material constants, V_p is the volume fraction of nanoparticles incorporated into the matrix, and d_p is the particle size. This relation shows that with the increase of volume fraction of particles and decrease of particle size, the average matrix material grain size d_m decreases. Combining these results with the Hall-Petch effect explains the intrinsic strength increase of MMNCs due to grain refinement.

Load Transfer effect

The load transfer effect describes the shift of an externally applied load from the relatively soft matrix material to the relatively hard and stiff nanoparticles. With this, the incorporated reinforcements are supporting the matrix and enhance the overall material's strength. To quantify this mechanism, Nardone and Prewo modified the shear lag theory to explain a so far unaccounted for increase strength of MMNCs [107].

$$\Delta\sigma_{l-t} = 0.5V_p\sigma_m \quad (3)$$

Where $\Delta\sigma_{l-t}$ is the increase of strength due to the load transfer effect, V_p is the volume fraction of particles incorporated in the matrix material and σ_m the yield strength of the matrix material. For this mechanism to take effect the interfacial bonding between matrix and particle must be strong, requiring among others, compatible lattices of particle and matrix (Zhang, Chen 2008).

Orowan effect

Similar to the previously mentioned Zenner pinning effect, the Orowan effect is explained by the impeded movement of dislocations. However, in this theory, it is not the grain boundaries but the nanoparticles that keep them from propagating. Since the particle is commonly hard and non-sharable, the incoming dislocation front will bend and loop around it. Even for volume fractions as small as 1% and less, of 100 nm nanoparticles, this mechanism becomes pivotal, considering the overall strengthening of the material [105].

$$\Delta\sigma_{Orowan} = \frac{0.13G_m b}{d_p\left[\left(\frac{1}{2V_p}\right)^{\frac{1}{3}}-1\right]} ln\frac{r}{b} \quad (4)$$

Where $\Delta\sigma_{Orowan}$ represents the gain in Orowan strengthening, r is the particle radius, b is the Burger's vector, G is the matrix' shear modulus, and the denominator is a geometrical construct for the distance in-between nanoparticles. This last expression is one of the most significant drawbacks in utilizing $\Delta\sigma_{Orowan}$ to its full extent. It assumes perfect dispersion and distribution of the incorporated reinforcement particle while achieving this state is one of the major challenges in the manufacturing processes elucidated in section "Fabrication methods".

2.3.2. Influence of nanoparticles on solidification processing

In addition to the improved mechanical properties brought by the incorporation of nanophases into metal matrices, the particles have shown to cause unusual solidification behaviors in MMNCs.

Cao et al. found that by incorporating WC particles with an average diameter of 50 nm into the immiscible Zn-8Bi alloy, the segregation of the Bi phase during solidification was controlled. The authors concluded that nanoparticles covered the liquid-liquid interface of the precipitating Bi phases and effectively restricted their growth [108].

The author further discovered a significantly restricted alpha grain growth by nanoparticles in copper, aluminum, and zinc at largely varying solidification rates [109], which is in good agreement with observations made in further studies [110,111]. The beneficial effects of nanoparticles during solidification are not only limited to the growing alpha phases but are further found to modify and refine the morphology of eutectic phases [112–116]

Most strikingly, as mentioned in the introduction, nanoparticles were successfully employed to suppress hot cracking in aluminum A206. With the addition of 1 w% of Al_2O_3, the nanocomposite showed superior resistance to hot cracking compared to conventionally grain refined alloys [21]. Similarly, Martin et al. coated AA7075 feedstock powder with hydrogen stabilized Zirconium nanoparticles, yielding crack-free printed parts with good mechanical performance.

2.3.3. Application of MMNCs in fusion processes

A new take on how to decrease the negative influences that the welding process has on the joined materials and possibly even enhance their overall properties has been pursued lately. The introduction of nanomaterials to the field of welding might enable yet unthinkable possibilities for the manufacturing industry. The approach of introducing particles into the melt pool can be divided into two major categories, as shown in Figure 25.

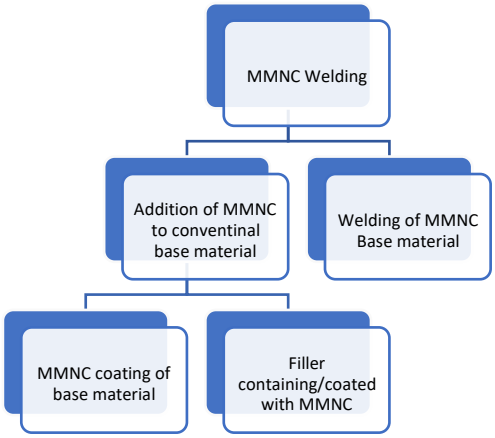

Figure 25 Categories of MMNC welding

Firstly, nanoparticles are introduced into welding procedures by adding them as part of the filler materials, as a coating on the base materials or incorporated into the flux added to the process. It is experimentally shown that the coating of filler materials with nanoparticles, in either GMAW or GTAW, these particles can be successfully introduced into the weld pool and show a remarkable change of properties compared to the fused materials [117–120]. The changes generally bring a refined grain structure of the FZ, increased tensile, and impact strength, increased wear resistance, and lower defects, such as porosities, while as a downside, the addition of nonmetallic reinforcements into the weld pool can lower the corrosion resistance of the joint. It has been shown that these inclusions could work as pitting agents, leading to premature failure [118]. Furthermore, it was shown that the addition of TiO_2 into low alloy steel joints changes the thermodynamic procedures while cooling and shifts the material's phase transformation temperature ranges [121]. One of the concerns with this technique is the low yield of particles being incorporated into the FZ compared to the amount of particles applied to the filler material. During the high energy process of arc welding, a fraction of the particles burn off the surface of the electrode or are simply slung off before penetrating the weld pool. Tseng et al. showed a significant impact of nanoparticles on weld distortion in GTAW welding of UNS S31603 stainless steel [122]. Here, the

nanoparticles were applied to the base material using a SiO_2/methanol solution, which was painted onto the surface before welding. It was revealed that the nanoparticle coating resulted in a 524 % increase of weld depth and a 38 % decrease in angular weld distortion. The second path shown in Figure 12 depicts an alternative way to introduce nanoparticles into the melt pool. Here, the MMNC is not formed during the fusion process, but the filler material already contains incorporated nanoparticles. Fattahi et al. successfully used accumulative roll bonding to fabricate filler rods used for GTAW [14,16,18,19,123]. In this approach, different types of particles such as ZrC, MWCNT, TiO_2, Al_2O_3, and TiC are coated onto sheets of aluminum, as shown in step 1 in Figure 26.

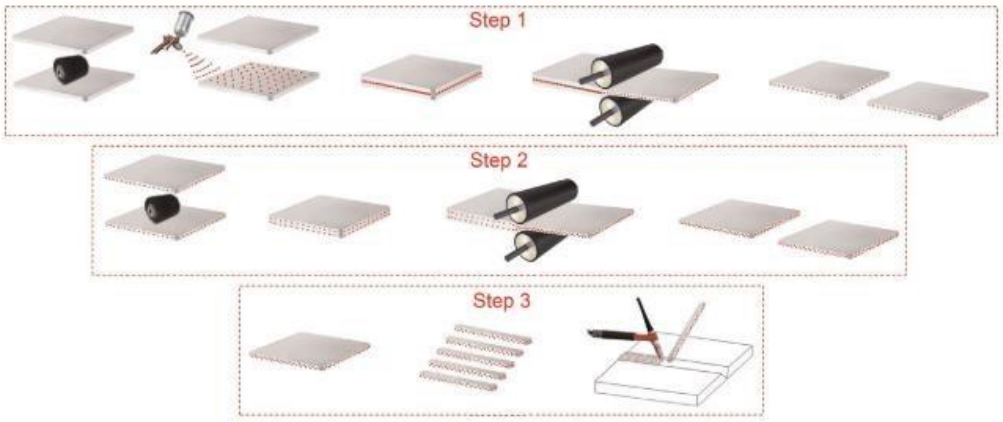

Figure 26 Fabrication of GTAW MMNC filler metals by accumulative roll bonding [18]

Hereafter, the sheets are roll bonded, cut, and roll bonded again, in an iterative process. Experimental results showed that after 10 iterations, the initial particle layer dispersed reasonably well throughout the material.

Utilizing this method, TiC was incorporated into AA 4043 and used to weld AA6061 in v-grove setup. Different amounts of nanoparticle incorporated into the filler rods showed various levels of grain refinement. For AA 6061 welded with 0, 2.5, and 5 wt% TiC filler metal, the measured average grain size of the WM was 38.7 µm, 22.3 µm, and 12.6 µm,

respectively. The Microhardness and tensile strength of the WM increased, as shown in Figure 27.

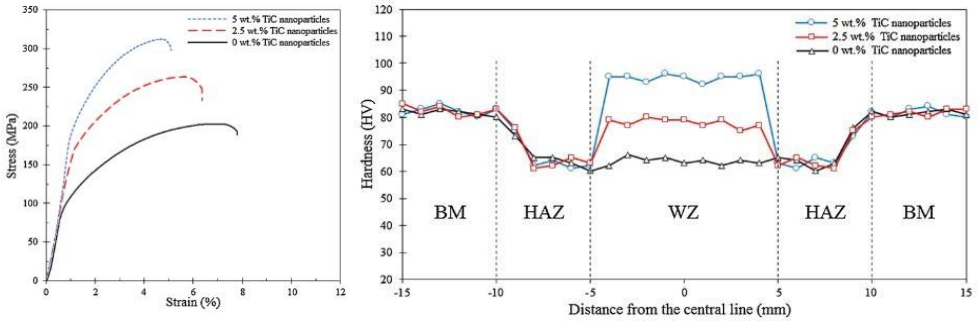

Figure 27 Tensile strength of WM (left) and transversal microhardness of joint (right) [16]

Fattahi et al. furthermore explored ball milling as an alternative solid-state incorporation method [17]. In this study, gas-atomized pure aluminum powder smaller than 20 µm in diameter was mixed with 1.5 wt% MWCNT and milled for 4 hours. The resulting powder was then first cold compacted at 500 MPa and finally hot extruded at 550 °C, yielding a 4 mm in diameter MMNC rod used as a filler. The investigation of a GTAW weld, using the produced wire to join AA1050 base material, showed comparable results, as seen in Figure 14. The hardness of the WM increased by 73 %, whereas in the HAZ, it decreased by 18 % compared to unreinforced WM material. The tensile strength of the WM material increased by almost 90%, while ductility decreased by 25 %.

Ahmadi et al. used the aforementioned roll bonding process to fabricate AA4043 containing 1 wt% ZrC/TiC [14]. The resulting hybrid MMNC filler rods were used for welding AA6061 base material. The microhardness of the WM increased by 23% compared to unreinforced WM material. The tensile strength of the WM material increased by almost 90, while ductility decreased by 25%. Fattahi et al. further showed that in addition to using an Al-Si filler material with 0.5 wt% ZrO2/TiO2, the application of ultrasonic vibration during the welding process further enhanced the microstructure, microhardness, and tensile properties of the

weld metal [123]. Using the ARB approach to incorporate various weight fractions of TiO_2 into AA3003 used as filler metal to weld AA1100, the authors suggested a restriction of growing aluminum α-grains caused by the refractory nanophases. However, except for a reduction in grain sizes with increasing nanoparticle content in the filler material, no supporting evidence for this theory was shown [124].

The third and last branch of Figure 28's diagram displays the category of fusion of MMNC base materials. Ma et al. used laser melting on a Nickel base material reinforced with 4.4 vol. % Al_2O_3 Particles of 50 nm in diameter, to simulate the process of laser welding or polishing [22]. The experimental results showed a significant manipulation of heat distribution and weld profile. Using the same laser processing parameters, pure Nickel base material showed a penetration depth of 1.9 ± 0.2 µm, while the pool depth of Nickel + 4.4 vol. % Al_2O_3 was 3.2 ± 0.2 µm, marking a penetration increase of 68 %. Furthermore, the two samples showed a remarkable difference in their HAZs, illustrated in Figure 15. While pure Nickel was heat-affected to a depth of 8.1 ± 0.3 µm, the MMNCs HAZ shrunk to only 2.7 ± 0.2 µm; a decrease of 77 %.

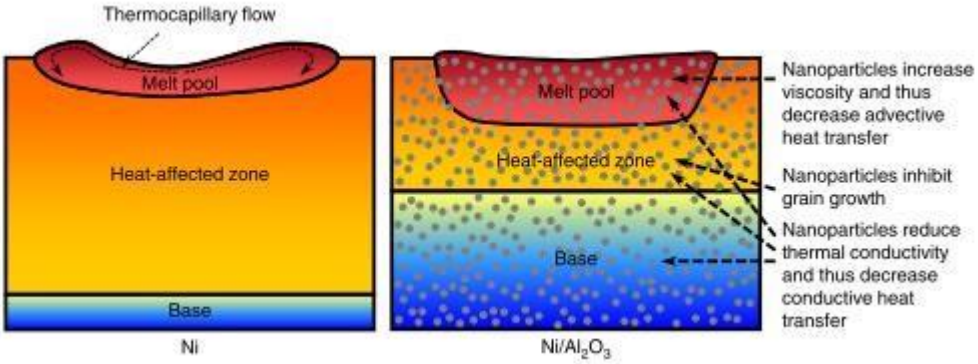

Figure 28: Effect nanoparticles on heat flow in laser melting

Two reasons are pointed out to explain this phenomenon. Firstly, nanoparticles decrease the composite's thermal conductivity and, therefore, reduce the heat flow into the base material,

and secondly, the increased viscosity within the melt pool caused by nanoparticles inhibits thermocapillary heat flow and advective heat transfer.

3 Fabrication and validation of nano-treated filler material

In this study, TiC and TiB_2 nanoparticles were chosen as refractory phases. This chapter outlines the fabrication and preliminary experiments with as-cast nanocomposite filler materials to quantify its effectiveness in the arc welding of AA7075 (Al-5.6Zn-2.5Mg-1.6Cu). These findings guided the design and conduct of the subsequent study in the following chapters.

3.1. Evaluation of TiC and TiB_2

As shown in Chapter 2, TiC and TiB_2 particles have shown sufficient chemical stability within molten aluminum, similar Hamaker constants, favorable wetting angle, and a low lattice mismatch between particle and matrix. Besides, since this study partially aims to solve a long-standing problem in industrial applications for high strength aluminum alloys, an important consideration was the potential to produce the nanocomposite material at an industrial scale. This chapter studies the effect of 0.5 v% and 1.5 v%, TiB_2, and TiC addition to AA7075 used as filler metal to weld AA7075 base metal on the weld metal's microstructure.

3.1.1. Fabrication of nano-treated filler metal

The nanoparticle master alloys were fabricated using established routes found in the literature. Figure 29 shows a schematic of the process used to incorporate TiC nanoparticles into molten aluminum.

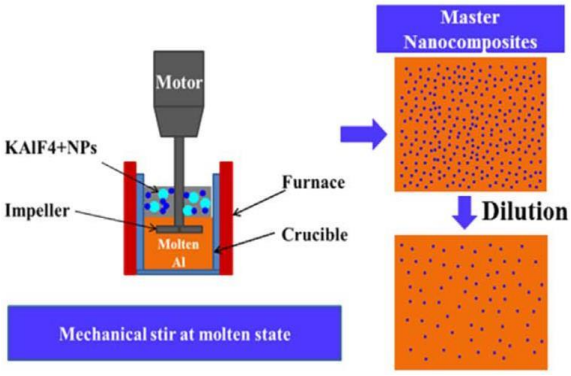

Figure 29: Fabrication route for TiC nanocomposite master [125]

$KAlF_4$ salt was mixed with TiC nanoparticles (TiC, 99+%, 40 – 60 nm, cubic, US Research Nanomaterials, Inc) and poured onto a pool of molten aluminum as discussed by Liu et al. Upon melting, the $KAlF_4$ dissolved the aluminum oxide layer, letting the nanoparticles cross the liquid-liquid interface into the molten aluminum. The process was enhanced by applying mechanical mixing within the aluminum phase. Following this procedure, an aluminum nano-composite master containing 5 v% TiC nanophases was fabricated. In Figure 30, SEM images of the master material are shown.

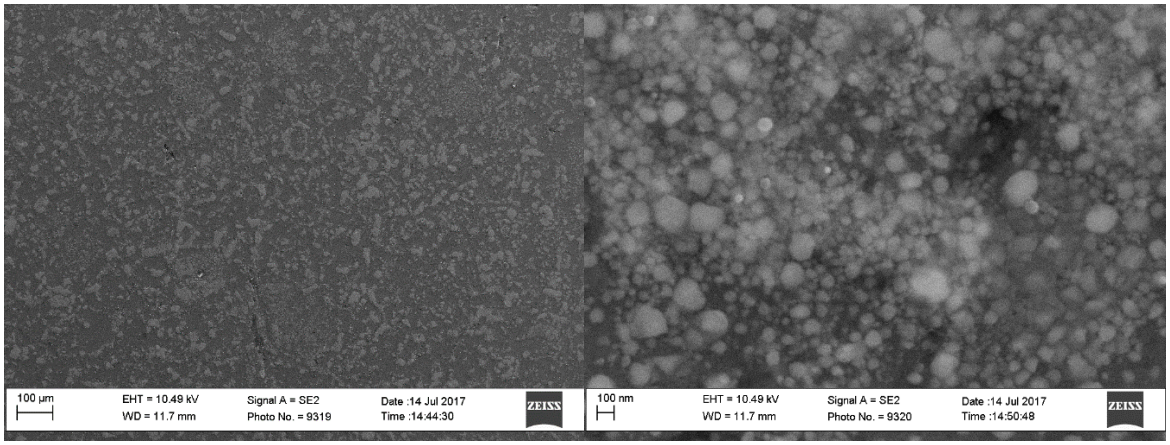

Figure 30 Aluminum with 5 v% TiC master composite

While in Figure 30 (left), uniformly dispersed pseudo-clusters of the nanoparticles, caused by particle pushing effects of the solidifying aluminum grains, are observed, the higher

magnification of the SEM image on the right reveals that the TiC phases within these pseudo-clusters are dispersed and wetted by the aluminum matrix. It can be seen that a small fraction of the TiC particles grew to a size of approximately 100 nm, whereas the majority of nanophases remained within the initial 30 – 60 nm range.

An established method found in the literature was utilized to synthesize the TiB_2 nanocomposite master material by an in-situ synthesis reduction reaction [126–129]. K2TiF6 and KBF4 were premixed and introduced onto a molten aluminum pool. The amounts of salt were chosen to yield a composite containing 5 v% of TiB_2 nanophases. SEM images are shown in Figure 31.

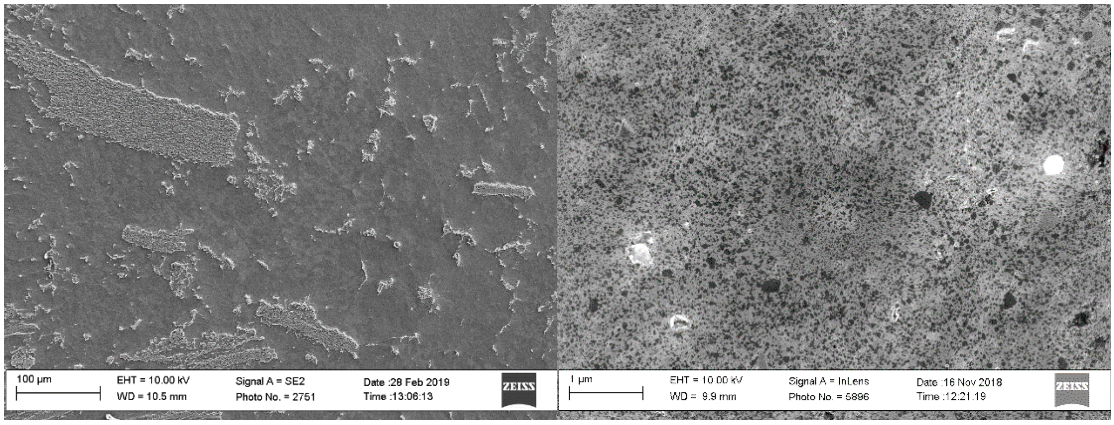

Figure 31 SEM images of aluminum with 5v% TiB_2 master composite

In contrast to the morphology shown for the TiC containing master material, the TiB_2 particles formed large clusters that did not conform with the growing grains of the aluminum matrix. However, at high magnification, the particles within the clusters appeared well dispersed and wetted by the aluminum.

3.2. Fabrication and evaluation of as-cast AA7075-TiC/TiB_2 filler metal

This chapter discusses the fabrication and use of as-cast nanocomposite filler material in the fusion welding of AA7075. It evaluates the impact of varying amounts of reinforcements on

the microstructure of the weld metal and concludes a filler metal design for an in-depth study of nanoparticle effects on hot crack susceptible aluminum alloys.

3.2.1. AA7075 - TiC/TiB_2 filler metal fabrication

The fabricated nanocomposite master materials were diluted into molten aluminum under mechanical mixing to yield volume fractions of 0.5 v% and 1.5 v%, respectively. The materials were subsequently alloyed with the addition of 6 wt% zinc, 2.9 wt% magnesium, and 1.6 wt% copper to match the chemical composition of AA7075 [43] and cast into plates. Microstructure images of the resulting alloys are shown in Figure 32.

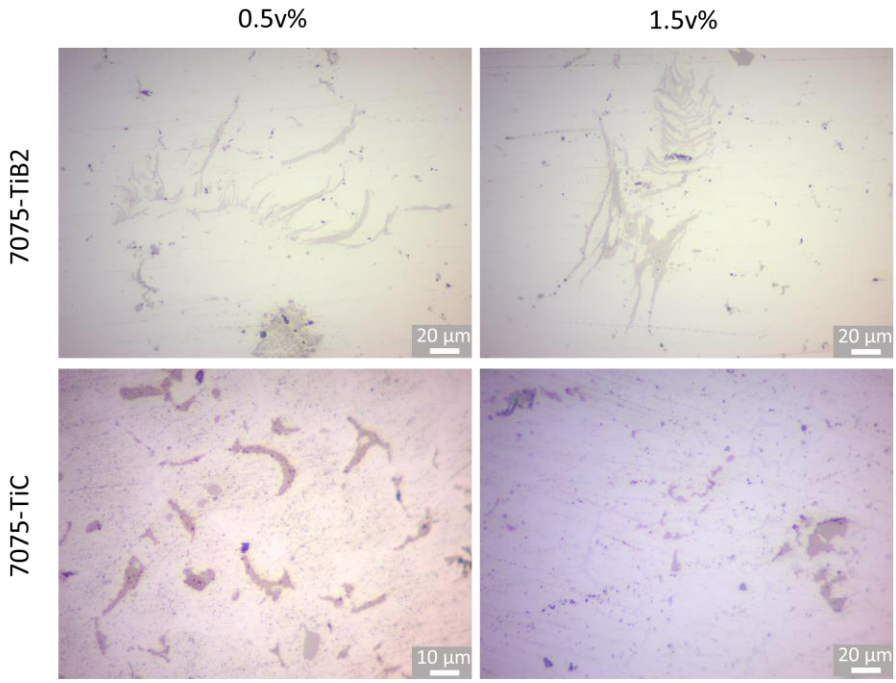

Figure 32 AA7075 filler metal with varying amounts of TiC and TiB_2

It was observed that the TiC bearing alloy showed microscopic clusters formed during solidification by grain boundary pushing. In contrast, both alloys containing TiB_2 showed irregularly shaped clusters, as observed in the synthesized master nanocomposite. It was concluded that these formations most likely did not disperse upon dilution and mechanical mixing but retained their shape throughout the liquid processing of the aluminum matrix.

3.2.2. AA7075 - TiC/TiB_2 filler metal welding experiments

The AA7075 nanocomposite alloys were cut into 3 mm x 3 mm x 150 mm sticks for further use as filler metal in AA7075 GTAW experiments. The microstructure of welds performed using AA7075-0.5 v% TiC, and AA7075-1.5 v% TiC are shown in Figure 33.

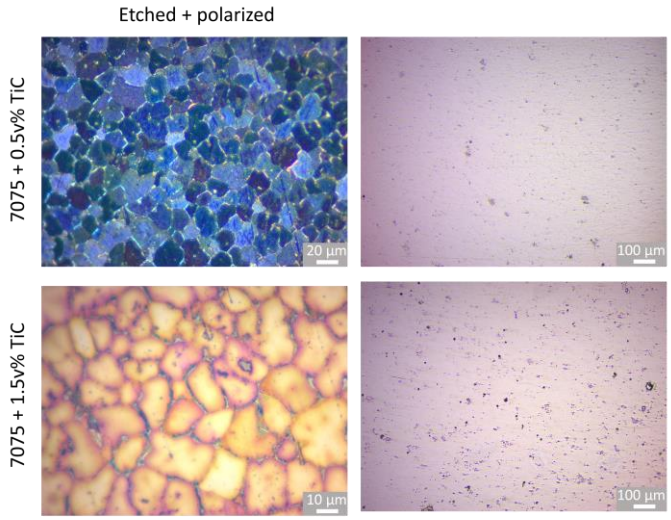

Figure 33 Grain morphology of welds performed with AA7075-0.5v% TiC and AA7075-1.5v% TiC.

Both weld metals showed a homogeneous grain structure of globular grains with minimal dendritic features and smooth grain boundaries. Choi et al. found this grain structure desirable to mitigate hot cracking in A206 aluminum cast alloy [21]. The unpolarized micrographs showed a limited occurrence of TiC micro clusters dispersed throughout the weld metal.

In contrast, the weld metal cross-sections of samples welded with filler metal containing TiB_2, presented in Figure 34, showed a less modified grain structure. While both alloys showed appreciable grain refinement, the expected morphology control was not observed. The weld performed with AA7075-1.5 v% TiB_2 as filler metal exhibited an equiaxed grain morphology with deep dendrite branching. In the cross-section containing AA7075-1.5 v% TiB_2 a mix of equiaxed dendritic and dendritic grain growth was observed. Moreover, the unpolarized micrographs show similar TiB_2 artifacts, as previously observed in the nanocomposite master material and alloyed filler metal.

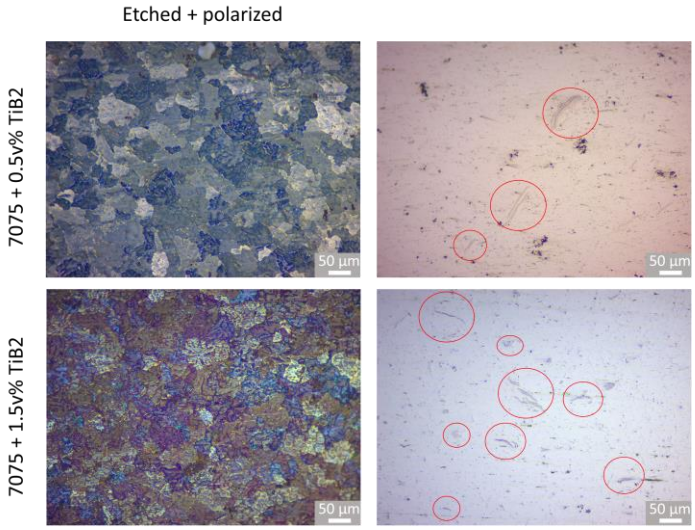

Figure 34 Grain morphology of welds performed with AA7075-0.5v% TiB_2 and AA7075-1.5v% TiB_2

While the structures are reduced in size, it is hypothesized that the features observed within the as-cast filler metal fractured to smaller pieces during the high temperature, high energy processing but did not fully disperse within the weld metal.

3.2.3. Discussions

This chapter is to be seen as a first-order approximation to evaluate the effectiveness of different volume percentages of TiC and TiB_2 nanoparticles on the grain morphology modification of a hot crack susceptible aluminum alloy. While both evaluated filler metals containing TiC showed a desirable morphology modification, the alloys containing TiB_2 did not meet the expectations. The sample containing 1.5 v% of TiB_2 showed a relatively refined grain structure, whereas the development of an equiaxed dendritic morphology was not suppressed. Further, the sample containing 0.5 v% exhibited a mix of equiaxed dendritic and dendritic grain growth. However, since a fraction of the particles appeared to remain clustered throughout the various processing steps, the actual effectiveness of dispersed TiB_2 nanoparticles on the alloys grain morphology was not determined. It was therefore concluded that the fabricated filler metals have to be subjected to severe plastic deformation to guarantee a uniform dispersion before

conducting extensive testing. Including this additional processing step, a non-biased study with identical initial conditions for both systems is possible.

3.3. Filler material fabrication

Since the dispersed 0.5 and 1.5% TiC particles both caused the desired morphology change, a rational design of 0.8 v%, refractory nanophases within the filler metal was chosen and extruded for both systems to compare the effect of dispersed TiC and dispersed TiB_2.

The study was further expanded to include not only AA7075 but also AA2024 and AA6061 for being commonly applied aluminum alloys with high susceptibility to hot cracking, as discussed in the introduction chapter 1. The similar filler metals designed to weld latter aluminum alloys designed were AA7075-0.8 v% TiC (7075NT-C), AA7075-0.8 v% TiB_2 (7075NT-B), AA2024-0.8 v% TiC (7075NT-C), AA2024-0.8 v% TiB_2 (2024NT-B), AA6061-0.8 v% TiC (6061NT-C) and AA6061-0.8 v% TiB_2 (6061NT-B). With these filler metals, the effect of nanoparticles on the intrinsic crack susceptibility on the chemical composition of the parent material and the benefits regarding mechanical performance and heat treatability of the resultant welded joint shall be studied. Furthermore, the dissimilar filler metal ER5356 was enhanced with TiC and TiB_2 to yield ER5356-0.8 v% TiC (ER5356NT-C) and ER5356-0.8 v% TiB_2 (ER5356NT-B) to evaluate the effects of nanoparticles on mechanical properties and hot crack susceptibility when incorporated into a commercially applied filler metal composition. In the nomenclature used, NT abbreviates the term nano-treated indicating a low volume fraction of nanoparticles incorporated into the respective alloy, while C and B identify TiC and TiB_2, respectively, as the incorporated refractory nanoparticle.

After alloying constituent elements and diluting the stated volume fraction of nanoparticles into molten aluminum, the filler metals were cast into ingots and hot extruded to yield filler metal

rods of 2.4 mm in diameter. Figure 35 shows representative images of the extruded filler metal rods for 7075NT-B and 7075NT-C.

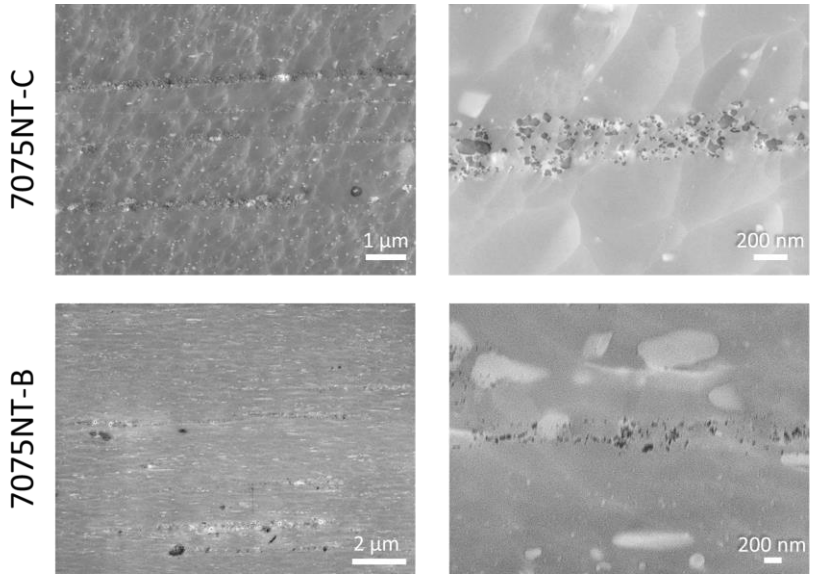

Figure 35 Dispersion of nanophases after extrusion for 7075NT-B and 7075NT-C

It is shown that, unlike discussed in the previous section, by employing severe plastic deformation, both TiC and TiB_2 containing alloys do not show signs of macroscopic or microscopic particle agglomeration. In both systems, eventual pseudo-clusters present after synthesis or casting formed finely dispersed particle rich strips during hot extrusion. The phase compositions of the filler metals' cross-sections were analyzed using X-ray diffraction (XRD). Corresponding peaks of TiC and TiB_2 confirmed the presence of nanoparticles within the extruded NT-C and NT-B alloys, respectively. The resulting XRD plots and matched peaks can be found in attachment A.

The actual volume fraction of nanoparticles within the filler metal was derived from quantitative Energy-dispersive X-ray spectroscopy (EDS) mappings of the detected titanium signal. Since the SEM analysis of the extruded weld metal further revealed a small fraction of Al_3Ti phases indicated by red circles in Figure 36a, the total titanium signal was corrected by using image analysis, as shown in Figure 36b.

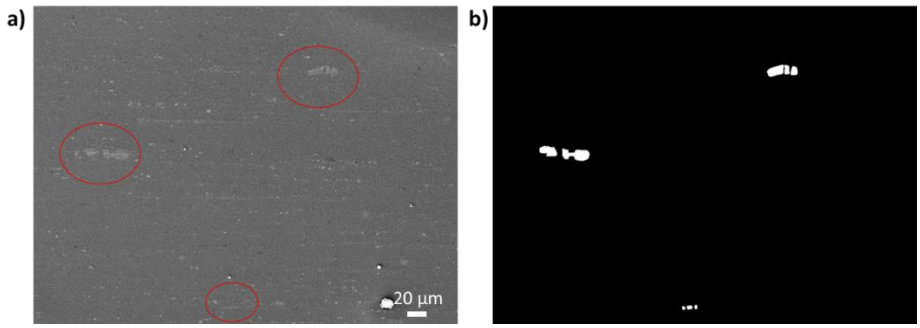

Figure 36 Typical Al_3Ti phases observed in SEM micrographs (left) and image analysis of latter phases (right)

The overall titanium signal was reduced by the fraction corresponding to the detected fraction of Al_3Ti, and the resulting derived volume fractions of TiB_2 and TiC, respectively, are shown in the last column of Table 1.

Table 1 Detected volume fractions of TiB_2 and TiC

Filler metal	Ti w%	Ti (TiC/Tib2) v%	Fraction of Al3Ti	TiC/TiB2 v%
7075NT-C	0.99	0.802	0.188	0.6576
7075NT-B	0.86	0.82	0.04	0.7134
2024NT-C	0.95	0.798	0.142	0.66256
2024NT-B	0.83	0.75	0.08	0.6525
6061NT-C	1.04	0.865	0.175	0.7093
6061NT-B	0.89	0.82	0.05	0.7308
5356NT-C	0.97	0.774	0.196	0.63468
5356NT-B	0.88	0.77	0.11	0.6699

4 Effect of nano-treated filler material on microstructure and mechanical performance of high strength aluminum alloys

This chapter investigates the influence of nanoparticles on the mechanical properties and microstructure of welds performed with nano-treated filler metal. The materials discussed in Chapter 3 are used for welding their respective commercial base alloys. Also, 5356NT-C and 5356NT-B filler rods are explored in the welding of AA6061 as an alternative to its widely applied commercial counterpart ER5356. Further, the response of the resulting welds to a Post Weld Heat Treatment (PWHT) procedure is evaluated.

4.1. Methods

4.1.1. Welding of high strength aluminum alloys

The welding experiments were conducted according to the schematic illustrated in Figure 37. Two 3.17 mm (1/8”) thick aluminum alloy sheets (rolled AA7075, AA2024, AA6061, McMaster Carr) sized 152.4 mm (6”) in length and 76.2 mm in width (3”) were beveled at the long sides at 45˚. The plates were placed onto a 6.34 mm (1/4”) thick, square (152.4 mm *152.4 mm) copper backing plate for enhanced cooling. The backing plate had a 6.34 mm wide and 1 mm deep notch machined along the weld seam to allow for full penetration. Before welding the backing plate, aluminum alloy sheets and filler rods were thoroughly cleaned with acetone to

remove grease and minimize the occurrence of gas porosities in the weld metal.

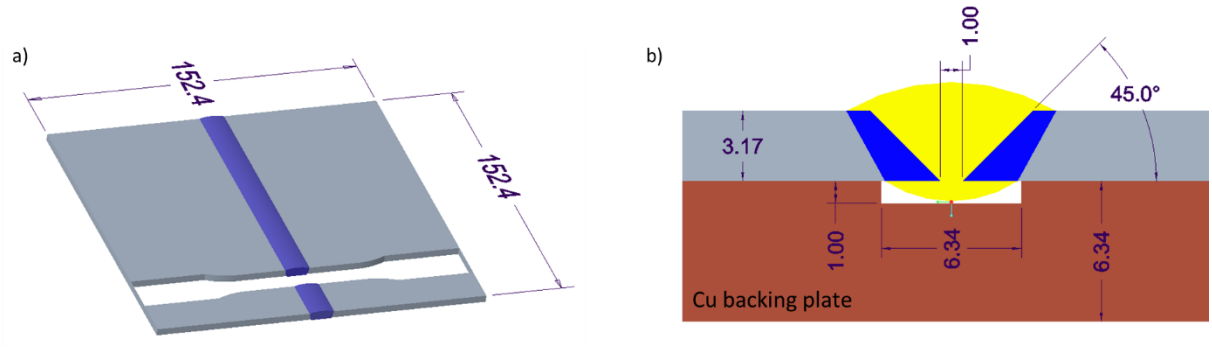

Figure 37 Schematic of the welding setup

The aluminum alloy sheets were restrained onto the backing plate with toggle clamps, leaving a 1 mm root gap. The dilution of the percentage of filler metal and base metal was determined by measuring the weld bead geometry after welding. In Figure 37b, the amount of filler metal in the weld metal is shown in yellow, while the blue area accounts for the amount of base metal molten during the welding process. The composition of the weld metal resulted in approximately 69 % filler metal and 31 % base metal.

The welding process was conducted using an ESAB Rebel EMP 205ic AC/DC power source and a linear welding tractor. The sheets were first tack welded at both ends using the experiment's respective filler rod. The welds were performed using a size 5 ceramic cup, 2.4 mm 2 % lanthanated tungsten electrode, an electrode gap of 2 mm, resulting in a welding voltage of 14.5 – 15.5 Volts. The welding tractor was set to a forward speed of 100 $\frac{mm}{min}$ and the wire was manually fed to maintain the electrode gap between the electrode and melt pool. The power source's parameters were set to AC TiG, 200 Hz AC frequency, 70 % balance, and 25 cfh Argon flow rate. Due to differences in thermal conductivity regarding the base metals AA7075, AA2024 and AA6061 (130 $\frac{W}{m*K}$, 121 $\frac{W}{m*K}$ and 167 $\frac{W}{m*K}$, respectively); the welding current was adjusted to 145 A, 150 A, and 165 A, respectively, to yield a consistent weld bead geometry. The fused aluminum alloy sheets welded with and without nano-treated filler metal

were processed using an AgieCharmilles CUT 200 wire EDM machine for further characterization and testing. 7 transversal tensile bars (Orientation indicated in Figure 37a) were cut from the specimen. The top and bottom of the tensile bars were milled flat using a CNC mill according to ASTM E8 to ensure consistent test results. Selected samples were subjected to a PWHT. The heat treatment conditions can be found in Table 2.

Table 2 Post Weld Heat Treatment conditions [130]

Alloy	Solution heat treatment		Precipitation heat treatment		Temper designation
	Metal temperature, ˚C	Time, h	Metal temperature, ˚C	Time, h	
AA7075	480	1.5	120	24	T6
AA2024	496	1.5	-	-	T4
AA6061	530	1.5	160	18	T6

At the end of the solution heat treatment step, the tensile bars were immediately quenched in water at room temperature. The solutionized 2000 series samples were naturally aged for 10 days before characterization.

4.1.2. Characterization

4.1.2.1. Mechanical properties

Tensile testing: The two tensile bars closest to start and end of the weld, respectively, were subjected to PWHT before testing, while the 3 remaining specimens were taken from the center portion of the fused aluminum alloy sheets were tested in as-welded condition. The specimens were tested using a strain rate of 0.01 $\frac{\frac{mm}{mm}}{min}$ and the strain was measured using a 50 mm extensometer.

Microhardness: The center slugs taken from in-between the tensile specimen after wire EDM cutting were used for microhardness measurements. The vertical transversal surfaces of the slugs were ground using 240, 400, 600, 800, and 1200 grid SiC abrasive paper followed by polishing with 0.3 μm and 0.05 μm polishing solution (Allied High Tech Products, Inc.). The

Vickers Hardness tests were conducted using a Microhardness Tester (LM800 AT) under 200 gf with a dwell time of 10 s. Two parallel lines of indentations were performed at the center of the sample's thickness, ranging from the center of the weld metal past the materials HAZ. The placement is indicated in Figure 38.

Figure 38 Schematic of microhardness measurement

The spacing between the lines was 318 μm, while the transversal spacing in-between indentations was 635 μm. The respective two values of equal distance from the weld metal were averaged.

4.1.2.2. Microstructure

The microstructure of the welded specimen was characterized using optical microscopy (OM), scanning electron microscopy (SEM), energy dispersive X-ray spectroscopy (EDS), focused ion beam (FIB), and transmission electron microscopy (TEM). Analogous to the microhardness characterization, the samples for microstructure characterization were center slugs of the welded aluminum alloy sheets taken after wire EDM cutting of tensile bars.

Moreover, the same grinding and polishing procedure was used to reveal the weld beads microstructure. The two cross-section orientations prepared are illustrated in Figure 39.

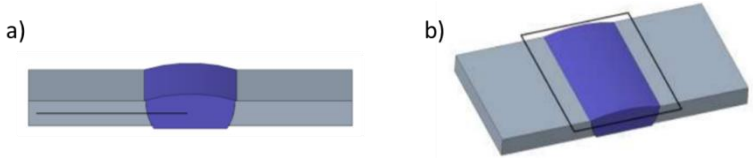

Figure 39 Types of cross-sections prepared for microstructure characterization a) transversal vertical cross-section, b) transversal horizontal cross-section

To expose the materials intergranular segregations using optical microscopy, the samples were submerged for 5 s in Weck's Reagent (100 ml DI water, 4g $KMnO_4$, 1g NaOH) [131]. To reveal the material's primary grain structure, electrolytic etching was employed. The samples were submerged in Barker's Reagent (200 ml DI water, 5 mL HBF_4 (48%)) at 30 V for 1 – 2 minutes. A polarization filter was used to observe the different lattice orientations of grains and therefore generate grain contrast. The grain size was determined using the Intercept Procedure described in ASTM E112 – 13.

4.2. Results

With the methods discussed in the previous section, welds were performed and characterized. In the following, the resulting microstructures and their impact on the welding joints' mechanical properties are presented and discussed.

4.2.1. Microstructure

4.2.1.1. AA7075

Figure 40 shows the weld metal cross-sections of AA7075 base metal welded with 7075NT-C, 7075NT-B, and AA7075 as filler metal. A stark contrast appears between the grain sizes and morphology of the nano-treated and pure weld metals. Since the experiments were performed relatively low welding speed and heat input, the appearance of the weld metal welded with pure AA7075 as filler conforms with the G/R relation shown in Figure 17.

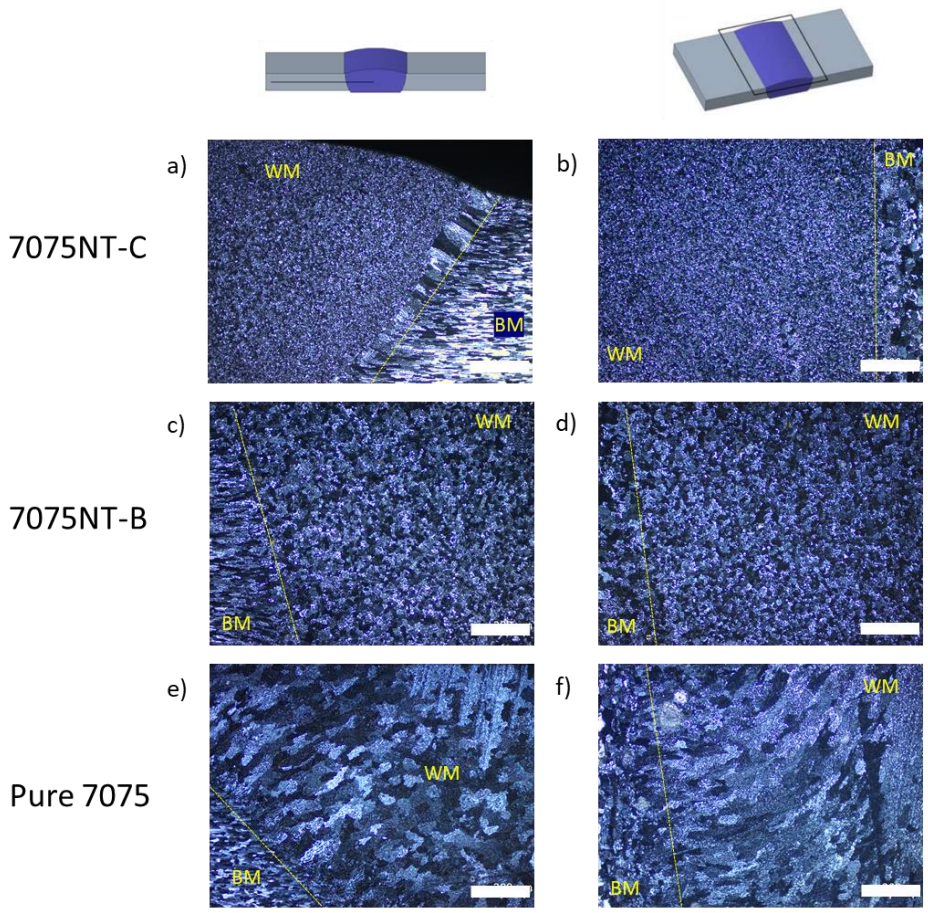

Figure 40 Polarized images of cross-sections of AA7075 welded with different filler metals. a-b) 7075NT-C, c-d) 7075NT-B and e-f) AA7075. All scale bars represent 200 µm

Due to the low welding speed, epitaxial grain growth caused by low constitutional supercooling is favorable at the liquid-solid interface, and cellular dendritic grain growth is observed throughout the WM. The region adjacent to the fusion line exhibit a shorter, curved morphology caused by the solidification direction and geometry of the round/elliptic geometry of the melt pool. At the center section of the weld metal, the liquid-solid interface is approximately perpendicular to the welding direction and therefore leading to actual columnar dendritic growth of high aspect ratio grains trailing the heat input.

Both nano-treated filler materials exhibit highly refined, equiaxed grains. The occurrence of these grains is homogenous throughout the WM, and no segmented appearance is observed. Due to microscopic fluctuations of the unmixed zone, a thin film of base metal that does not

mix with the filler metal at the liquid-solid interface, limited epitaxial grain growth is randomly observed at the interface. Figure 40a is an example of this manifestation. A thin film of columnar grains with a maximum thickness limited to 80 μm, which sharply transitioned to a fine spherical grain morphology was observed [28]. This observation is not limited to 7075NT-C but occurred randomly for all nano-treated filler metals across the 7000, 2000, and 6000 systems. The overall resulting average grain sizes within the WM are shown in Figure 41.

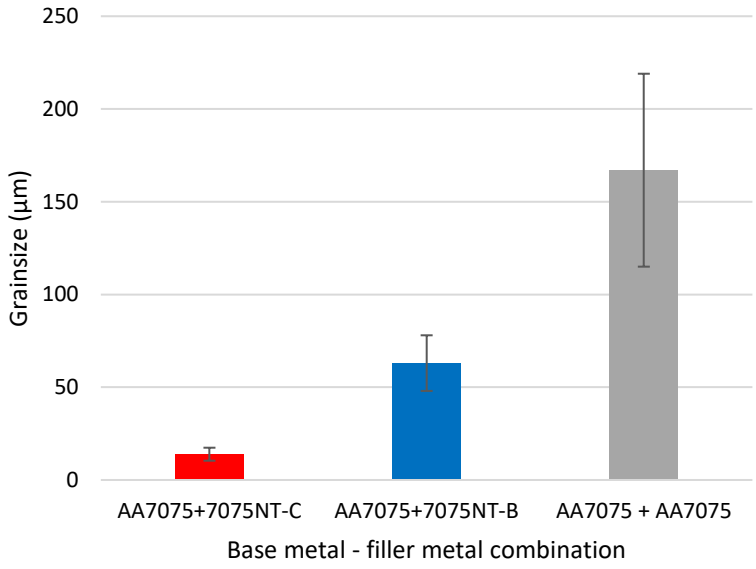

Figure 41 Grain sizes in the WM of AA7075 welding experiments

Both 7075NT-C and 7075NT-B filler metals cause significant grain refinement within the WM compared with welds performed with AA7075 filler metal. The grain size of 167 ± 48 μm shown in the graph reflects the curved grained section adjacent to the fusion boundary since grains in the center section show an indefinitely long, columnar dendritic structure. With 7075NT-C and 7075NT-B, the grain size is shown as 13.3 ± 2.6 μm and 63 ± 8.4 μm, respectively. While the WM of the containing TiC solidified in a highly refined spherical α-grain morphology with no dendritic sub-grain structure visible, the weld performed with 7075NT-B showed less refinement, and the primary aluminum grains exhibited a clear equiaxed dendritic morphology.

4.2.1.2. AA2024

The resulting weld metal microstructure of welds performed using AA2024, 2024NT-C, and 2024NT-B as filler metal to fuse AA2024 base metal sheets are shown in Figure 42. Similar to the observations in the 7000 system, the morphology of welds containing nanoparticles strongly differ from WM only containing pure AA2024.

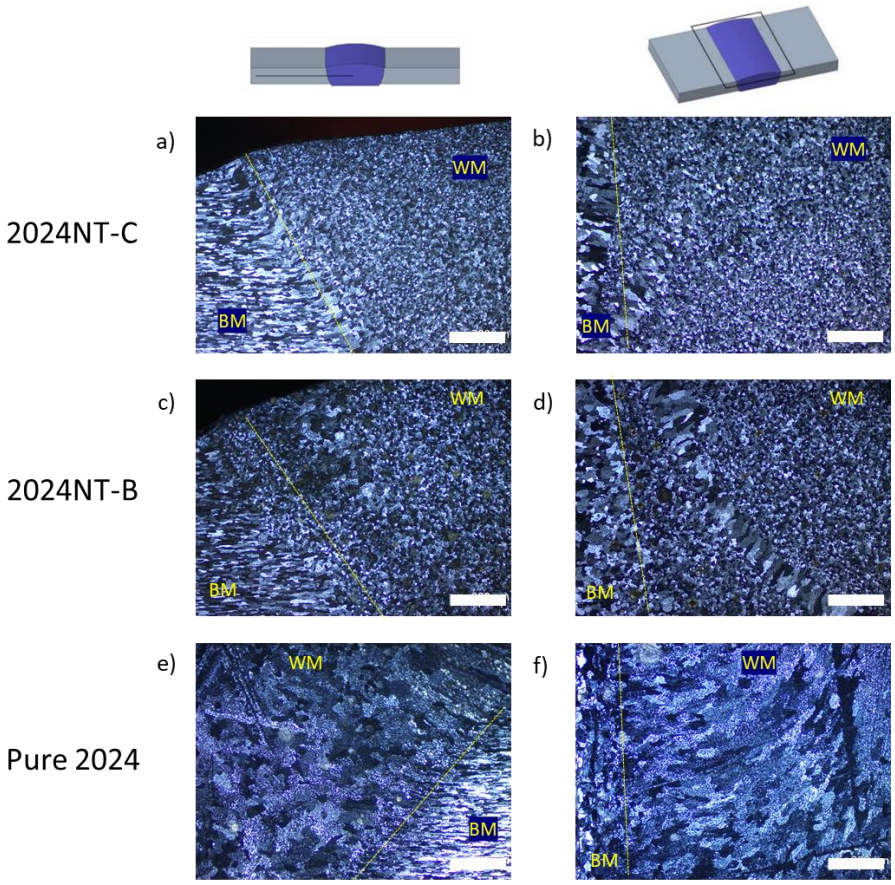

Figure 42 Polarized images of cross-sections of AA2024 welded with different filler metals. a-b) 2024NT-C, c-d) 2024NT-B and e-f) AA2024. All scale bars represent 200 µm

As shown in the previous section, the horizontal cross-section of the latter WM shows a segmented appearance with curved columnar dendrites adjacent to the fusion boundary (center portion of Figure 42f) and the transition to indefinitely long columnar dendrites in the center of the WM (right-hand of Figure 42f). Both welds performed with 2024NT-C and 2024NT-B show a uniform grain distribution in vertical (Figure 42a,c) and horizontal (Figure 42c,d)

orientation. Figure 42c and d further show thin streaks of unmixed base material flushed into the melt pool, causing arms of enlarged grains branching into the WM. This phenomenon randomly occurred throughout all welded 7000, 2000, and 6000 systems and did not show detrimental effects [28]. Figure 43 shows an average grain size of the weld performed with pure AA2024 as the filler material with 153 ± 40 µm.

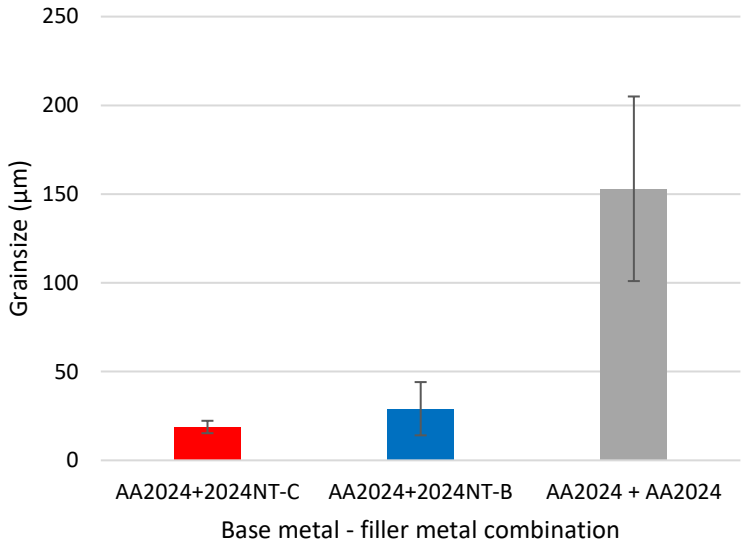

Figure 43 Grain sizes in the WM of AA2024 welding experiments

Since the WM, similar to the pure 7000 system WM, exhibited a segmented grain morphology with indefinitely long columnar dendrites in the center portion (right-hand of Figure 42f), the grain size evaluation was limited to the curved segment adjacent to the fusion line. The uniform WM observed in welds containing TiC and TiB_2 show a highly refined α-grain structure with grain sizes of 19.8 ± 2.1 µm and 29.1 ± 7.8 µm, respectively.

4.2.1.3. AA6061

Figure 44 shows etched cross-sections of AA6061 base metal sheets welded with AA6061, 6061NT-C, and 6061NT-B as filler metals. In the horizontal cross-sections (Figure 44b, d, f), a gradual transition from directional dendritic grain growth, in the case of AA6061 as filler metal,

to an equiaxed spherical grain morphology when welding with 6061NT-C as filler metal. It is noted that unlike in the 2000 and 7000 series systems, the use of TiB_2 as refractory nanophases in the filler metal did not entirely eliminate the occurrence of directional grain growth.

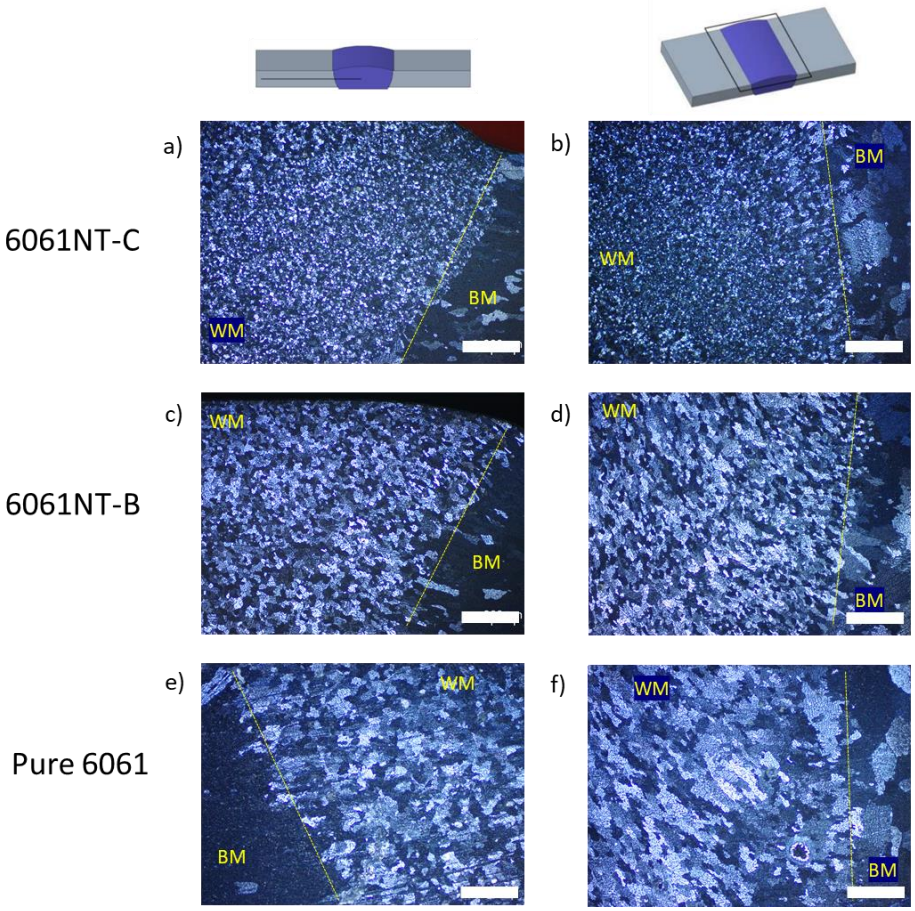

Figure 44 Polarized images of cross-sections of AA6061 welded with different filler metals. a-b) 6061NT-C, c-d) 6061NT-B and e-f) AA6061. All scale bars represent 200 μm

While 6061NT-B refined the aluminum α-grains, the horizontal cross-section shown in Figure 44d reveals elongated grains directionally growing from the solid-liquid interface. The resulting grain sizes of this study are shown in Figure 45.

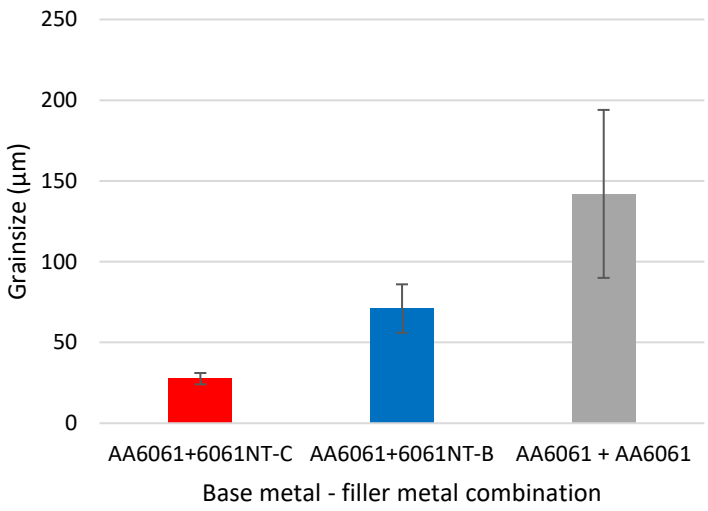

Figure 45 Grain sizes in the WM of AA6061 welding experiments

The average grain size for AA6061 used as filler metal is 142 ± 52 µm. It is noted that unlike the pure base metal welds in the 2000 and 7000 systems, this grain size reflects all grains within the WM since no segmentation is observed. The grain sizes of nano-treated WMs using TiC and TiB_2 are 21.1 ± 1.3 µm and 59.6 ± 8.3 µm, respectively.

4.2.2. Microhardness Properties

This chapter displays microhardness measurements of the 2000 and 7000 series welds with their respective nano-treated filler metal. Since AA6061 is considered commonly weldable using commercially available filler metals, such as ER5356 (Al-5Mg) and ER4043 (Al-5.3Si), the characterization of additional reference welds is included in the 6000 systems study.

4.2.2.1. AA7075

In Figure 46, the microhardness measurements of AA7075 welds with various filler metals are displayed. In as-welded condition, AA7075 base material welded with AA7075 filler metal shows a reference hardness of 115.4 ± 2.3 HV. This hardness slightly increases with the use of nano-treated filler metal. 7075NT-C shows the highest average WM hardness of 125.1 ± 1.4

HV, while the use of 7075NT-B results in a hardness of 122.4 ± 3.1 HV. The increase in hardness can be attributed to the strengthening effects introduced in Chapter 2. Due to the low volume fraction and the subsequent filler metal/base metal dilution of 70 %, the nanoparticle strengthening effects introduced are marginal. The slight increase in hardness is attributed to grain boundary strengthening.

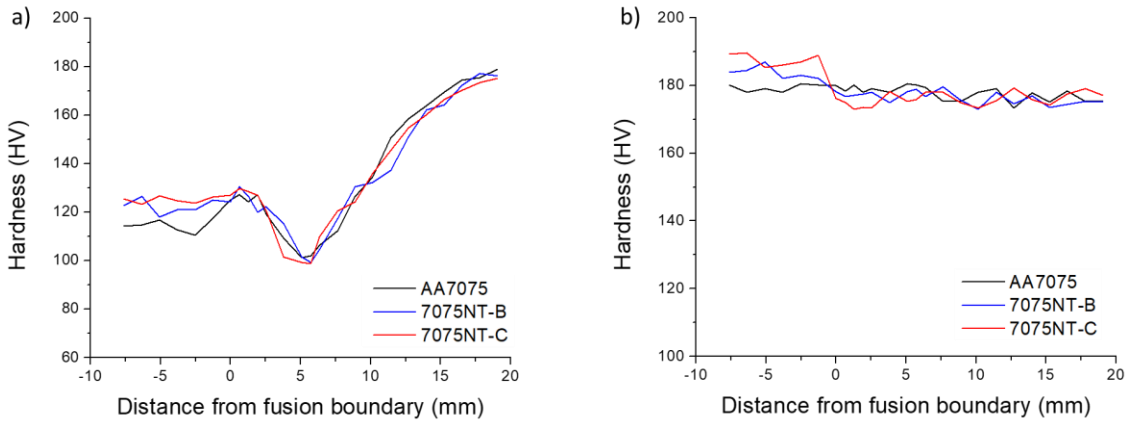

Figure 46 Microhardness mappings for AA7075. a) As welded, and b) PWHT (T6)

The heat-affected zone in the positive regime of the x-axis shows a typical hardness profile of a heat affected, precipitation-hardened aluminum alloy, discussed in detail in section 4.3, and remains unaffected by nanoparticles in the WM.

The hardness of the WM in PWHT condition shown in Figure 46b exhibits a similar trend. The weld performed with AA7075 as filler metal recovered to 179.1 ± 2.3 HV, indicating that the loss of strengthening elements during the welding process. The hardness of the WM containing 7075NT-C was measured as 187.5 ± 1.6 HV, and the weld containing 7075NT-B measured 183.8 ± 1.8 HV, exceeding the strength of the base metal. It is found that by employing nano-treated filler metal, the hardness of the WM exceeds the hardness in the materials HAZ in as-welded condition and the hardness of the recovered base material in PWHT condition.

4.2.2.2. AA2024

Figure 47 shows the hardness profiles AA2024 base metal welded with AA2024, 2024NT-B, and 2024NT-C filler metal. The typical soft spot observed in the HAZ of precipitation-hardened aluminum alloys showed no significant variation for the three filler metals investigated. The weld performed with pure AA2024 as filler metal exhibited the lowest WM hardness of 96.6 ± 2.2 HV. With the use of 2024NT-B, the hardness was increased to 98.5 ± 1.9 HV, while the WM further increased with the use of 2024NT-C and reached a value of 102 ± 1.6 HV.

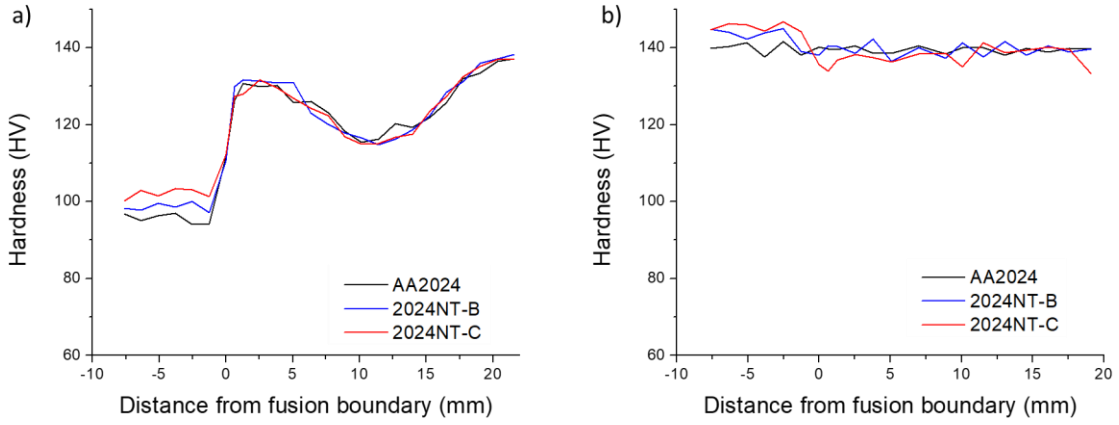

Figure 47 Microhardness mappings for AA2024. a) As welded, and b) PWHT (T4)

In PWHT condition, the hardness of all samples significantly recovered due to the restoration of the strengthening precipitations. For the weld performed with AA2024 as filler metal, the WM hardness reached 139.8 ± 1.6 HV, which is in good agreement with the hardness of the recovered base metal. With the use of nano-treated filler metal, the WM hardness exceeded the base metal level and reached a value of 143.1 ± 2.3 HV for 2024NT-B and 145.4 ± 1.1 HV for 2024NT-C.

4.2.2.3. AA6061

The hardness profiles obtained in welding experiments of AA6061 with 6061NT-B and 6061NT-C are found in Figure 48. Since AA6061 is readily weldable using the commercial

filler metals ER5356 (Al-5Mg) and ER4043 (Al-5Si) to mitigate the materials hot crack susceptibility, these filler metals were included as references, as well as the nano-treated 5356NT-B and 5356NT-C filler metals. It is seen that welds performed with ER5356 and ER4043 show the lowest WM hardness with 60.5 ± 1.3 HV and 56.8 ± 1.7 HV, respectively. At 63.9 ± 1.9 HV, the hardness of the weld performed using 5356NT-B was within close range of the weld only containing pure AA6061, which measured 64 ± 0.9 HV. The hardness recorded for 5356NT-C showed a slight increase in hardness over its TiB_2 bearing counterpart at 66.6 ± 1.4 HV. The highest WM hardness values were obtained for cross-sections welded with 6061NT-B and 6061NT-C, at 70 ± 2.4 HV and 73.6 ± 2.0 HV, respectively. As observed in the 7000 and 2000 series' hardness, the choice of filler metal did not affect the base metal's hardness within the HAZ.

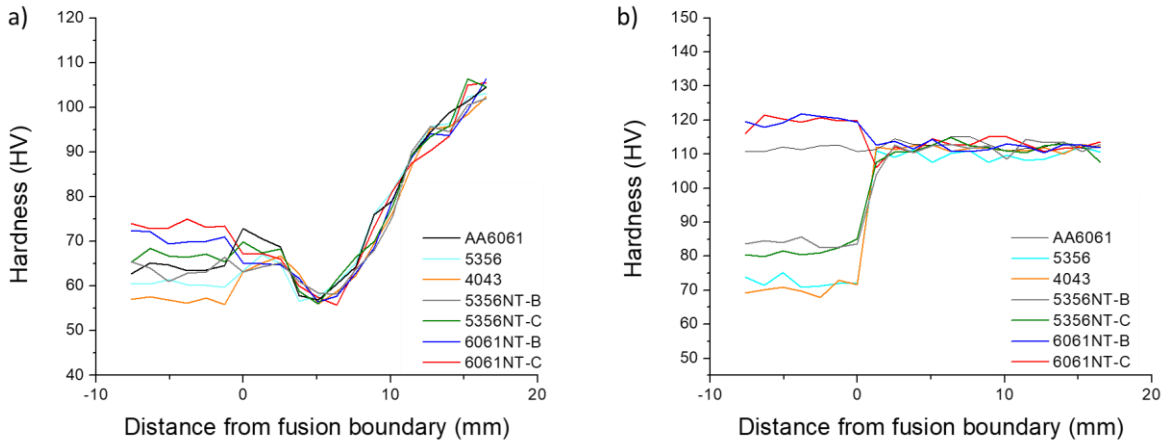

Figure 48 Microhardness mappings for AA6061. a) As welded, and b) PWHT (T6)

In PWHT condition, the dilution of strengthening phases in welds performed with dissimilar filler metals becomes apparent. While ER4043 and ER5356 showed the lowest response to heat treatment with hardness values of 70.6 ± 1.7 HV and 72.5 ± 1.7 HV, respectively, the nano-treated aluminum-magnesium filler metals showed an increased hardness of 81 ± 1 HV for 5356NT-C and 83.8 ± 1.2 HV for 5356NT-B. Correspondingly to the data presented for the

2000 and 7000 series, the WM's hardness for welds performed with 6061NT-B and 6061NT-C exceeded the base metal's hardness with values of 119.8 ± 1.9 HV and 120 ± 1.5 HV, respectively. The hardness of the WM welded with AA6061 recovered to the base metal level with 111 ± 0.8 HV.

4.2.3. Tensile Properties

Transversal tensile bars, as shown in Figure 37, were cut from sheets fused with NT-B and NT-C filler metal to evaluate the joints' mechanical performance. In addition, for AA6061, the commercial filler metals ER4043 and ER5356 were included as a reference.

4.2.3.1. AA7075

Figure 49 shows typical stress-strain curves recorded for AA7075 welds performed with 7075NT-B and 7075NT-C as filler metal. In as-welded condition, it was found that the tensile specimen showed limited ductility. A typical sample for 7075NT-B fractured at an elongation of 0.65% at 317 MPa. The yield strength was recorded as 305 MPa. 7075NT-C typically fractured at 1.2 % elongation at an ultimate tensile stress of 359 MPa, exhibiting a yield strength of 318 MPa. All samples tested in as-welded condition fractured within the WM or the fusion boundary between WM and base metal.

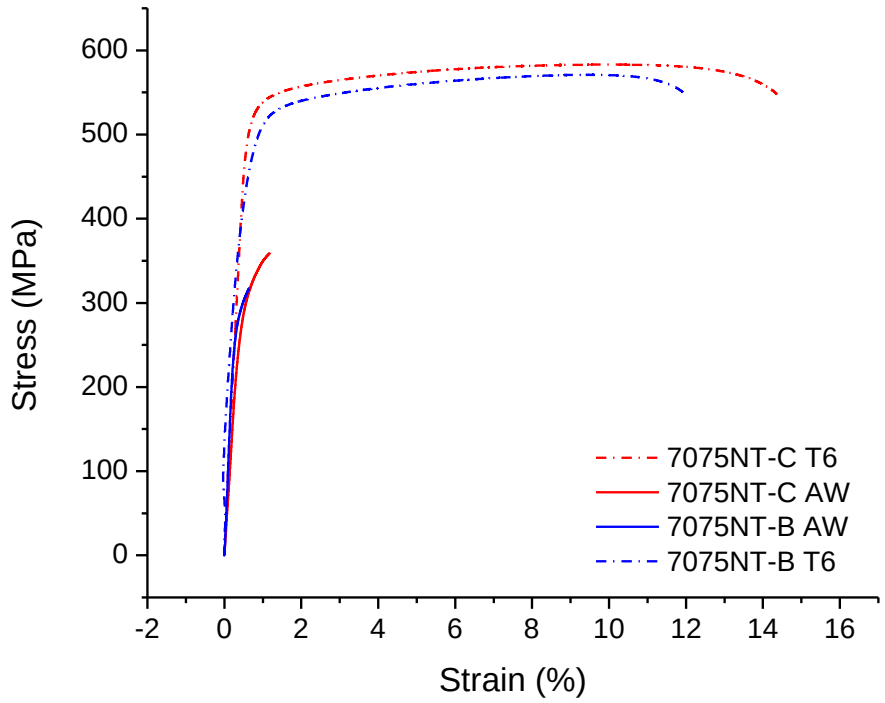

Figure 49 Typical stress-strain curves for AA7075 welded with 7075NT-C and 7075NT-B

After being subjected to a PWHT, both the TiC and TiB_2 containing specimens showed a significant increase in strength and ductility. Welds performed with 7075NT-B as filler metal typically showed an elongation of 11.9 % at fracture and an ultimate tensile strength of 571 MPa. The yield strength was recorded at 501 MPa. With the use of 7075NT-C, the typical sample fractured at 14.4 % elongation while reaching an ultimate tensile strength of 583 MPa. The sample further showed a yield strength of 530 MPa. Considering the reference yield strength, ultimate tensile strength, and elongation values for wrought AA7075-T6 are 503 MPa, 572 MPa, and 11 % [43], respectively, both nano-treated filler metals showed an exceptional response to PWHT. Typical samples in heat-treated condition fractured outside the WM at random locations in the base metal.

4.2.3.2. AA2024

Typical stress-strain curves for AA2024 base metal welded with 2024NT-B and 2024NT-C are shown in Figure 50. Similarly, the as-welded tensile properties of AA7075NT-C, the WM containing AA2024NT-C showed limited ductility in as-welded condition. A typical sample fractured at an elongation of 2.5 % and exhibited an ultimate tensile strength of 336 MPa. A yield strength of 255 MPa was recorded. By restoring the microstructure of the alloy using a PWHT, the joint containing 2024NT-C showed a significant increase in mechanical performance. A typical heat-treated specimen showed an ultimate tensile strength of 464 MPa and fractured at 16.4 % elongation. The sample's yield strength recovered to 288 MPa. Comparing these values to the ultimate tensile strength, yield strength, and elongation of wrought AA2024-T4, which are 469 MPa, 324 MPa, and 20 %, respectively, the joint showed a recovery of 99% in ultimate tensile strength, 89 % in yield strength and 82 % in elongation.

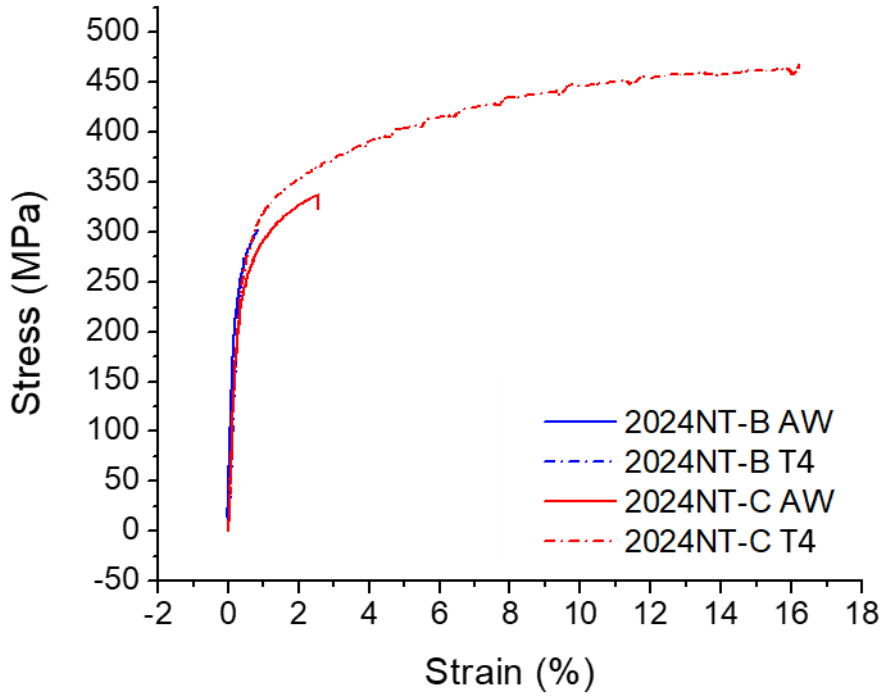

Figure 50 Typical stress-strain curves for AA2024 welded with 2024NT-C and 2024NT-B

As for joints containing 2024NT-B, no conclusive tensile data was obtained. The typical as welded and heat-treated samples fractured at 0.5 % and 1 %. It was found that the use of 2024NT-B resulted in significantly more porosity within the WM when compared to the WM containing 2024NT-C. Figure 51 illustrates this finding.

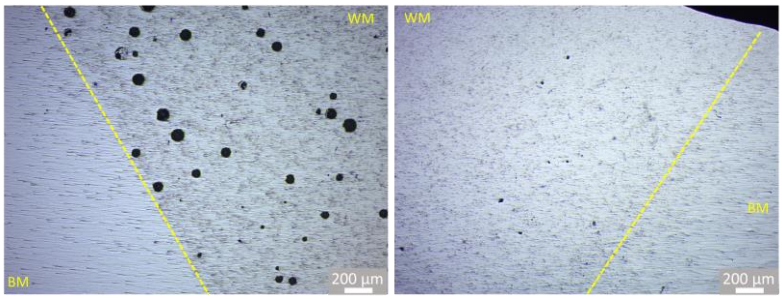

Figure 51 Weld cross-section of AA2024 base metal welded with 2024NT-B (left) and 2024NT-C (right)

While it is unclear what lead to this drastic discrepancy in porosity generation, inconsistencies in the fabrication of the filler metals regarding degreasing of raw materials and mold and argon protection of the liquid metal may have caused hydrogen absorption by the decomposition of organic residues or moisture in the ambient air.

4.2.3.3. AA6061

The study on tensile properties of AA6061 with various filler metals showed the most consistent results. It was found, in accordance with the hardness profiles, that all typical samples tested in as-welded condition fractured within the welds HAZ, where the lowest hardness was recorded.

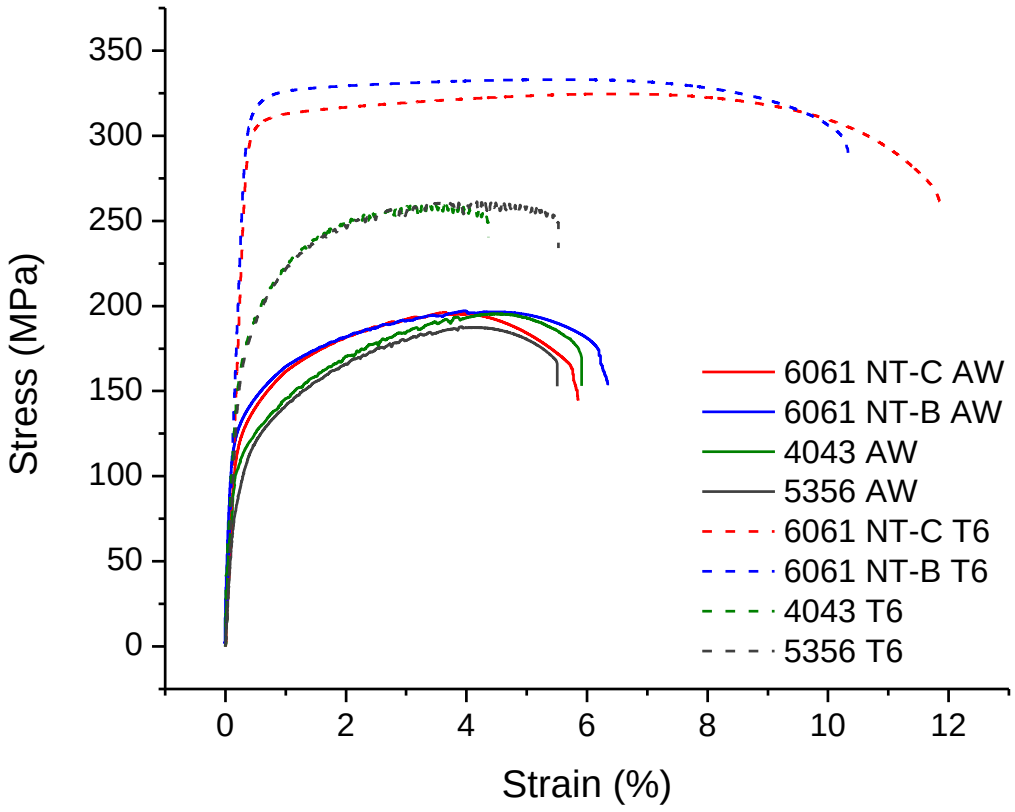

Figure 52 Typical stress-strain curves for AA6061 welded with various filler metals

The ultimate tensile strength of the as-welded samples ranged between 186 – 194 MPa, which is in good agreement with the literature [132]. However, at 132.75 MPa and 136.02 MPa for 6061NT-C and 6061NT-B, respectively, the nano-treated welds showed slightly higher yield strengths than ER4043 and ER5356 with 119 MPa and 117 MPa. In PWHT condition, the hardness profile of the welded joints again indicated the expected location of the fracture and approximate tensile strength. With the dilution of strengthening elements in the WM in welds performed with ER5356 and ER4043, the WM strength did not fully recover. Typical tensile bars, therefore, fractured within the WM at 259 MPa and 260 MPa for ER5356 and ER4043, respectively. With 5.5 %, the elongation at fracture was higher for ER5356 than for ER4043, which exhibited 4.4 %. Both filler metals showed an identical yield strength of 185 MPa.

As observed in the 2000 and 7000 series, welds performed with similar nano-treated filler showed an unprecedented response to PWHT. A typical specimen welded with 6061NT-B showed an ultimate tensile strength of 332 MPa with an elongation at break of 10.4 %, while the typical specimen containing 6061NT-C fractured at 11.9 % and exhibited an ultimate tensile strength of 324MPa. A yield strength of 317 MPa and 307 MPa was recorded for 6061NT-B and 6061NT-C. Comparing these values to the ultimate tensile strength, yield strength, and elongation of wrought AA6061-T6, which are 276 MPa, 310 MPa, and 12 %, respectively, the joint showed full recovery in ultimate tensile strength and yield strength and recovered 82 % in elongation.

4.3. Discussions

Across this study, the use of nano-treated filler metals showed remarkable advantages over welds performed with similar commercial alloys, or in the case of AA6061, the widely used filler metals ER5356 and ER4043. Significant grain refinement and morphology change are observed for NT-C and NT-B filler metals across all alloys systems. Compared to welds performed, using the respective base alloy as filler metal, the grains for the nano-treated 2000 and 7000 systems are uniform in horizontal and vertical cross-sections of the weld metal and do not show signs of curved dendrites nucleating epitaxially at the liquid-solid interface of columnar grain growth. It is indicative of the high potency of 7075NT-C and 7075NT-B, regarding nucleation and growth restriction of grains. Without changes to the weld parameters that would cause a shift in solidification rate R and thermal gradient G, the morphology of the observed microstructure shifted from columnar dendritic to globular or equiaxed dendritic as shown in Figure 53

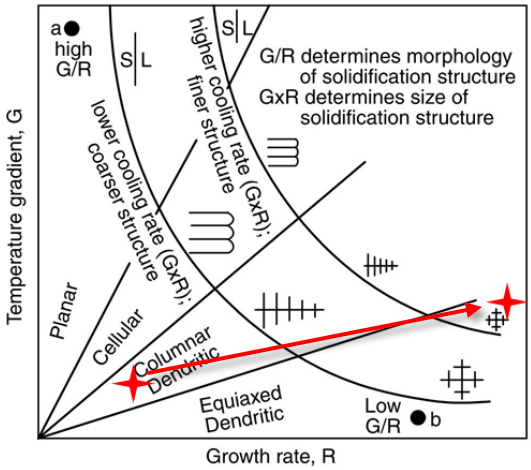

Figure 53: Growth rate, R vs. temperature gradient G schematic [25]

In the case of AA6061, welds performed with 6061NT-B filler metal have the least refinement effect, and the directional solidification was not suppressed. This phenomenon can be explained considering the intrinsic differences between AA6061, containing a total of approximately 2.8 w% added elements, and both AA7075 and AA2024, containing approximately 10 w% added elements. As stated in the literature, a higher solute content in alloys decreases the dendrite tip velocity, and both total and constitutional undercooling [133]. Since nanoparticles are believed to impose a physical restriction on the growing solidification front [109], it is fair to assume that an increase in dendrite tip velocity is likely leading to a less pronounced restriction effect caused by ≈ 0.7 v% nanoparticles. When comparing the TiC and TiB_2 containing weld metals, the carbide particles generally have a more significant grain refining than effect boride ones, for all investigated alloys. NT-C filler metal further eliminates the visible sub-grain boundaries within the primary aluminum grains, while micrographs taken from samples welded with NT-B filler metal show a typical equiaxed dendritic morphology. This observation will be further investigated and discussed in the following chapters.

The microhardness mappings yield a good first approximation of the tensile strength and fracture location of the tested specimen. Generally, the low nanoparticle content in the filler

metal does not influence the base metals HAZ. This deterioration process is governed by solid-state diffusion, enabled by the resultant high temperatures adjacent to WM. It was shown for 6000 and 7000 series alloy systems that in as-welded and PWHT conditions, the hardness of the WM was higher than that of the HAZ or base metal. It is therefore in good agreement with the observation that all representative heat-treated tensile bars failed outside of the WM in the base metal at the location of the former soft spot or beyond. The tensile strength and ductility for the PWHT welds are well within the range of AA7075, AA2024, and AA6061's wrought mechanical properties [43] and display the welding joints supreme response to heat treatment when welded with similar, nano-treated filler metal. This advantage was clearly illustrated by the 6000 series tensile data comparing nano-treated filler metal with commercial ER5356 and ER4043, which reached a UTS of 259MPa and 260 MPa in PWHT condition, respectively. With 5.5%, the elongation at fracture was higher for ER5356 than for ER4043, which exhibited 4.4%. Both alloys remained far below the recorded values of 6061NT-B and 6061NT-C, which recovered to wrought yield and tensile strength levels and exhibited a supreme ductility. When considering the Hobart filler metal chart found in Attachment B, more limitations regarding the use of commercial filler metals become apparent. AA6061 welded with ER5356 is generally not recommended for high-temperature applications and PWHT in general due to the formation of Mg_2Si precipitations and show reduced corrosion resistance.

In contrast, joints welded with ER4043 are categorized with limited strength, ductility, toughness, and color matching during anodizing. These limitations are introduced with the changed chemistry within the weld metal and are intrinsically not observed with similar filler metal. However, further research is needed to investigate the eventual effects of incorporated TiB_2 and TiC in the weld metal on other material properties.

In the case of the as-welded tensile bars, the microhardness profile was only indicative of the 6000 series specimens' fracture locations. This trend was not observed in as-welded 2000 and

7000 series samples, which broke within the WM or at the fusion boundary. Due to micro segregations, owed to a high amount of alloying elements, found the microstructure of both AA7075 and AA2024, the ductility in as-cast condition, is found to be between 1 – 2 % for both alloys [99,134]. Since this morphology is directly fused onto a soft and ductile HAZ, this interface may cause discontinuities in strain upon plastic deformation. Further, imperfections caused by the welding process itself may promote this type of failure.

5 Mitigation of hot crack susceptibility by nano-treated filler material

This chapter quantifies the effect of nanoparticles on the hot crack susceptibility oh high strength aluminum alloys. The Holdcroft test presented in Chapter 2 was chosen due to the ease of manufacturing, its relatively quantitative nature, and the ability to conduct testing on the existing welding setup. To yield a reference crack length, the Houldcroft samples were welded with their respective base material used as filler metal (e.g., AA7075 Houldcroft sample welded with AA7075 filler metal). Subsequently, the Houldcroft specimens were welded with their respective nano-treated filler metals containing TiC and TiB_2. Since the mappings in Figure 16 indicate a reduction in hot crack susceptibility for the Al-5.6Zn-2.5Mg and Al-1Mg-0.7Si system when diluted with Al-5Mg filler metal, AA7075 and AA6061 specimens were additionally tested with ER5356, 5356NT-B, and 5356NT-C filler metal.

5.1. Methods

5.1.1. Fabrication of Houldcroft specimen and hot crack susceptibility testing

To evaluate the filler material's influence on their respective alloy systems' hot crack susceptibility, Houldcroft specimens were fabricated [71]. As suggested in the literature, the original specimen was modified. Following the geometry and dimensions of the slotted region, a "lead-in" section combined with a slot to improve the test's repeatability and accuracy was added (Figure 54) [61,65,135]. AA7075, AA2024, and AA6061 samples were cut from 1.59 mm thick sheet metal (McMaster, Carr) using wire EDM.

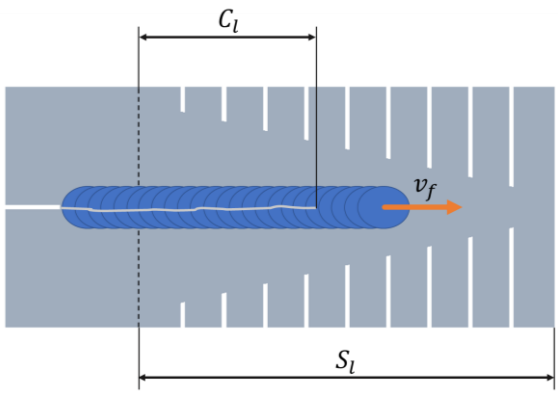

Figure 54: Modified Houldcroft sample used in this study

Before testing, samples, backing plate, and filler rod were cleaned with Acetone. The test sample was placed on the slotted backing plate shown in Figure 54and left unrestrained for testing. The welds were performed using a size 5 ceramic cup, 2.4 mm 2% lanthanated tungsten electrode, an electrode gap of 2 mm, resulting in a welding voltage of 14.5 – 15.5 Volts. The power source's parameters were set to AC TiG, 200 Hz AC frequency, 70% balance, and 25 cfh Argon flow rate. The welding tractor was set to a forward speed of 200 $\frac{mm}{min}$, while the current was set to 110 A and 120 A for AA7075 and AA6061 samples, respectively. For AA2024, an array of different current and forward speed combinations was explored.

5.1.2. Characterization

Weck's Reagent was used as a penetrant die to allow for more accurate identification of the crack tip, and the crack length was measured using a caliper.

5.2. Results

5.2.1. Houldcroft test

5.2.1.1. AA7075

Figure 55 shows the plotted results of the hot crack study conducted for the 7000 system using the Houldcroft test. Comparing the crack lengths of experiments conducted using nano-treated 7075NT-C and 7075NT-C with the reference crack length for commercial AA7075, a significant decrease is observed. While the latter causes centerline solidification cracking of 49.7 ± 3.6 %, the use of 7075NT-B decreases this centerline crack by approximately 25 % resulting in a 25.1 ± 6.0 % crack susceptibility. For experiments employing 7075NT-C as filler metal, the crack susceptibility of the pure reference composition is further decreased by 33 %, yielding an absolute crack susceptibility of 17.0 ± 3.3 %.

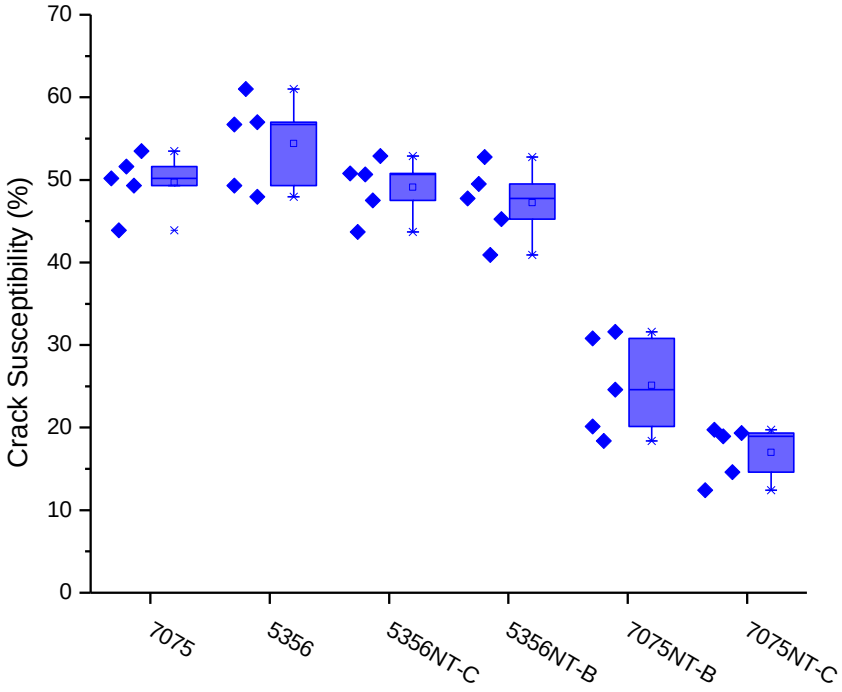

Figure 55 Hot crack susceptibility of the 7000 system

The employment of 5356NT-C and 5356NT-B does not significantly change the crack susceptibility, compared to reference experiments using ER5356 or AA7075 as filler metal. While ER5356 further increases the crack susceptibility compared to AA7075 to 54.4 ± 5.6 %, the use of nano-treated 5356NT-C and 5356NT-B slightly decreases the index to 49.1 ± 3.6 % and 47.2 ± 4.5 %, respectively. It is noted that in contrast to the solidification cracks observed with the use of 7000 series filler metal, ER5356 and its nano-treated counterparts all caused liquation cracks in the Houldcroft specimen.

5.2.1.2. AA2024

The evaluation of crack sensitivity of the 2000 series system proved difficult using the Houldcroft test. First, similar welding currents and forward speeds were explored, gauging the total crack length for an AA2024 Houldcroft sample using AA2024 filler metal. However, the sample showed no signs of hot cracking. A parametric study was therefore conducted, pursuing a maximum crack length for pure AA2024. The explored welding parameters and the resulting crack lengths can be found in Table 3. The parameter combinations were iteratively chosen to yield a consistent weld bead width. The greyed-out area on the bottom left lead to insufficient penetration, and the area on the top right caused excessive melting of the specimen. Two different batches of AA2024 sheet metal (McMaster Carr) were used to fabricate the Houldcroft samples to rule out inconsistencies in the purchased material. However, the crack lengths generated with the AA2024 Houldcroft specimen and AA2024 filler metal did not meet a crack length necessary to conduct a significant study on the hot crack susceptibility differences of commercial and nano-treated filler metal.

Welding speed (mm/min) \ Welding current (A)	70	80	90	100	120	130
160	-	-	-			
230	-	-	-	6%		
360		-	-	-	20%	
450			-	-	-	4%
500				-	13%	-

Table 3 Welding parameters for AA2024 Houldcroft test

5.2.1.3. AA6061

Figure 56 shows the result of the Houldcroft test study conducted for AA6061 using various filler metals. It is evident that with 47.1 ± 2.9 %, the by far highest crack susceptibility was found when using commercial AA6061 as filler metal. By utilizing the commercially available ER5356 filler metal, commonly used to weld AA6061, the crack susceptibility index significantly decreases to 17.3 ± 1.6 %.

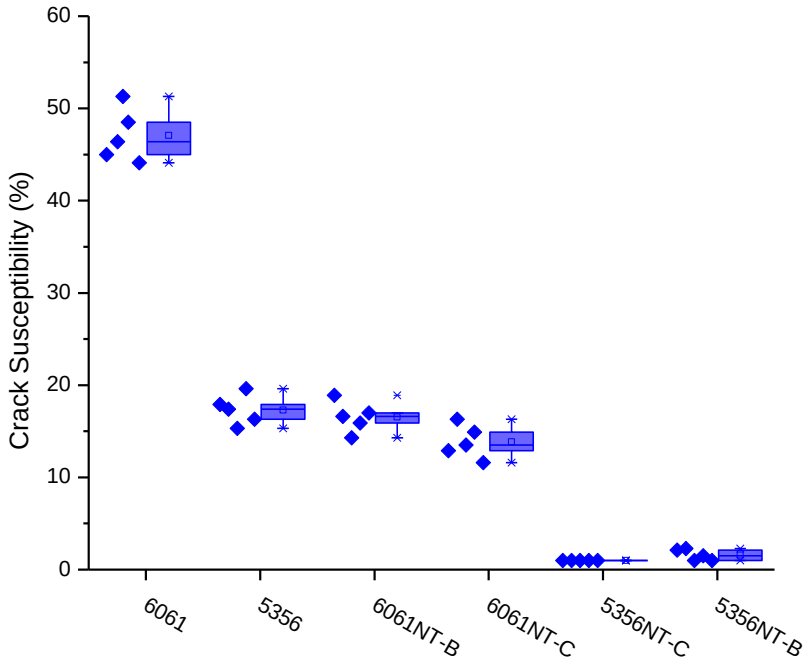

Figure 56 Hot crack susceptibility of 6000 system

It was further shown that the use of nano-treated filler metal, the susceptibility of the material system to cracking, was slightly below the commercial dissimilar filler metal. The experiments

conducted with 6061NT-B resulted in a slight decrease in crack length to yield 16.5 ± 1.7 %. The resultant index for 6061NT-C was observed as 13.8 ± 1.8 % and exhibited a further reduction compared to the filler metal containing TiB_2. The most significant decrease in crack susceptibility was observed for 5356NT-C and 5356NT-B filler metal. For 5356NT-C, no cracks entered the gauge area indicated by the dotted line in Figure 54, and therefore, no crack susceptibility was quantifiable using the present test and test parameters. By employing 5356NT-B as filler metal, a limited number of cracks entered the previously mentioned gauge area resulting in a crack susceptibility index of 1.18 ± 1.1 %.

It is noted that in this study, all observed cracks were typical centerline solidification cracks.

5.3. Discussions

In this study, it was observed that the use of TiC in similar filler metals decreases the crack susceptibility in the evaluated 7000 and 6000 series aluminum alloys more effectively than their counterparts containing TiB_2. However, the use of both NT-C and NT-B significantly decreased the respective base material's intrinsic susceptibility to solidification cracking. A correlation of these hot crack results with the microstructural observations presented in Chapter 4 is noted. 7075NT-C and 6061NT-C showed a stronger restriction of α-grain growth and a more spherical, therefore less dendritic morphology than their TiB_2 bearing counterparts. This finding is reflected in the presented hot crack study. The use of 7075NT-C further decreases the hot crack susceptibility in the 7000 series system by 8 % compared to 7075NT-B. In the 6000 series system, the advantage of 6061NT-C over 6061NT-B manifested in a 4 % difference in hot crack susceptibility. Therefore, these findings further raise the question of a fundamental difference in the working mechanisms of TiC and TiB_2 nanoparticles during solidification.

Comparing the nano-treated 6061 filler metals and ER5356, a widely applied filler metal used to weld AA6061 in industrial applications, showcases the effectiveness of nanoparticles in

mitigating a material's tendency to hot cracking. As referenced in Figure 16, ER5356 shifts the chemical composition of the WM by increasing its magnesium and decreasing its silicon content, resulting in an alloy composition that is intrinsically less prone to solidification cracking [136]. The fact that with the use of nano-treated AA6061, the WMs crack susceptibility is further improved, shows that the weldability of this new technology is at an industrially acceptable level while retaining the initial elemental ratio of AA6061 and therefore preserving its intrinsic properties regarding high-temperature applicability, corrosion resistance, and heat-treatability, as shown in Chapter 4.

In the case of welding AA6061 with 5356NT-B and 5356NT-C, both beneficial effects are combined. By shifting the alloy composition to less crack prone and the addition of refractory nanophases to further mitigate hot crack susceptibility, the Houldcroft specimen barely exhibited cracking within the measured range under the chosen test conditions.

However, using 5000 series filler metal to weld AA7075 shows less promise regarding hot crack mitigation. The large differences in liquidus and solidus temperatures of the two alloy systems cause severe liquation cracking. If using ER5356 to weld, the low alloyed AA6061 the solidus-liquidus temperature ranges are 570 ˚C – 635 ˚C and 580 ˚C – 650 ˚C, respectively [43]. Due to the marginal difference in solidus temperature, liquation cracking is not expected for this alloy combination according to liquation cracking mechanisms introduced in Chapter 2, and hot cracking is mitigated. The heavily alloyed AA7075, however, solidifies between 475 ˚C – 635 ˚C. The approximate 100 ˚C difference in solidus temperature between ER5356 and AA7075 causes the WM to freeze and contract while the PMZ is still liquated and weak. While the use of 5356NT-C and 5356NT-B further reduced the crack susceptibility for AA6061, the underlying mechanisms did not seem to overcome the fundamental difference in solidus temperature regarding AA7075 and caused liquation cracking.

6 Thermal analysis of nano-treated alloys during solidification

With the exceptional grain morphology modification, supreme mechanical properties, and suppressed hot crack susceptibility shown in the previous chapters, the question of how nanoparticles facilitate the remarkable changes to the solidification behavior of AA7075, AA2024, and AA6061 remains unanswered. Further, the fact that TiC seems to outperform by means of grain control and hot crack susceptibility decrease requires further investigation. This chapter utilizes Thermal Analysis (TA) and subsequent microstructural analysis to shed light on these matters. Casting experiments were conducted to determine the effect of nanoparticle addition on the alloy systems' Grain Coherency Points (GCP) using the two-thermocouple approach established in the literature [137,138]. During solidification, this event marks the transition from free-floating growing grains to a coherent grain structure. Due to the coherency, the semisolid melt no longer behaves like a slurry mush and builds up strength to resist thermal and solidification shrinkage. Therefore, in hot crack theory, this event is commonly correlated to the onset of a material's Brittle Temperature Range (BTR) where hot cracking may occur [139–141]. The cooling curves, the cooling curve derivatives, and the solid fraction vs. temperature curves recorded were used to interpret the different stages of solidification between liquidus and solidus temperature of commercial and nano-treated alloys. This study was complemented by employing Differential Scanning Calorimetry (DSC) to obtain more detailed insights into the materials latent heat release and thus phase changes. Microscale samples of the nano-treated and commercial aluminum alloys were heated above their respective liquidus temperatures and cooled at a consistent and constant cooling rate below their respective solidus temperatures. The recorded heat flow out of the sample is directly related to latent heat released due to phase transformation. The more controlled environment and data acquisition gave better insights into the intensity and speed of the nucleating and growing aluminum α- grains.

6.1. Methods

6.1.1. Thermal analysis

The solidification cooling curves and heat flow through the melt of the aluminum alloys was investigated using the two-thermocouple setup. The setup consisted of a stainless steel cup (0.5 mm wall thickness) placed on a 200 mm x 200 mm x 25.4 mm steel plate, a frame that fixed a thermocouple at the center of the cup and a second thermocouple at a 1 mm distance from the cup's wall and a DAQ recording the thermocouple readings at a rate of 4 Hz. A schematic of this setup is shown in Figure 57. The height of the thermocouples was adjusted to be in the center of the melt. Samples of 320 g in weight were molten in a graphite crucible under argon protection (8 cfh flow rate).

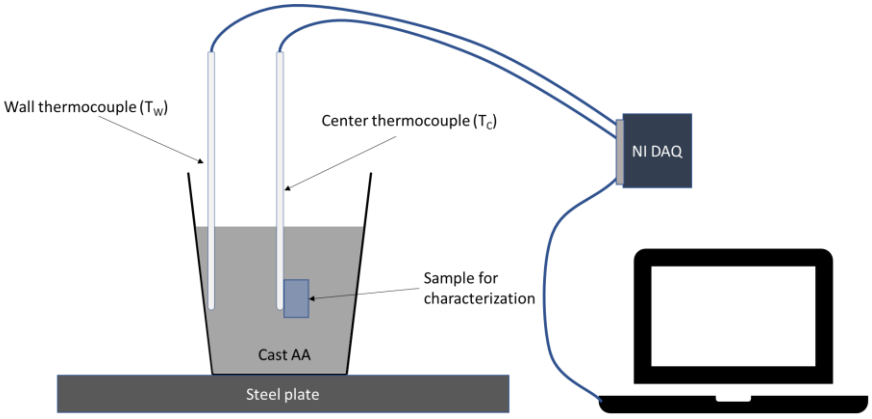

Figure 57 Casting setup used for thermal analysis

Upon melting, the sample was mechanically stirred at 400 RPM and further heated until reaching 750 °C. The samples were then cast into the boron nitride coated stainless steel cup. After each experiment, the steel base plate was cooled to room temperature to guarantee consistent conditions.

The recorded cooling curves were processed using OriginPro (OriginLab Corporation) to derive the difference of wall (T_w), and center thermocouple (T_w) defined as deltaT [142], compute the first derivative of the cooling curves and subsequently integrate the first derivative over a Newtonian baseline to obtain the solid fraction vs. temperature [143–145]

6.1.1. DSC analysis

Reference samples of commercial AA7075, AA2024, and AA6061 (McMaster Carr), as well as their respective nano-treated alloys containing TiC or TiB_2 nanoparticles, were investigated using Differential Scanning Calorimetry (DSC) (TA Instruments, Q600). The weight of the tested samples was 40±0.3 mg, and the heat flow was normalized for weight. Samples of the 7075, 2024 and 6061 aluminum alloy system were heated to 655.00 °C, 655.00 °C and 670.00 °C, respectively at a rate of 100 $\frac{^{\circ}C}{min}$, held isothermally for 5 minutes and cooled at a rate of 20 $\frac{^{\circ}C}{min}$. The recorded heat flux curves were processed using OriginPro (OriginLab Corporation) to derive the solid fraction vs. temperature using the application of peak partial

area integration [146,147].

6.2. Results

The two thermocouple approach was utilized to measure the investigated alloys' GCPs [141]. The limited thermal transport from the center of the melt to the crucible wall in combination with the latent heat release of the growing grains causes the recorded temperatures of wall and center thermocouples to diverge in the early stages of grain growth. This trend is reversed once the free-floating grains within the semi-solid touch and form a coherent network. The coherent solid network abruptly increases the thermal conductivity across the cast sample, and the wall and center thermocouple temperatures begin to converge. This point is reflected as a minimum in the deltaT (T_w - T_c) curve. Further, the first derivatives of the recorded Tc-curves reflect the

change in temperature of the melt at any given time. It is widely used in the literature to observe and quantify the release of latent heat during solidification and gives, therefore, insight into a materials grain growth mechanics and secondary nucleation events [143,148]. By applying a Newtonian zero curve to the first derivative, the tangents of the solid-state cooling rate as well as the liquid state cooling rate are connected by a parabolic function. Since during liquid state cooling and solid-state cooling, no phase transitions are observed for aluminum alloys, the difference between baseline and first derivative curve reflects the absolute amount of heat released by grain growth or nucleation events. The integral between the first derivative and baseline is therefore widely used to reflect the evolution of solid fraction during solidification [145,149]

6.2.1. Grain coherency point

6.2.1.1. AA7075

Figure 58 shows the cooling curves of T_w, T_c, and the derived deltaT curves for AA7075, 7075NT-B, and 7075NT-C. The solidification time at which the minimum in the deltaT curves was found was correlated with the center temperature at the respective time, and the grain coherency temperature was derived.

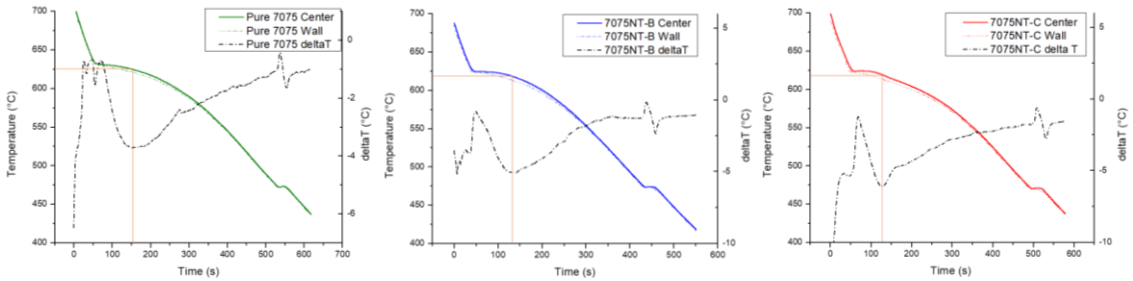

Figure 58: Cooling curves and deltaT curves for AA7075, 7075NT-B, and 7075NT-C.

While for AA7075, the GCP was recorded at 626.4 ˚C, the grain coherency of the two nano-treated alloys was observed at a lower temperature. For 7075NT-B, the GCP was lowered to 620.3 ˚C, and the coherency temperature was further lowered to 619.2 ˚C for 7075NT-C.

6.2.1.1. AA2024

The cooling curves of T_w, T_c, and the derived deltaT curves for AA2024, 2024NT-B, and 2024NT-C are presented in Figure 59.

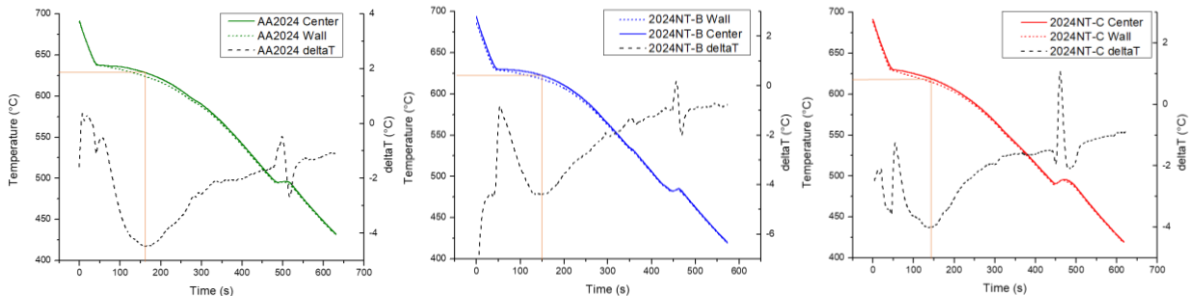

Figure 59 Cooling curves and deltaT curves for AA2024, 2024NT-B and 2024NT-C

The same procedure as for AA7075 was used to determine the temperature of grain coherency. It was again observed that the commercially pure alloy, AA2024 showed the highest temperature of coherency at 626.4 ˚C. For 2024NT-B, this temperature was decreased by 6.1 ˚C to 620.3 ˚C, while 2024NT-C further depressed the recorded reference temperature of grain coherency by 9.1 ˚C to 617.3 ˚C.

6.2.1.2. AA6061

The plots of recorded T_w and T_c cooling curves, as well as the derived deltaT curves for casting experiments of AA6061, 6061NT-B, and 6061NT-C, are shown in Figure 60.

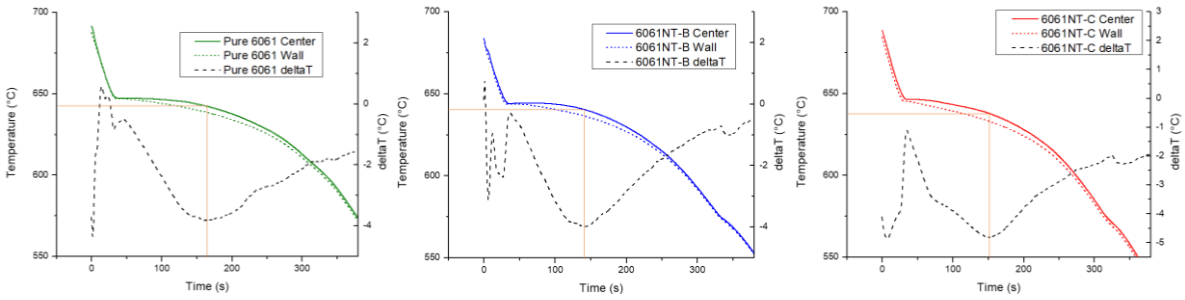

Figure 60 Cooling curves and deltaT curves for AA6061, 6061NT-B and 6061NT-C

The same procedure, as previously introduced, was used to correlate the time of grain coherency to the corresponding temperature of the center thermocouple. As for AA7075 and AA2024, the commercially pure alloy exhibited the highest temperature of grain coherency with 642.2 ˚C. In this alloy system, a different trend for the nano-treaded alloys was observed compared with the previously investigated alloys. 6061NT-C depressed the coherency temperature by 2.1 ˚C to 640.1 ˚C, while for 6061NT-B, a further reduction in the recorded coherency temperature of 4.7 to yield 637.5 ˚C was observed. This occurrence may be related to a largely the different amount alloying constituents present in AA6061 compared to the 2000 and 7000 alloys, as well as the choice of alloying elements. This phenomenon will be further discussed in the following.

6.2.2. Latent heat release and solid fraction evolution during solidification

To give a more detailed insight into phase transitions and nucleation events present during solidification, the first derivative of the center thermocouple curves presented were computed. Using the Newtonian baseline method introduced earlier, the corresponding solid fraction vs. temperature curves were derived to show the materials' solid evolution throughout the solidification process.

6.2.2.1. AA7075

Figure 61 shows the recorded center thermocouple cooling curves' first derivatives of AA7075, 7075NT-B, and 7075NT-C and the subsequently derived solid fraction vs. temperature curves.

In the compiled derivative curves, a very different heat release behavior in the early stages of solidification becomes obvious. The black line representing the commercially pure alloy exhibits a gradual increase in latent heat release before reaching the maximum and hereafter, reaching a continuous decline in the cooling rate observed in non-refined alloys [142]. For 7075NT-B, this spike in latent heat release is found to be sharper, followed by a rapid decline, while for 7075NT-C, this rapid decline in heat release is even more dominant, followed by a secondary nucleation event.

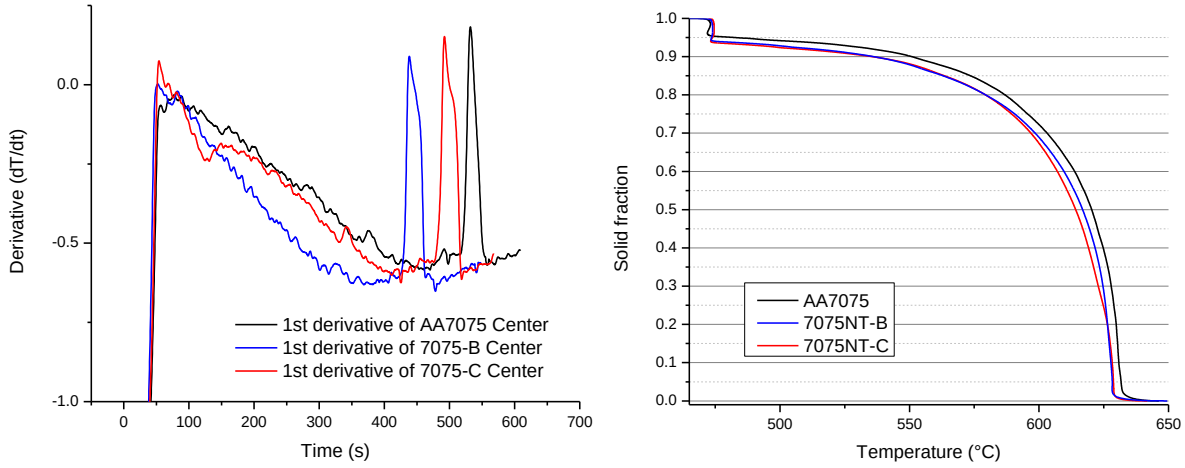

Figure 61 Derivative of cooling curves (right) and solid fraction vs. temperature curves (left) for AA7075, 7075NT-B and 7075NT-C

The implication these different types of early heat release have on the evolution of solid during the early stage of solidification are displayed on the right-hand of Figure 62. Up to approximately 15 % solid fraction NT-C and NT-B show a similarly rapid generation of solid. Next, the TiC bearing alloy exhibits a significant shift in solid evolution, indicating the onset of grain growth restriction. The solid fraction of 7075NT-B, on the other hand, continues to grow at a curve steeper than the one recorded for AA7075 indicating the behavior of a typically grain-refined alloy [150].

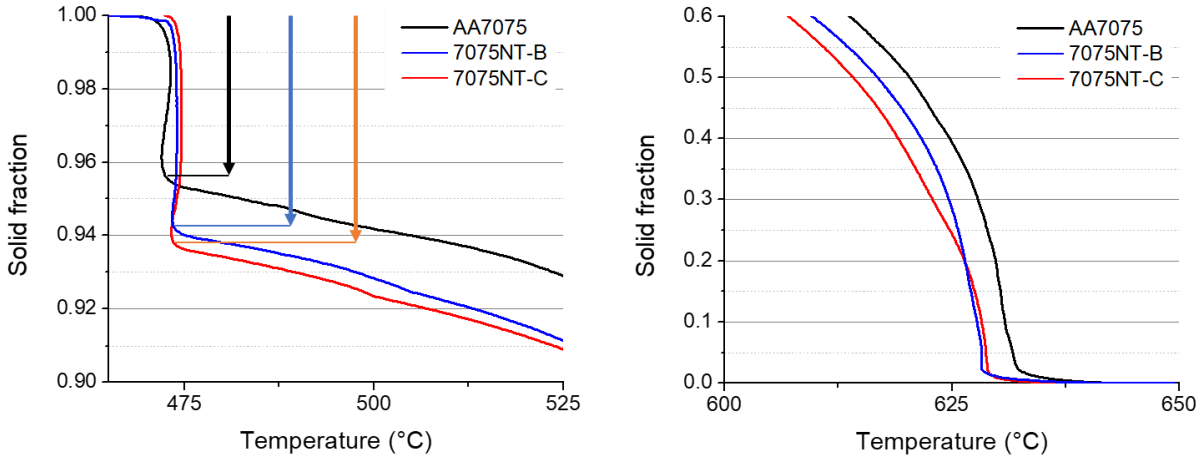

Figure 62 Enlarged segments of the late stages (left) and early stages of solidification shown in the solid fraction vs. temperature curves of AA7075, 7075NT-B and 7075NT-C

Comparing the eutectic nucleation observed between 400 – 600 s in Figure 61, firstly, the decreased overall solidification time observed for the nano-treated alloys becomes apparent. Secondly, the widths of the eutectic peaks appear to be wider than the peak observed in AA7075. The wider appearance of the eutectic nucleation event is further observed and confirmed on the left-hand of Figure 62, where the late stage of solidification in the solid fraction vs. temperature plot is highlighted. Indicated by the black, blue, and red arrow, the amount of eutectic liquid nucleating at the terminal stage of solidification was enhanced for the nano-treated alloys compared to the commercial AA7075. In detail, 7075NT-B exhibited an +29.5 % increase over AA7075, while 7075NT-C showed an +40.9 % increase

6.2.2.2. AA2024

The first derivative of the cooling curves recorded for AA2024, 2024NT-B, and 2024NT-C, as well as the corresponding solid fraction vs. temperature plots, are shown in Figure 63. After the nucleation event, similar observations as in the 7000 series' data can be made. After a sharp spike in latent heat release, 2024NT-C's plot shows a significant downward shift, which is not observed in AA2024 and 2024NT-B, followed by a subsequent distinct increase in latent heat.

In the case of 2024NT-B, after showing a spike at the nucleation event, the derivative curve approaches a slope, steeper than the commercial alloy, again, indicative of a grain refined behavior.

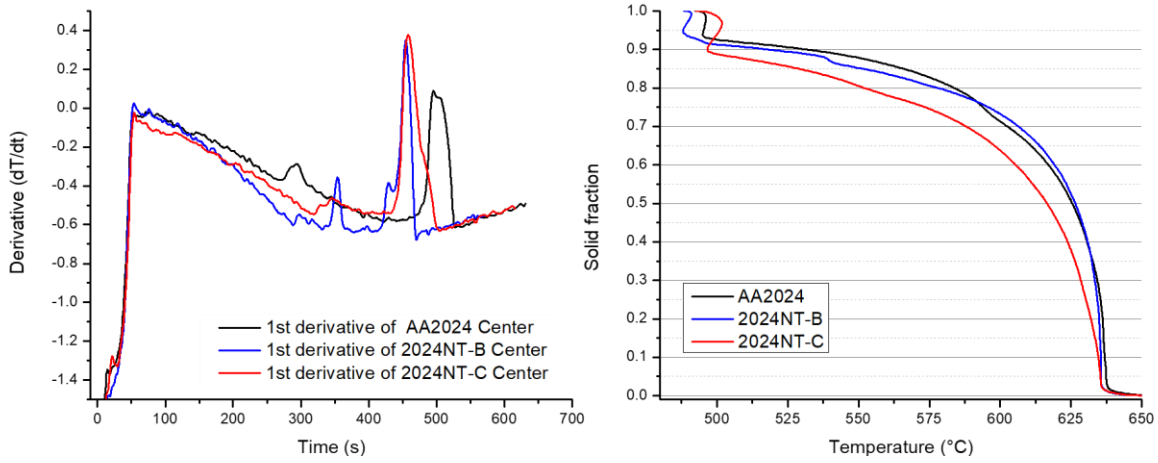

Figure 63 Derivative of cooling curves (right) and solid fraction vs. temperature curves (left) for AA2024, 2024NT-B and 2024NT-C

In Figure 64, the resultant solid fraction vs. temperature for the early stage of solidification are shown to elucidate the observations of the derivative plots. It is seen that the 2024NT-C alloy exhibits a sharp shift in solid evolution after 10 % of solid fraction towards a more restricted solid fraction increase. On the other hand, 2024NT-B showed a rapid solid increase at a steeper slope than AA2024, confirming the typical grain refined behavior. However, the complete solid fraction plot shown on the right-hand of Figure 63 highlights a gradual restriction between 50 – 70 % of solid fraction, causing 2024NT-B's solid fraction curve to shift below AA2024. This observation leads to the late stage of solidification. In the derivative curves shown in Figure 63, a lower solidification time for the nano-treated alloys is observed, while the width and height of the eutectic solidification peaks between 400 – 550 seconds appear increased.

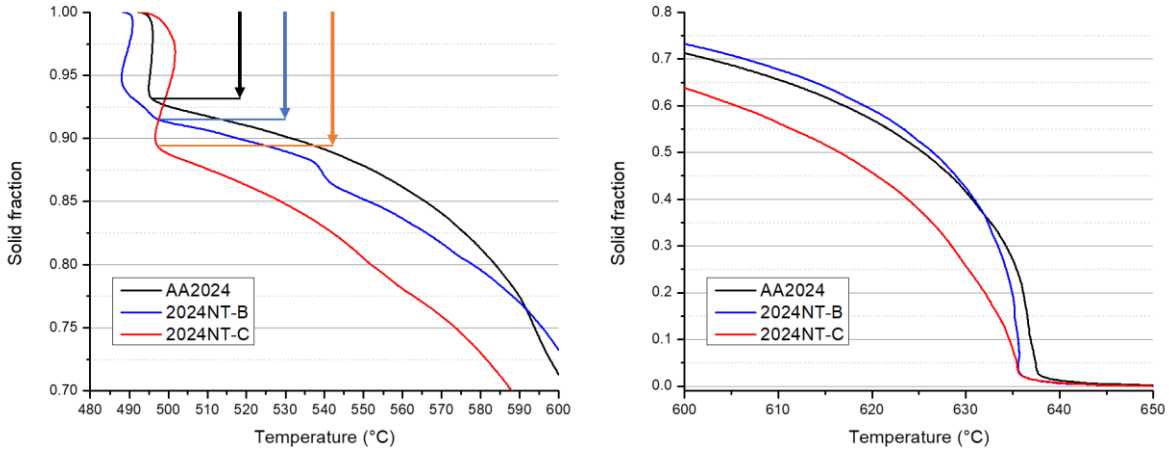

Figure 64 Enlarged segments of the late stages (left) and early stages of solidification shown in the solid fraction vs. temperature curves of AA2024, 2024NT-B and 2024NT-C

The solid fraction vs. temperature plot of the late stage of solidification in Figure 63 confirms the enhanced liquid fraction of the nano-treated alloys at the onset of eutectic nucleation. It further highlights the delayed growth restriction of 2024NT-B, causing its solid fraction curve to shift below its commercial counter part's curve at 76 %, indicating a restricted grain growth at the later stages of solidification. The relative increase of liquid fraction at the onset of eutectic nucleation over AA2024 was determined as +26.8 % for 2024NT-B and +58.2 % for 2024NT-C.

6.2.2.3. AA6061

The first derivatives of the cooling curves derived, and the corresponding solid fraction vs. temperature curves for AA6061, 6061NT-B, and 6061NT-C are shown in Figure 65. In the derivative curves shown on the left-hand, the previously observed dip for 6061NT-C, following the maximum, is once more observed. However, after its subsequent second onset of heat release, the slope approaches a similar cooling rate decrease as 6061NT-B, which did not exhibit the initial drop in latent heat release.

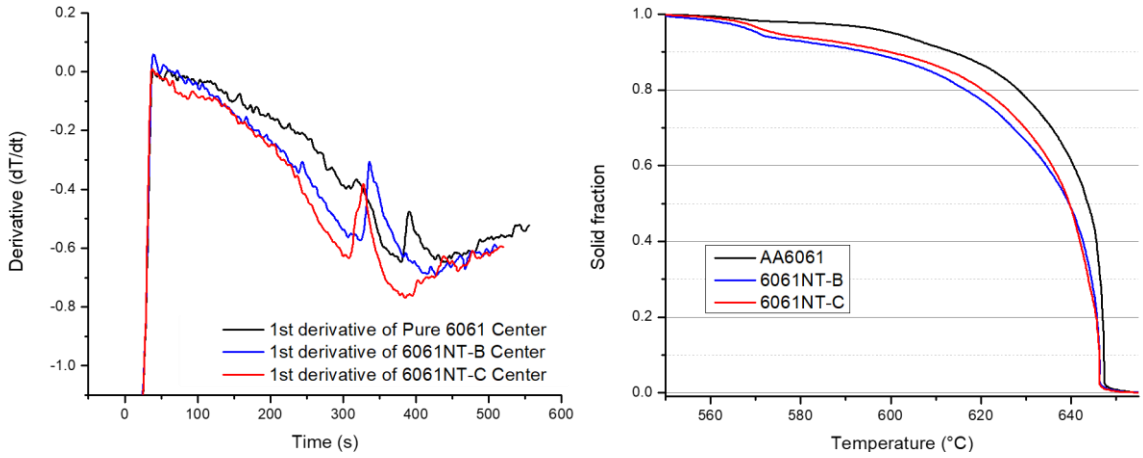

Figure 65 Derivative of cooling curves (right) and solid fraction vs. temperature curves (left) for AA6061, 6061NT-B and 6061NT-C

The right-hand of Figure 66 illustrates the solid fraction evolution of the investigated alloys in the early stages of solidification. While TiC containing alloy shows a more discrete shift of solid growth at 20 % of solid fraction, this shift is further observed in 6061NT-B more gradually. Both nano-treated alloys indicate a restricted increase in grain development compared to commercial AA6061.

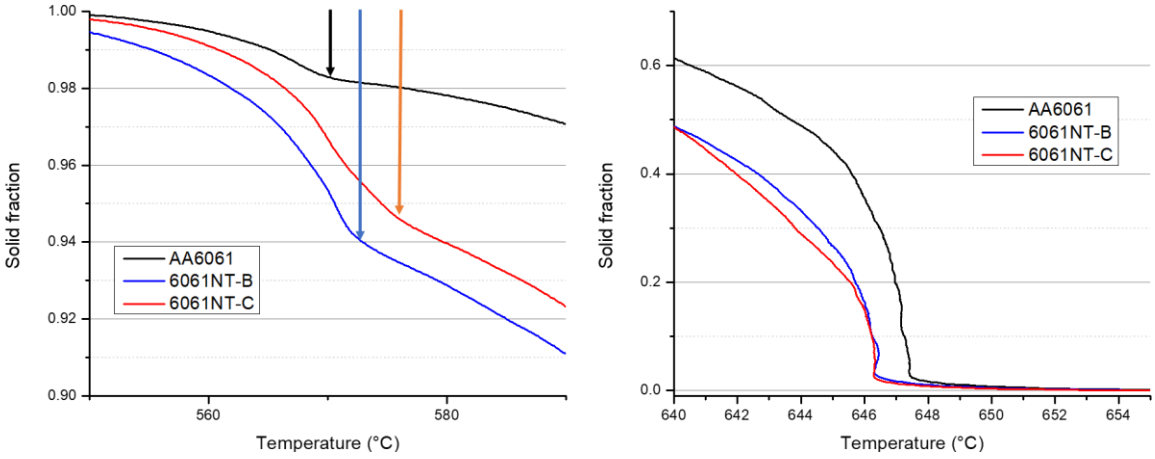

Figure 66 Enlarged segments of the late stages (left) and early stages of solidification shown in the solid fraction vs. temperature curves of AA6061, 6061NT-B and 6061NT-C

The eutectic nucleation events in the cooling curves' derivative plots in Figure 65 are observed between 300 – 450 seconds. The eutectic peaks observed for nano-treated alloys of the 6000 series demonstrate the most dramatic increase in width and height over their commercial counterpart, compared to observations made in the 2000 and 7000 series experiments. The solid fraction segment of the late stage of solidification is highlighted on the left-hand of Figure 66. It is found that the liquid fraction of 6061NT-C at the onset of eutectic nucleation showed a relative increase of +298.6 % over the commercial alloy, while the increase for 6061NT-C was recorded at +322.2 %. It is to be noted in contrast to the previously investigated alloy systems, the solid fraction curve for the TiB_2 containing alloy crossed below the TiC containing alloy at approximately 50 % solid fraction yielding a higher amount of liquid at the terminal stage of solidification.

6.2.3. Secondary phase analysis

To investigate the changes in secondary phase morphology caused by nanoparticles during solidification, a microstructural analysis was conducted. The center portions of the cast ingots were taken from the location marked in Figure 57 and prepared for SEM investigation.

6.2.3.1. AA7075

The secondary phase at the center portion of the AA7075 cast sample is shown in Figure 67. The majority of these phases solidified as $Mg(Zn,Cu,Al)_x$ eutectics and minor impurity phases, such as Al_3Fe, were observed.

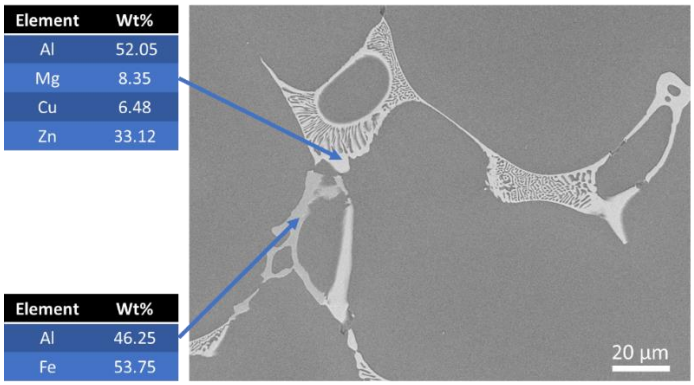

Figure 67 Secondary phases of AA7075 cast sample

The eutectic phases observed were of regular morphology showing the typical facetted and connected features found in as-cast AA7075. The grain boundaries connecting the alpha grain and secondary phase were found to be continuous and smooth.

Figure 68 shows a typical secondary phase morphology found in as-cast 7075NT-B. In contrast to the eutectic appearance of AA7075, the features within the secondary phase appear random and partially disconnected. The titanium signal observed with the Energy-dispersive X-ray spectroscopy (EDS) detector matched the outline of the overall secondary phase and showed a mostly uniform distribution within the $Mg(Zn,Cu,Al)_x$ phase, indicating dispersed TiB_2 nanoparticles.

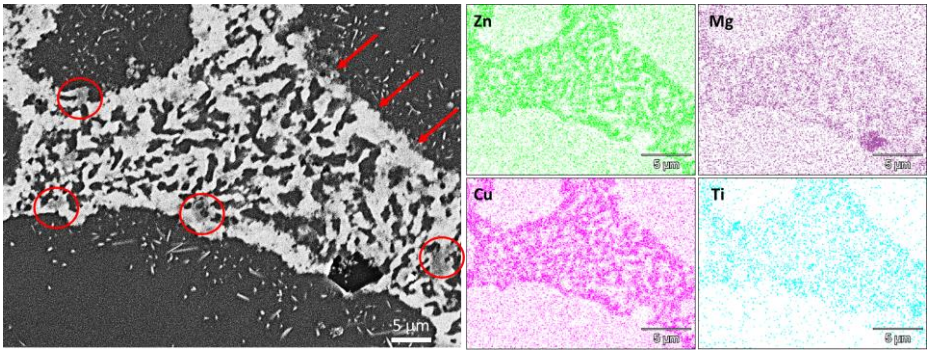

Figure 68 SEM image (left) and EDS image mappings (right) of modified $Mg(Zn,Cu,Al)_x$ secondary phase in as-cast 7075NT-B containing dispersed TiB_2 particles and microclusters

A uniformly densified signal aligning with the boundary marked by red arrows in the SEM image shows nanoparticles pushed ahead of the growing α-grain's solidification front. In contrast to the typical secondary observed in AA7075, the interface between the intermetallic phase and alpha grain appears rugged instead of smooth. Furthermore, marked by red circles, areas of dense titanium, partially shadowing the signals of zinc, magnesium, and copper, are observed and represent microscopic agglomerations of TiB_2 particles. Figure 69 shows a more prominent and clearer example of the nanoparticle clusters found throughout this investigation. Marked by the red arrow, an approximately 15 µm long artifact was observed within the alloy's secondary phase.

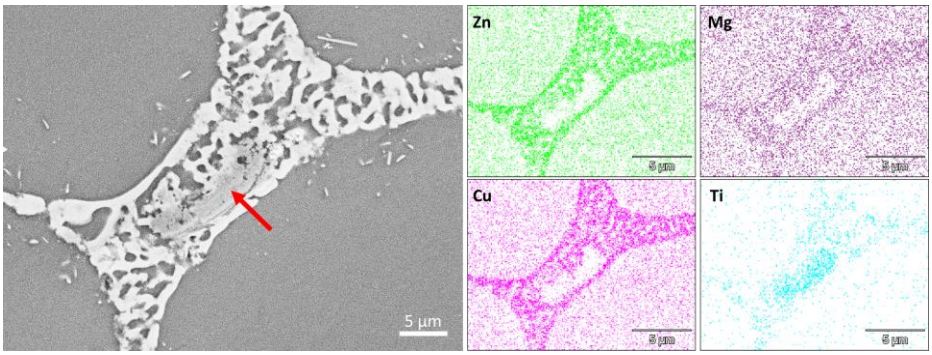

Figure 69 SEM image (left) and EDS image mappings (right) of modified $Mg(Zn,Cu,Al)_x$ secondary phase in as-cast 7075NT-B containing dispersed TiB_2 particles and macro cluster

Due to its size, the EDS mappings obtained give a more detailed chemical composition of the cluster. It is found that the largely enhanced titanium signals completely shadow the constituent elements, indicating a non-wetted particle agglomeration.

The morphology of secondary phases in 7075NT-C samples show parallels to the previously presented phases modified by TiB_2. A SEM image and EDS mappings of a typical secondary phase are shown in Figure 70.

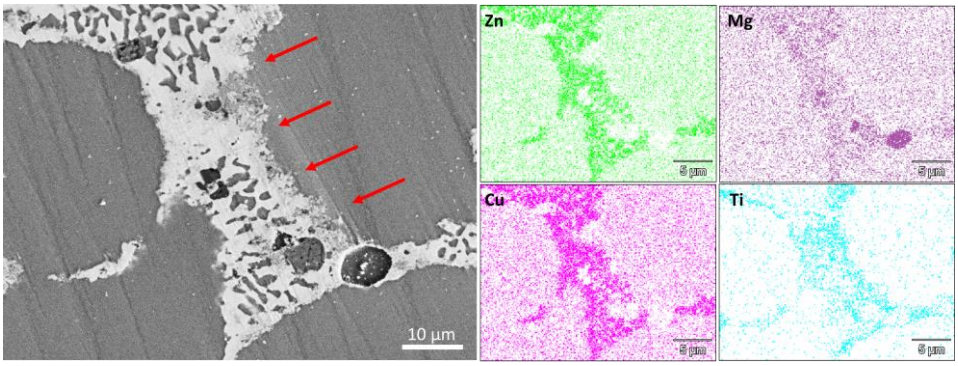

Figure 70 SEM image (left) and EDS image mappings (right) of modified $Mg(Zn,Cu,Al)_x$ secondary phase in as-cast 7075NT-C containing dispersed TiC particles and particle enrichment at its boundary

The boundary indicated by red arrows aligns with the densified titanium signal in the EDS mapping and represents particles pushed by the growing aluminum grain. The overall morphology of eutectic features is randomly oriented, while the boundaries are discontinuous and rugged. It is further noted that no densified clustering, as shown in Figure 69 for 7075NT-B, was observed in the TiC containing alloy.

6.2.3.2. AA2024

A representative SEM image of intermetallic phases observed in AA2024 castings is shown in Figure 71. In contrast to the AA7075 system, AA2024 shows a more complex solidification behavior where minor impurity elements solidify in a variety of intermetallic phases, e.g., Al2Cu, Al2CuMg, Al7Cu2Fe, Al4Cu2Mg8Si7, AlCuFeMn, and Mg2Si. [151,152].

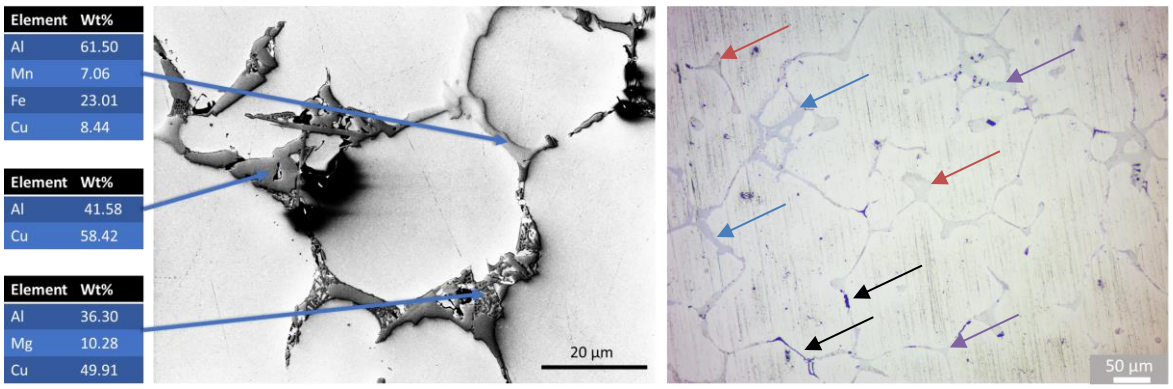

Figure 71 Constituent phase morphology in as-cast 2024. SEM image and EDS point scans (left) and optical micrograph (right)

In the optical micrograph, four distinct mayor phases in the as-cast microstructure of AA2024 were identified. While a light grey (purple arrow) and dark grey (blue arrow) phase solidified as blocky intermetallics, a brown phase (red arrow) observed was of eutectic morphology. Additionally, a slender black phase (black arrow) was observed. EDS point scans distinguished the blocky intermetallics as Al_xCu_y and $Al_xCu_yMn_zFe$ complex phases, and the eutectic phase's signal corresponded with an $Al_xCu_yMg_z$ phase. While the black sender phase was not identified, morphology and contrast in the optical micrograph concur well with Mg_xSi [151].

A typical secondary phase morphology for the investigated 2024NT-B system is shown in Figure 72.

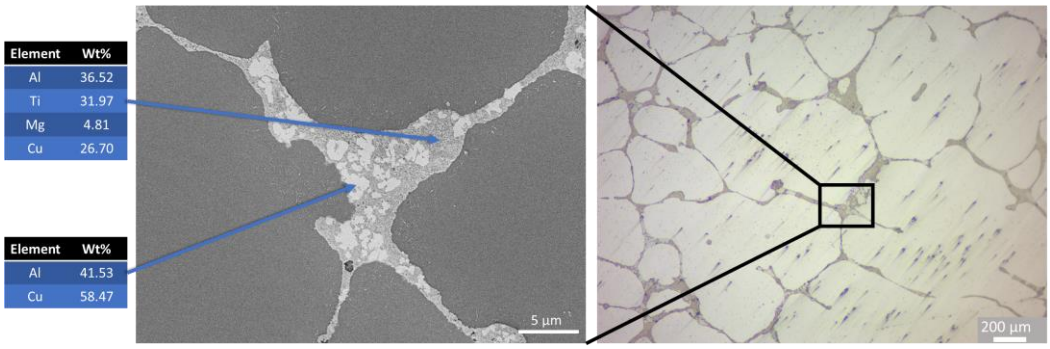

Figure 72 Constituent phase morphology in as-cast 2024NT-B. SEM image and EDS point scans (left) and optical micrograph (right)

The optical microscope image revealed that the constituent phase of the alloy containing TiB_2 nanoparticles nucleated much more uniformly than expected for the commercial counterpart without the presence of blocky segregated phases. The magnified SEM micrograph of the microstructure revealed finely dispersed intermetallic particles embedded within the intergranular eutectic. EDS point scans detected the large eutectic phase as an $Al_xCu_yMg_z$ phase containing TiB_2, whereas the light grey particle phase was identified as Al_xCu_y. It is therefore

found that the presence of nanoparticles largely impacted the morphology of the complex AA2024 microstructure.

Figure 73 is an example of a less modified eutectic phase containing a lower fraction of nanoparticles, sparsely found throughout the microstructure of the material.

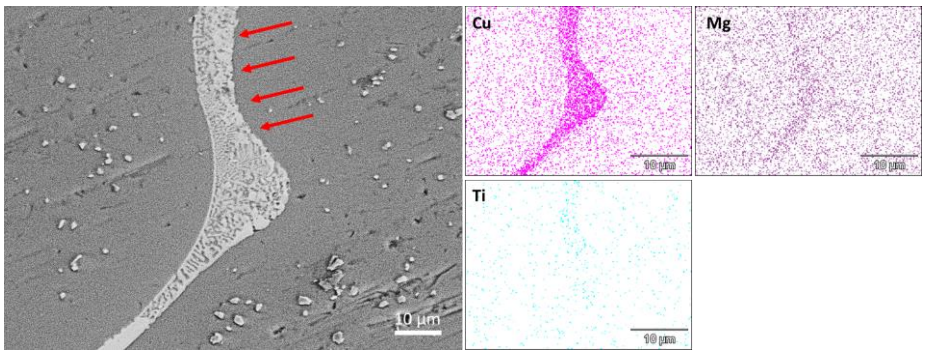

Figure 73 SEM image (left) and EDS image mappings (right) of modified Al-Cu-Mg secondary phase in as-cast 2024NT-B containing dispersed TiB_2 particles and particle enrichment at the boundary

This picture underlines the particle pushing observed in the nano-treated 7000 series micrographs. Indicated by the red arrows, a rough boundary aligned with an increased titanium signal in the EDS mapping is shown, while the lower-left boundary showing limited titanium presence in the EDS mapping is found to be smooth.

Figure 74 shows a highly dense area of TiB_2, which were mostly wetted by copper and aluminum.

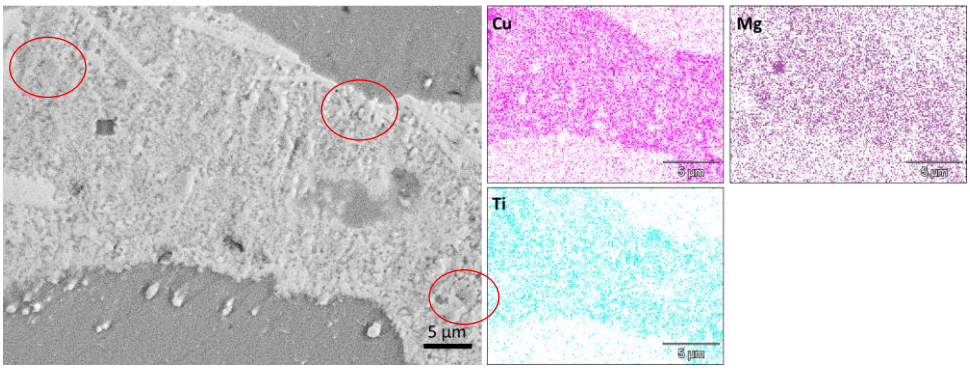

Figure 74 SEM image (left) and EDS image mappings (right) of dense TiB_2 regions infiltrated with copper and magnesium and “dry” micro-clusters observed in 2024NT-B

However, as previously observed for 7075NT-B, artifacts with intensified titanium signals were observed and are indicated by red circles, which shadowed the constituent elements' signals. These agglomerations are indicative of non-wetted particle clusters.

The overall microstructure of as-cast 2024NT-C is shown in the optical micrograph in Figure 75. Similar to the observation for 2024NT-B, the constituent phases were found to be mostly homogeneous, missing the development of large blocky segregated intermetallic phases.

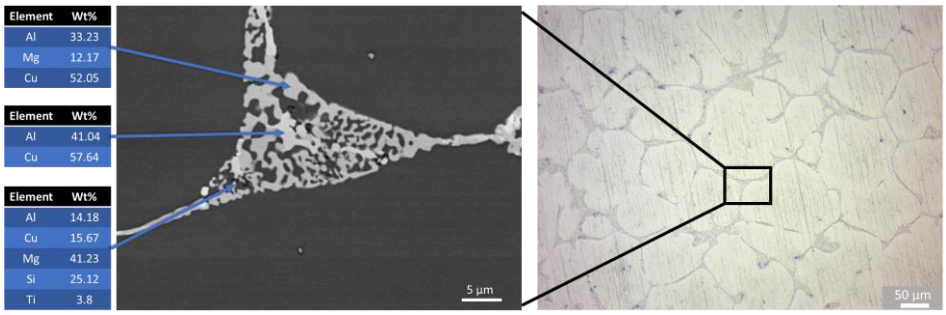

Figure 75 Constituent phase morphology in as-cast 2024NT-C. SEM image and EDS point scans (left) and optical micrograph (right)

A detailed investigation of the secondary phases is shown in the SEM image on the left-hand of Figure 75. While the morphology appeared to be an irregular broken eutectic as observed in the nano-treated 7000 series alloy, some features of the eutectic showed a slight contrast difference. EDS analysis confirmed, the eutectic that developed in 2024NT-C was a composite of Al_xCu_y and $Al_xCu_yMg_z$, while scattered black Mg_xSi phases nucleated within the network. Owed to the small size of the magnesium-silicon phase, the EDS point scan picked up surrounding aluminum, copper, and titanium signals.

A larger-scale image of 2024NT-C's secondary phases is shown in Figure 76. The scattered titanium signal observed in EDS mappings aligned with the constituent phase signals, indicating the presence of TiC within the secondary phase.

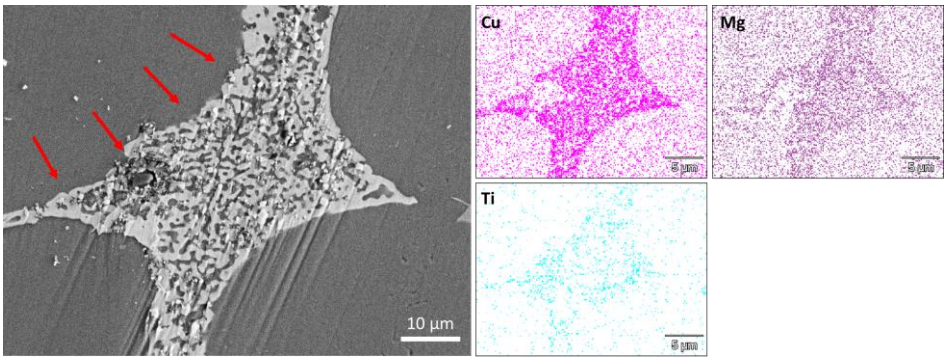

Figure 76 SEM image (left) and EDS image mappings (right) of modified Al-Cu-Mg secondary phase in as-cast 2024NT-C containing dispersed TiC particles and particle enrichment at the boundary

The eutectic's internal features appear random and broken into small discrete segments. Indicated by the red arrows, particle pushing was observed by a densified titanium signal in the EDS mapping. The pushed particles caused a rough interface to the α-grain.

6.2.3.3. AA6061

The secondary phase of the as-cast AA6061 alloy is shown in Figure 77. The eutectic structures observed are typical of an AlSiMg alloy. The constituent phases in this alloy system commonly solidify as a lamellar eutectic or a so-called "Chinese Script" structure [153]. This particular structure is representative of the solidifying secondary phase deep within the hyperbranched α-dendrite arms.

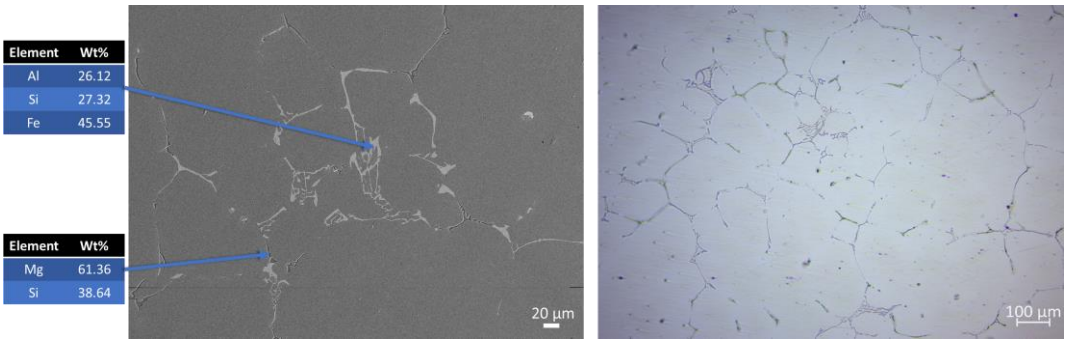

Figure 77 Constituent phase morphology in as-cast AA6061. SEM image and EDS point scans (left) and optical micrograph (right)

The phases identified using the EDS point scan were Mg_xSi and $Al_xSi_yFe_z$, while typical phases observed in this alloy are, e.g., AlFeSi, Al(FeMn)Si, Al2Cu, and Mg2Si. [154]

A typical secondary phase observed in 6061NT-B is shown in Figure 75. It was noted that the titanium signal observed in the EDS mapping aligned mainly with the joint signal of the magnesium-silicon phase indicating the presence of nanoparticle within the secondary phase.

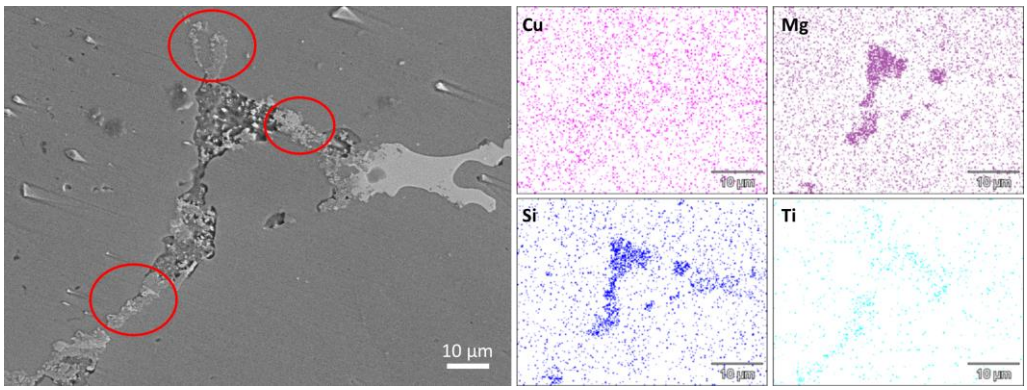

Figure 78 SEM image (left) and EDS image mappings (right) of Mg-Si secondary phase in as-cast 6061NT-B containing dispersed TiB_2 particles and clusters

As previously shown in 7000 and 2000 series micrographs, TiB_2 appears to agglomerate into clusters during solidification. The denoted artifacts in the SEM image show a titanium signal while shadowing the constituent phases, indicating non-wetted TiB_2 agglomerations.

An extreme example of TiB_2 clustering observed in this alloy system is shown in Figure 79. While the black phase observed in the SEM image corresponds with the magnesium and silicon signal observed in the EDS mappings, only a weak titanium signal overlaps with the latter.

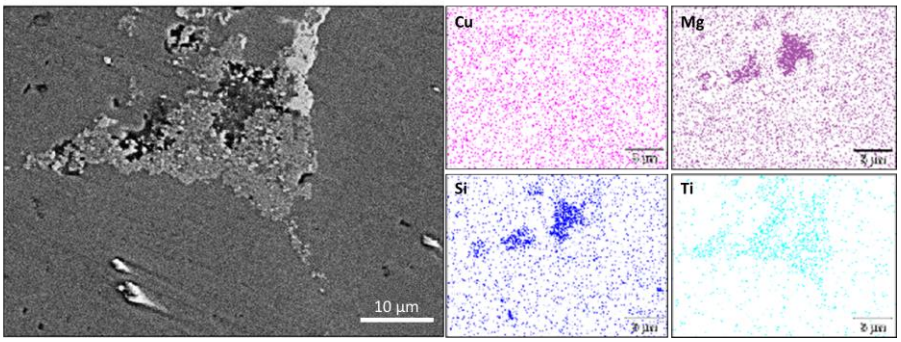

Figure 79 SEM image (left) and EDS image mappings (right) of TiB_2 cluster adjacent to Mg-Si phase in as-cast 6061NT-B

The majority of the titanium signal is densely emerging from the light grey area, adjacent to the Mg-Si signal, indicating that the secondary phase does not wet the TiB2 agglomeration.

For 6061NT-C, a typical image of a modified secondary phase is shown in Figure 80. In contrast to the TiB_2 nanoparticles, TiC was not found in magnesium-silicon phases but mainly in copper-bearing constituent phases. In the EDS mappings, it is shown that the titanium signal overlaps with the copper signal, confirming the presence of TiC particles within the secondary phase.

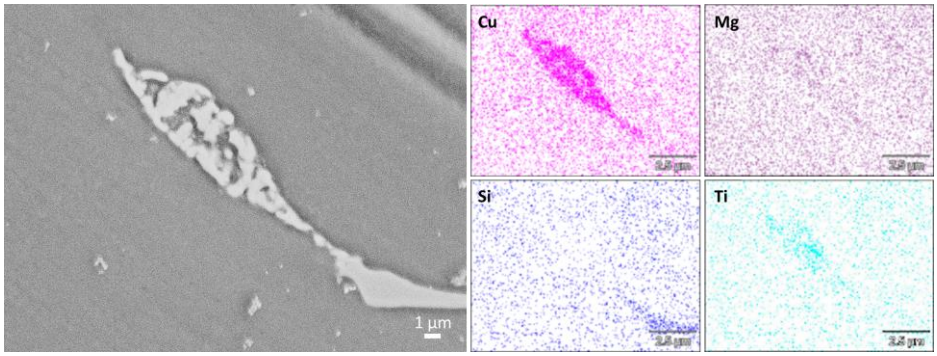

Figure 80 SEM image (left) and EDS image mappings (right) of Modified Al-Cu secondary phase in as-cast 6061NT-C containing dispersed TiC_2 particles

It is further noted that no titanium signal was found in the adjacent intermetallic phase showing a silicon signal. The morphology of the TiC-containing secondary phase showed the typical, broken morphology with rough boundaries. It is noted that no clustered artifacts, as shown for the 6061NT-B alloy, were found in 6061NT-C.

6.2.4. Image analysis of secondary phases

The previously observed increased area of the eutectic peaks shown in the cooling curve derivatives and solid fraction vs. temperature curves show a significant deviation from the commercial alloys' solidification characteristics. Since the enhancement of eutectic liquid has a major impact on an alloy's susceptibility to hot cracking, this observation was further investigated using image analysis. Representative microstructure images at consistent magnifications were taken and processes to quantify the secondary phase areas.

6.2.4.1. AA7075

Figure 81 shows secondary electron images of AA7075, 7075NT-B and 7075NT-C castings at consistent magnification. As seen in Figure 67, the typical 7000 series $Mg(Zn,Cu,Al)_x$ and Al_xFe_y constituent phases show sufficient contrast compared with the aluminum background for further image processing. By applying an FFT Bandpass Filter, the contrast was enhanced for subsequent thresholding. The area analysis of the final black/white images yielded an area percentage of 6.8 % constituent phases as a reference baseline for AA7075. For both 7075NT-B and 7075NT-C and respective increase in secondary phase, density is observed owed to the decreasing grain size.

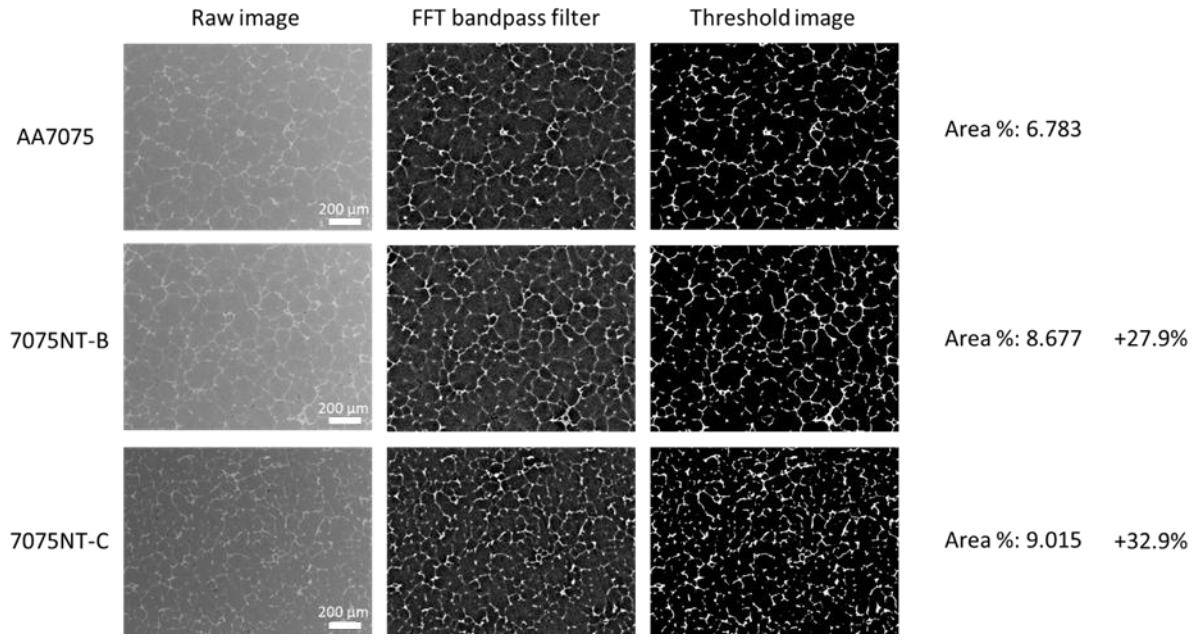

Figure 81 SEM images and derived area fraction of intermetallic phases of 7000 series castings

However, in the case of 7075NT-B, the overall fraction of secondary phases was found to be 8.7 %, marking a 27.9 % increase over the reference AA7075 sample. This percentage further increased in the alloy nano-treated with TiC nanoparticles. The processed SEM image of a 7075NT-C cross-section showed a constituent phase fraction of 9.0 %, which, compared to the reference, resulted in a relative 32.9 % area increase. Assuming that all nanoparticles incorporated in the 7075NT-C and 7075NT-B alloys were pushed by the advancing aluminum grain boundaries, the detected increase of secondary phase would have to be normalized by the fraction of nanoparticles present in the eutectic liquid.

6.2.4.2. AA2024

Secondary electron images of AA2024, 2024NT-B and 2024NT-C castings at consistent magnification are displayed in Figure 82. As shown in Figure 71, the major secondary phases observed in AA2024's microstructure show sufficient contrast for subsequent image processing. To ensure consistency, equivalent areas of secondary phase have been removed from the top left corner of 2024NT-B and 2024NT-C to account for the shadowed region found in AA2024's micrograph.

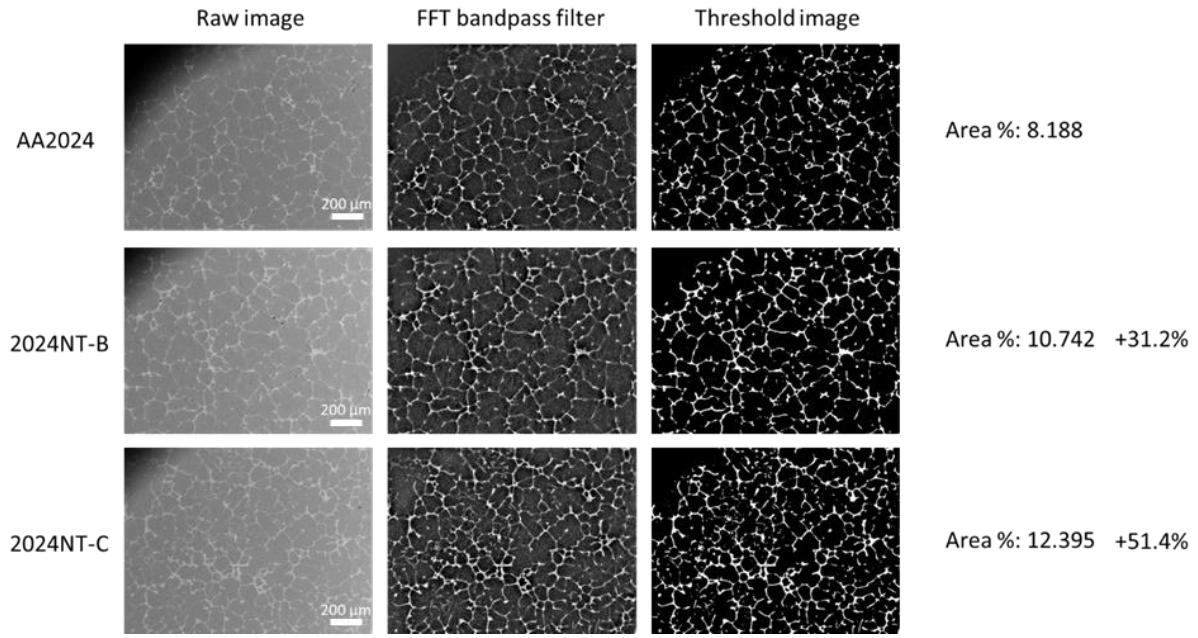

Figure 82 SEM images and derived area fraction of intermetallic phases of 2000 series castings

With 8.2 area percent of secondary phase observed, the commercial AA2024 alloy showed the lowest amount of intergranular phases in this alloy system. Due to the low magnification it was not possible to distinguish between the different types of intermetallics introduced earlier. Image analysis of 2024NT-B revealed, with 10.7 % of secondary phase area, a 31.2 % increase over the commercial alloy's recorded value. For 2024NT-C, this amount was further increased. The nano-treated alloy containing TiC showed a 51.4 % increase over AA2024's constituent phase area, at 12.4 %.

6.2.4.3. AA6061

Figure 83 shows optical microscope images at a consistent magnification of cast AA6061, 6061NT-B, and 6061NT-C cross-sections. Due to the limited visibility of silicon bearing phases shown in Figure 73, polished samples of the 6000 series were lightly etched using Weck's reagent to expose the material's secondary phases. As previously shown, the FFT bandpass filter in ImageJ was used to enhance the contrast of the image before thresholding. The two nano-treated samples showed a strong visual increase in secondary phases.

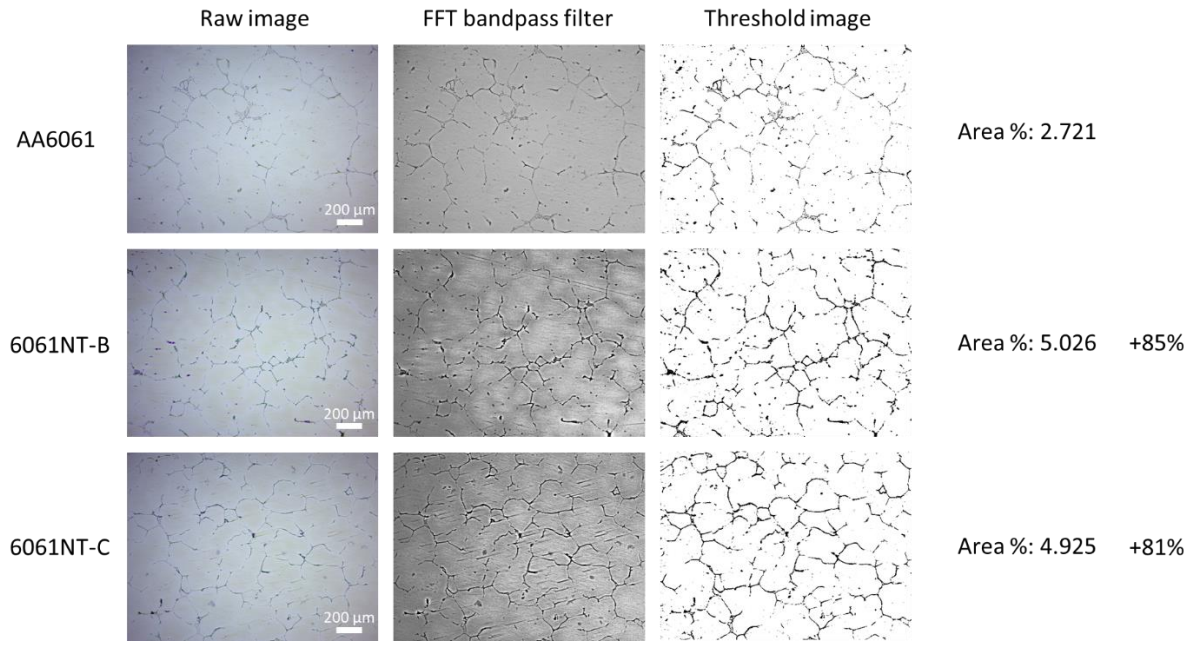

Figure 83 Optical micrographs and derived area fraction of intermetallic phases of 6000 series castings

The quantitative image analysis revealed an area fraction of 2.7 % of constituent phases found in the microstructure of AA6061. For 6061NT-B, this area fraction was found to increase by 85 %, yielding a total of 5 %. In the 6000 series, the observed area fraction of 6061NT-C was not found to be increased over 6061NT-B. The TiC containing alloy showed a relative increase over the commercial alloys secondary phase fraction of 81 % at an absolute value of 4.9 %.

6.3. Detailed heat release and phase changes during solidification

To further complement the findings made in large scale casting experiments using thermal analysis, Differential Scanning Calorimetry (DSC) was employed. The heat flux curves recorded show a higher resolution of the nucleating and growing aluminum grains and give a more detailed understanding of the restrictive effects of nanoparticles on the α-grain growth.

6.3.1.1. AA7075

Figure 84 shows the recorded heat flux curves and derived solid fraction vs. temperature curves for the 7000 series aluminum alloys investigated. A similar overall trend was observed in this study compared to the casting study conducted. The first peaks observed between 500 – 650 ˚C show a decreased peak intensity combined with a broader peak width for the tested nano-treated alloys, which represents a more gradual heat release during α-grain growth.

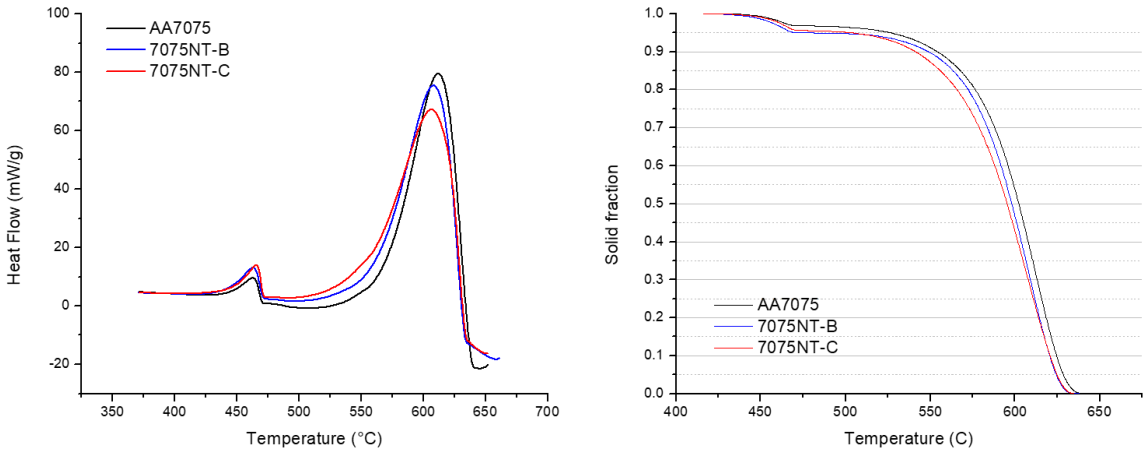

Figure 84 DSC analysis of the 7000 series system. Heat flow during solidification (left), and derived solid fractions (right)

It is further noted that the peak observed for AA7075NT-C appeared more shallow and wider than the one for 7075NT-B. In the region between 475 – 550 ˚C, it is found that while AA7075 early on approaches the heat flux baseline indicating limited phase transition and, therefore, grain growth, the nano-treated samples' heat release continues to the onset of the eutectic peak. The heat release recorded for the eutectic reaction appears broader and higher for the nano-treated samples compared to AA7075. This visual appearance is confirmed when deriving the solid fraction vs. temperature curves presented in Figure 84 right. Both alloys show an enhanced liquid fraction at the terminal stage of solidification while in this study. It is further observed that in the early stages of solidification, 7075NT-C exhibits a more restricted increase in solid

fraction at approximately 20 %. This shift is not observed for 7075NT-B until 85 % of solid fraction.

6.3.1.2. AA2024

The heat flux curves obtained in the DSC study of the investigated 2000 series alloys and their derived solid fraction curves are shown in Figure 85. It is again noted that in the heat flux curves, both nano-treated alloys exhibit a lower and wider primary peak corresponding to the materials' α-grain growth

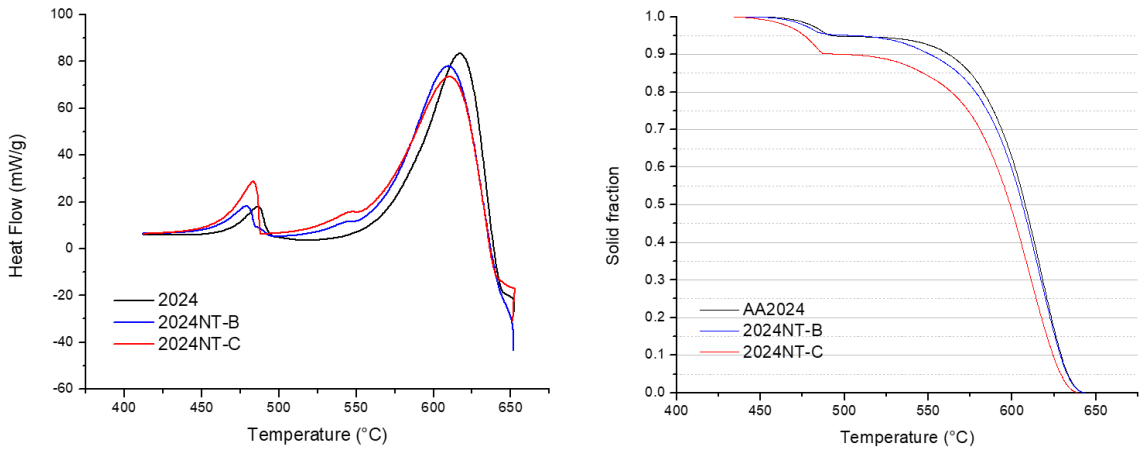

Figure 85 DSC analysis of the 2000 series system. Heat flow during solidification (left), and derived solid fractions (right)

Here the heat release for 2024NT-C is again found to be more gradual for a lower peak and a less steep slope at the declining side of the peak. The eutectic peak in this alloy system only appears to be increased for the TiC containing alloy, while 2024NT-B appears consistent with the commercial alloy. This observation is reflected in the derived solid fraction curves presented in Figure 85, right. While the onset of eutectic nucleation coincides for AA2024 and 2024NT-B, 2024NT-C shows an enhanced amount of liquid in the terminal stage of solidification. It is observed that after nucleation, the solid fraction curve of 2024NT-C strongly diverges from AA2024 towards a more restrictive grain growth. In the TiB_2 containing alloy, this phenomenon only becomes dominant at about 75 % solid fraction.

6.3.1.3. AA6061

Figure 86 shows the heat flux recorded during the DSC study conducted and the subsequently derived solid fraction vs. temperature curves for the investigated 6000 series alloys. Compared to the commercially pure AA6061, the primary peaks observed between 580 – 650 °C show a limited peak height and increased peak width for 6061NT-C and 6061NT-B, indicating a restricted grain growth for the nano-treated alloys.

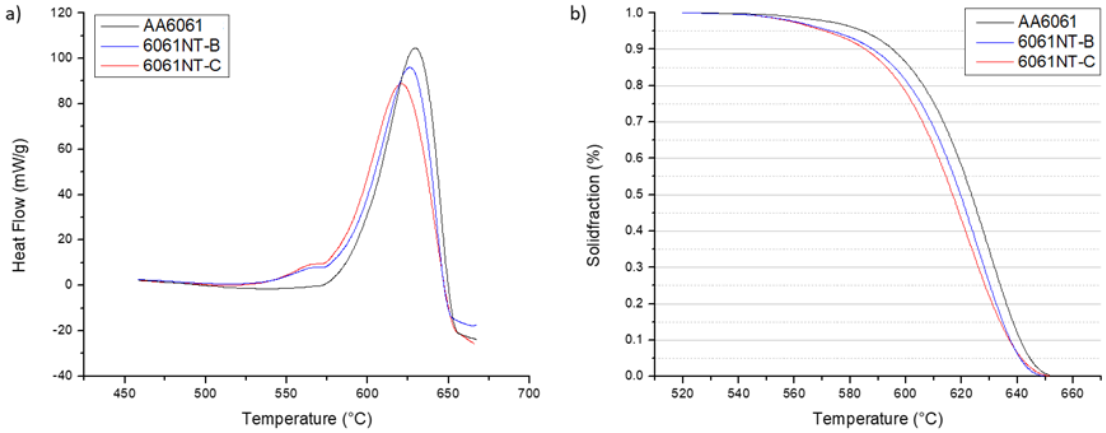

Figure 86 DSC analysis of the 6000 series system. Heat flow during solidification (left), and derived solid fractions (right)

As previously observed for the 2000 and 7000 alloys tested, 6061NT-C shows a lower and wider peak compared to 6061NT-B, indicating a higher growth restriction effect for the alloy containing TiC. At the onset of eutectic solidification, both nano-treated alloys show a largely enhanced latent heat release. This observation is further illustrated in the solid fraction vs. temperature curve presented in Figure 86, right. While both 6061NT-B and 6061NT-C show a largely enhanced liquid fraction over AA6061 at the terminal stage of solidification. In contrast to the results of the image analysis and thermal analysis, the liquid fraction of 6061NT-C appears marginally increased over 6061NT-B

6.4. Discussions

With the enhanced material properties and resistance to hot cracking presented in the previous chapters, thermal analysis and DSC analysis, paired with microstructural characterization, lead to a deeper understanding of the underlying mechanisms. The findings in this chapter show a distinctly different behavior for nano-treated and commercially pure alloys and were able to differentiate between alloys containing TiC and TiB_2 refractory nanophases. In general, the effects of nanoparticles observed can be subdivided into 3 categories; (1) The impact of nanoparticles on the growth of aluminum α- grains, (2) the modification of intermetallic phases nucleating at temperatures between liquidus and solidus temperature, and (3) the enhanced liquid fraction at the terminal stages of solidification caused by nanoparticles.

While the cooling curves and derivatives observed in casting experiments show a more restricted solidification behavior for NT-C alloys and a more grain refined solidification path for NT-B alloys, the derived solid fraction vs. temperature curves in combination with the primary peaks observed with the forced cooling rate during DSC analysis, shows a restricted solid fraction increase for both nano-treated alloys compared to their commercial counterparts with decreasing temperature. While the primary peaks are shown to be flatter and broader, indicating a more gradual heat release of the growing alpha grain, the onset of the restrictive behavior is observed at an earlier solid fraction for NT-C and at a higher solid fraction for NT-B in the casting experiments' solid fraction vs. temperature graphs. This less restrictive behavior is in good agreement with the TiB_2 micro clusters observed in the solidified NT-B alloys. While in Kennedy et al.'s study, the solidification TiC and TiB_2 microparticles within an aluminum matrix were investigated, similar observations were made [127]. The authors stated a higher wettability of TiC in molten aluminum compared to TiB_2 and observed a tendency for TiB_2 to agglomerate.

Moreover, the Hamaker constants for aluminum, TiB_2, and TiC are reported as 266 zJ[104], 256 zJ, and 238 zJ [88], respectively. Therefore, while particle pushing was observed in SEM images of both NT-B and NT-C alloys, according to Xu's theory, the lower Hamaker constant of TiC compared with TiB_2 will result in a more effective pushing effect [155]. This restrictive solidification of the alpha grain is hypothesized to be the driving force behind the lower grain coherency temperatures observed for the nano-treated alloys. In many theoretical hot cracking models, the development of a coherent and continuous grain network corresponds to the beginning of the solidus–coherency temperature range, labeled brittle temperature range (BTR). During this temperature, the semi-solid network begins to build strength to resist thermal, and solidification shrinkage and shrinkage compensation within the intergranular liquid network becomes restricted. A decrease of this brittle temperature range by decreasing the grain coherency point is therefore highly desirable to limit the likelihood of hot cracking.

The second mechanism identified was observed in the study of the 2000 series alloys' solidification behavior, since AA2024 was the only alloy involved in this study exhibiting the nucleation and growth of major intermetallic phases between its liquidus and solidus temperature[151].

While hot crack susceptibility of the nano-treated 2000 series alloys was not well determined in Chapter 5, the thermal and microstructural findings in this chapter have major implications for the material's theoretical susceptibility to hot cracking. Cross et al. found when comparing the inherent permeability of aluminum alloys 2219, 2014, and 2024 that AA2024 theoretically appears to have the best weldability [156]. The study concluded that Si, Fe, and Mn- containing constituents nucleate at temperatures between the solidus and liquidus temperature and therefore accelerate the blockage of intergranular channels far from the eutectic temperature. While this typical AA2024 microstructure is found in the reference castings, where the Al_2Cu phases, which typically nucleate at 544 ˚C [157], are found to be blocky and continuous, TiB_2

and TiC significantly change the morphological appearance of these constituents. In the case of 2024NT-B, it is found that that Al_2Cu phases nucleated within the segregations, detached from the aluminum alpha grain, and are surrounded by the pseudo-binary eutectic made up of aluminum and Al_2CuMg after solidification. This implies that instead of forming large segregations blocking the flow of intergranular liquid far above the solidus temperature, the growth of this intermetallic phase is restricted, partially forming free-flowing intermetallic particles for 2024NT-B. For 2024NT-C, a further modification of the Al_2Cu phase is observed; instead of forming dispersed particles as observed in the TiB_2 containing alloy, the early nucleation was suppressed, and Al_2CuMg and Al_2Cu formed a coherent eutectic structure at the terminal stage of solidification.

This indicates that the growth restriction effect of nanoparticles does not only apply to the aluminum alpha grain but also intermetallic compounds nucleating below the liquidus temperature. In contrast to the observations in the micrographs of the commercial AA2024 sample, the intermetallic compounds modified by nanoparticles are less likely to form blockages within the interconnected network of liquid and maintain the network's ability to backfill, therefore promoting the resistance of the material to hot cracking. It can be noted that, as seen in the morphology of the alpha grains, TiC tends to be more effective in modifying the intermetallic compounds than TiB_2.

The third mechanism observed is the increased amount of non-equilibrium eutectic phases observed at the terminal stages of solidification. The results of thermal analysis during casting, image processing of microstructure, and DSC analysis confirm the general trend of an increased liquid fraction at the final stage of solidification for nano-treated alloys. This observation strongly contradicts the prior studies on grain refined aluminum alloys, which found a decreasing amount of non-equilibrium eutectic phases with decreasing grain size [49][48]. This phenomenon is explained by constituent phases diffusing into the growing aluminum α-grains

during solidification, which is promoted by the high thermal energy. While large grains exhibit a low surface to volume ratio and a long diffusion path to the center of the grain, small grains show a higher surface to volume ratio and reduced diffusion path to the grain center. Therefore, with a reduction in grain size, an increasing amount of non-equilibrium eutectic saturates the aluminum lattice, resulting in a decreasing amount of eutectic liquid present at the solidus temperature. Therefore, while grain refinement is generally desired to reduce crack susceptibility since smaller grains were found to delay the onset of strength development in the semi-solid [47] and therefore reduce the BTR, an excessive decrease in grain size leads to a reversed trend caused by a lack of eutectic liquid to backfill the semi-solid network [24] [156], shown in Figure 12.

Therefore, the use of nanoparticles breaks this fundamental limitation of classical grain refiners by enhancing the amount of non-equilibrium eutectic liquid, despite offering a refined grain structure. Both manifestations are highly desirable to prevent hot cracking in aluminum alloys. It is hypothesized that nanoparticles pushed by the advancing grain boundaries shown in the SEM micrographs partially block the diffusion path of constituents into the grain. Moreover, with increasing solid fraction, the nanoparticle volume fraction within the residual liquid increases due to particle pushing. This increasing volume fraction is likely to block diffusion of constituents within the liquid phase, cause a homogenization of the latter, and to hinder constituents from diffusing towards the liquid-solid interface. Wang et al. proposed a diffusion-based model accurately predicting the grain size of pure aluminum with various amounts of TiCN [111]. Based on this model, by not only accounting for the restriction of aluminum atoms diffusing towards the growing aluminum grain but including the diffusion of constituents within an alloy system, a theoretical framework for this observation is feasible.

Based on the experimental results and interpretation of the findings, the solidification mechanisms observed in this study are illustrated in Figure 87. Here the red frame denotes the event of grain coherency and the turquoise areas mark the secondary phase after solidification.

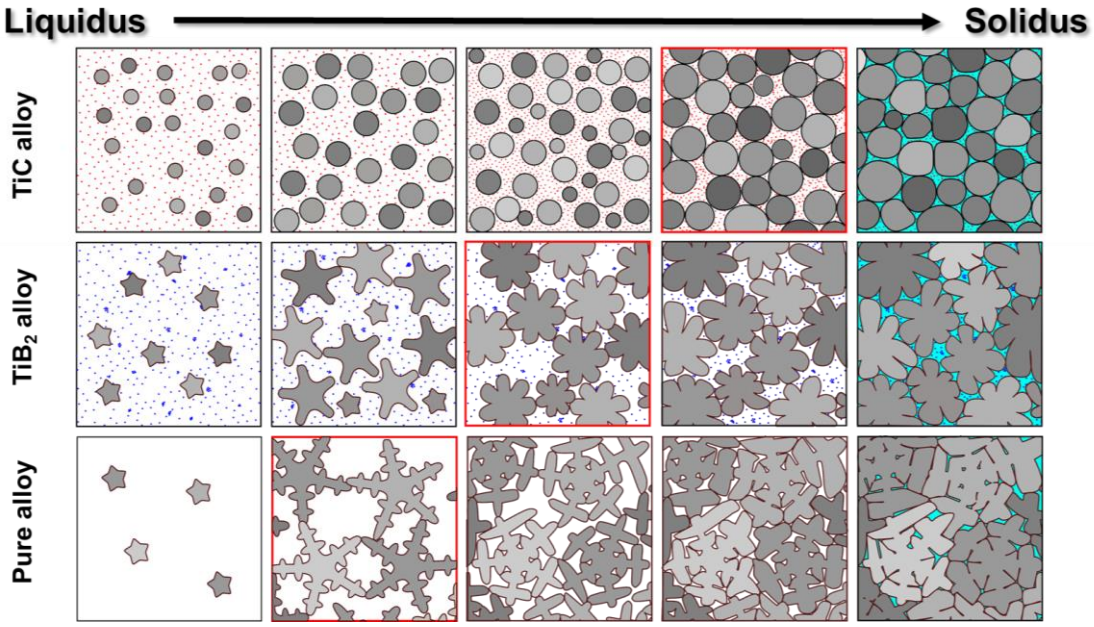

Figure 87 Schematic of the solidification process of commercially pure aluminum alloys, alloys enhanced with a low fraction of TiB_2 nanoparticles and alloys enhanced with a low fraction of TiC nanoparticles

7 Conclusions

This study is motivated by the lack of weldability of high strength aluminum alloys due to high hot crack susceptibility. Conventional methods to mitigate hot cracking showed limitations in their effectiveness or did not apply to certain alloys. It was therefore motivating to explore the unique solidification behavior of metal matrix nanocomposites in combination with Gas Tungsten Arc Welding of high strength aluminum alloys.

AA7075, AA2024, AA6061, and ER5356 alloys were infused with 0.8 v% TiC (NT-C) and TiB_2 (NT-B) nanoparticles, respectively, while the effective number of nanoparticles present within the nanocomposites was slightly lower. 7075NT-B/C and 2024NT-B/C were used as filler metal to successfully weld AA7075, and AA2024 were for the first time. In the same manner, 6061NT-B/C was successfully employed to weld AA6061, also considered unweldable without dilution of dissimilar filler metal.

The welded joints show enhanced hardness in the weld metal in combination with a highly refined grain structure. Here, TiC containing welds typically exhibit slightly higher hardness and smaller grain structure than welds containing TiB_2, while more effectively suppressing the development of a dendritic grain morphology. The weld metal further showed a supreme response to post-weld heat treatment, elevating its hardness over the hardness level of the base metal for all three alloys tested. These observations were mostly reflected in transversal tensile tests of the welded joints. The high amount of micro-segregations developing in the weld metal microstructure of joints welded with 7075NT-B/C and 2024NT-B/C likely cause limited ductility in tensile tests performed in as-welded condition, since all samples fractured in the weld metal or at the fusion boundary. In the case of 6061NT-B/C, the weld metal strength was not determined in as-welded condition since all tensile bars, including the one’s welded with commercially available filler metal, fractured at the soft spot of the heat-affected zone. By

employing a post-weld heat treatment, the tensile samples welded with both 7075NT-B and 7075NT-C reached remarkable material properties of wrought AA7075-T6, fracturing outside of the weld metal. The same trend was observed for where the shortcomings of ER5356 and ER4043 regarding a post-weld heat treatment become obvious. The samples welded with commercial filler metal showed limited recovery of strength and ductility while the samples welded with 6061NT-B and NT-C recovered to wrought AA6061-T6 with a minor reduction in ductility. In PWHT condition, AA2024 welded with 2024NT-C shows a similarly exceptionally recovery in mechanical properties. However, due to porosity present in the weld metal of 2024NT-B tensile bars fractured within the weld metal, exhibiting very limited ductility.

While the very high ultimate tensile strength and ductility of the tensile samples in heat-treated condition indirectly implied a sound microstructure free of microcracks, a Houldcroft study was employed to quantify the nano-treated filler metals effect on the respective material's hot crack susceptibility. The tests conducted for AA7075 and AA6061 showed a significant reduction in hot crack susceptibility for similar NT-B and NT-C filler metals. It was observed that filler metals containing TiC marginally reduced the crack susceptibility below the level of filler metals containing TiB_2. The use of dissimilar 5000 series metal to mitigate solidification cracking was shown unsuccessful for AA7075 due to liquation cracking issues. Using ER5356 as filler in the Houldcroft test of AA6061, however, revealed an exciting comparison, showcasing the effectiveness of this novel technology. The crack length caused by ER5356 was found to be slightly higher than those for 6061NT-B and 6061NT-C, implying that the crack reduction caused by both nano-treated filler metals is at an industrially applicable level. It was further shown that introducing nanotechnology into the commercial ER5356 filler metal can further reduce the crack susceptibility of welded AA6061 joints.

The reasons for this significant reduction in crack susceptibility were found utilizing thermal analysis, DSC analysis, and microstructure characterization. The combination of these

approaches revealed that nanoparticles cause a threefold mechanism enhancing an aluminum alloys resistance to hot cracking. Firstly, nanoparticles effectively controlled the growth and morphology of the alloys' aluminum α-grains. The study further displayed a restricted growth and modification of intermetallic phases nucleating between liquidus and solidus temperature, more clearly observed in the microstructure of the nano-treated 2000 series alloys. This finding brings significant implications for aluminum alloys (such as AA2024), where intermetallic impurity phases prematurely block the permeability of the liquid network and therefore lower its ability to backfill solidifying trenches. Lastly, an enhanced amount of non-eutectic liquid was shown for all nano-treated alloys when compared to their commercial counterparts. This phenomenon strongly contradicts common perceptions and mechanisms observed for conventional grain refinement and can be explained by diffusion control of constituent elements caused by nanoparticles coating the liquid-solid interface during grain growth and homogenization of the intergranular liquid. The importance of this last mechanism on the overall reduction of aluminum alloys' susceptibility to hot cracking is highlighted in the results of the studied 6000 series alloys.

In welding experiments, the directional growth morphology for 6061NT-B is not completely suppressed, while the Houldcroft test results show an exceptional reduction in crack susceptibility similar to the observation in 6061NT-C. However, both alloys show a largely increased amount of non-equilibrium eutectic liquid at the terminal stages of solidification. Therefore, instead of solely focusing on the grain morphology after solidification, the discovered effect of nanoparticles on the diffusion of constituent elements into the aluminum α-grains and the restricted increase in solid fraction during grain growth cannot be neglected when assessing how nano-treated alloys reduce crack susceptibility. However, throughout this study, it was shown that TiC particles more effectively facilitate the aforementioned changes on aluminum alloys solidification behavior, due to TiB_2's tendency to form microclusters in the liquid state and the intrinsically lower particle pushing efficiency in the Al – TiB_2 system.

In summary, this work has successfully employed the use of refractory nanophases to enable arc welding for previously unweldable aluminum alloys and uncovered the underlying mechanisms. Low volume fractions of TiB_2 and TiC nanoparticles have proven to significantly reduce the crack susceptibility of AA7075, AA2024, and AA6061. This study, therefore, paves the way for the rational design of nanoparticle enabled welding or liquid state processing of hot crack susceptible aluminum alloys and other engineering alloys.

8 Recommendations for future work

8.1. Rational design of nano-treated aluminum alloys

With a parametric study, correlating the volume percentage of nanoparticles within the solidifying material to the resultant crack susceptibility, a rational design of this technology can be achieved. By finding the lowest amount of nanoparticles to prevent major hot cracking during solidification, the fabrication cost of this approach can be minimized and therefore its attractiveness towards widespread industrial application

8.2. A theoretical model to predict solidification behavior

It was shown throughout this study that the highly alloyed nano-treated 7075 and 2024 alloys exhibited a slightly different behavior than the low alloyed nano-treated 6061 alloys. It is, therefore, of great interest to develop a theoretical framework to combine the restrictive behavior of nanoparticles on growing aluminum alpha grains and the diffusion behavior of constituent elements.

This model could further guide the rational design of various aluminum alloys by predicting specific nanoparticle volume percentages depending on the intrinsic solidification behavior of specific alloys.

8.3. Study on welding of dissimilar metals

The fusion welding of dissimilar metals such as aluminum-titanium or aluminum-steel is a longstanding fundamental and industrial challenge. It would therefore be of great interest if the findings of this study, specifically the observed growth restriction of nanoparticles on

nucleating intermetallic phases, can have a beneficial effect on such brittle Al_3Ti or Al_3Fe phases forming during the fusion welding of latter material combinations.

8.4. Advanced hot crack testing

The use of more advanced evaluation methods such as the previously introduced Varestraint test or the Gleeble welding simulator should be employed to study the differences in commercially pure, NT-B, and NT-C alloys to greater detail. With externally augmented strain, the impact of nanoparticles on the Grain Coherency Point and, therefore, Brittle Temperature Range of the investigated materials can be directly quantified. The better understanding of the crack mechanisms involved in the solidification cracking of nano-treated alloys will possibly enable an adaption of classical hot crack models and criteria to this young research field.

8.5. Application of nano-treating in additive manufacturing

High strength aluminum alloys are so far not applicable to additive manufacturing processes such as powder-based Selective Laser Melting or wire and powder-based Direct Energy Deposition, due to their intrinsic hot crack susceptibility. With the findings of this study, it is without a doubt that nano-treating of such alloys will enable a new research direction and ultimately allow their expansion to the commercial sector of additive manufacturing.

References

References

[1] Zion Market Research, Welding Products Market (SAW Wires & Fluxes, Solid Wires, Flux-cored Wires, Stick Electrodes,) Market for Building & Construction, Automobile & Transportation, Marine, Offshore and Other Applications: Global Industry Perspective, Comprehensive Analysis and Forecast, 2016 – 2022, 2017.

[2] T. Dursun, C. Soutis, Recent developments in advanced aircraft aluminium alloys, Materials & Design (1980-2015) 56 (2014) 862–871.

[3] A. Arowosola, G. Gaustad, Estimating increasing diversity and dissipative loss of critical metals in the aluminum automotive sector, Resources, Conservation and Recycling 150 (2019) 104382.

[4] W.J. Joost, Reducing Vehicle Weight and Improving U.S. Energy Efficiency Using Integrated Computational Materials Engineering, JOM 64 (2012) 1032–1038.

[5] C. Schutte, Vehicle Technology Program Annual Merit Review – Lightweight Materials, Materials Technologies, US Department of Energy (2010).

[6] C. Liu, D.O. Northwood, S.D. Bhole, Tensile fracture behavior in CO2 laser beam welds of 7075-T6 aluminum alloy, Materials & Design 25 (2004) 573–577.

[7] J.H. Martin, B.D. Yahata, J.M. Hundley, J.A. Mayer, T.A. Schaedler, T.M. Pollock, 3D printing of high-strength aluminium alloys, Nature 549 (2017) 365–369.

[8] S.C. Wu, Y.N. Hu, X.P. Song, Y.L. Xue, J.F. Peng, On the Microstructural and Mechanical Characterization of Hybrid Laser-Welded Al-Zn-Mg-Cu Alloys, J. of Materi Eng and Perform 24 (2015) 1540–1550.

[9] T. Soysal, S. Kou, Predicting effect of filler metals on solidification cracking susceptibility of 2024 Al and 6061 Al, Science and Technology of Welding and Joining 24 (2019) 559–565.

[10] Z. Qi, B. Cong, B. Qi, G. Zhao, J. Ding, Properties of wire + arc additively manufactured 2024 aluminum alloy with different solution treatment temperature, Materials Letters 230 (2018) 275–278.

[11] M. Sheikhi, F. Malek Ghaini, H. Assadi, Solidification crack initiation and propagation in pulsed laser welding of wrought heat treatable aluminium alloy, Science and Technology of Welding and Joining 19 (2013) 250–255.

[12] A.K. Vasudevan, R.D. Doherty, Aluminum Alloys--Contemporary Research and Applications: Contemporary Research and Applications, Elsevier Science, Saint Louis, 2014.

[13] P.K. Mallick, Materials, design and manufacturing for lightweight vehicles, CRC Press; Oxford Woodhead, Boca Raton, Fla., 2010.

[14] E. Ahmadi, M. Ranjkesh, E. Mansoori, M. Fattahi, R.Y. Mojallal, S. Amirkhanlou, Microstructure and mechanical properties of Al/ZrC/TiC hybrid nanocomposite filler metals of tungsten inert gas welding fabricated by accumulative roll bonding, Journal of Manufacturing Processes 26 (2017) 173–177.

[15] M.S. Bayati, H. Sharifi, M. Tayebi, T. Isfahani, Effect of Al-B 4 C nanocomposite filler manufactured by accumulative roll bonding (ARB) method on the microstructure and mechanical properties of weldings prepared by tungsten inert gas welding, Mater. Res. Express 6 (2019) 106529.

[16] M. Fattahi, M. Mohammady, N. Sajjadi, M. Honarmand, Y. Fattahi, S. Akhavan, Effect of TiC nanoparticles on the microstructure and mechanical properties of gas tungsten arc welded aluminum joints, Journal of Materials Processing Technology 217 (2015) 21–29.

[17] M. Fattahi, N. Nabhani, E. Rashidkhani, Y. Fattahi, S. Akhavan, N. Arabian, A new technique for the strengthening of aluminum tungsten inert gas weld metals: using carbon nanotube/aluminum composite as a filler metal, Micron 54-55 (2013) 28–35.

[18] M. Fattahi, V. Noei Aghaei, A.R. Dabiri, S. Amirkhanlou, S. Akhavan, Y. Fattahi, Novel manufacturing process of nanoparticle/Al composite filler metals of tungsten inert gas welding by accumulative roll bonding, Materials Science and Engineering: A 648 (2015) 47–50.

[19] M. Fattahi, M. Rostami, F. Amirkhanlu, N. Arabian, E. Ahmadi, H. Moayedi, Fabrication of aluminum TIG welding filler rods reinforced by ZrO2/reduced graphene oxide hybrid nanoparticles via accumulative roll bonding, Diamond and Related Materials 99 (2019) 107518.

[20] K.R. Ramkumar, S. Natarajan, Tensile properties and strengthening effects of Al 3003 alloy weldment reinforced with TiO2 nanoparticles, Composites Part B: Engineering 175 (2019) 107159.

[21] H. Choi, W.-h. Cho, H. Konishi, S. Kou, X. Li, Nanoparticle-Induced Superior Hot Tearing Resistance of A206 Alloy, Metall and Mat Trans A 44 (2013) 1897–1907.

[22] C. Ma, L. Chen, C. Cao, X. Li, Nanoparticle-induced unusual melting and solidification behaviours of metals, Nature communications 8 (2017) 14178.

[23] R.R. Ambriz and V. Mayagoitia, Welding of Aluminum Alloys, Recent Trends in Processing and Degradation of Aluminium Alloys: http://www.intechopen.com/books/recent-trends-in-processing-and-degradation-of-aluminium-alloys/weldingof-aluminum-alloys, in: M.T. Shaw, W.J. MacKnight (Eds.), Introduction to Polymer Viscoelasticity, John Wiley & Sons, Inc, Hoboken, NJ, USA, 2005, pp. 1–6.

[24] G. Mathers, The welding of aluminium and its alloys, CRC Press; Cambridge Woodhead Publishing, Boca Raton, Fla., 2002.

[25] S. Kou, Welding metallurgy, 2nd ed., Wiley, New Jersey, 2003.

[26] T. Fukuda, Weldability of 7000 series aluminium alloy materials, Welding International 26 (2012) 256–269.

[27] T. Böllinghaus, H. Herold (Eds.), Hot Cracking Phenomena in Welds, Springer-Verlag Berlin Heidelberg, 2005.

[28] J.C. Lippold, Welding Metallurgy and Weldability, Hoboken, New Jersey, 2015.

[29] D.G. Eskin, Suyitno, L. Katgerman, Mechanical properties in the semi-solid state and hot tearing of aluminium alloys, Progress in Materials Science 49 (2004) 629–711.

[30] J.C. Borland, Generalized Theory of Super-Solidus Cracking in Welds (and Castings), British Welding Journal 4 (1960).

[31] F. Matsuda, H. NAKAGAWA, S. OGATA, S. Katayama, Fractographic Investigation on Solidification Crack in the Varestraint Test of Fully Austenitic Stainless Steel Studies on Fractography of Welded Zone (III), Transactions of JWRI (1978) 59–70.

[32] N.N. Prokhorov, The technological strength of metals while crystallising during welding. Doc IX-479-65, 1965., Welding Production 9 (1965) 1–8.

[33] U. Feurer, Influence of alloy composition and solidification conditions on dendrite arm spacing, feeding and hot tearing properties of aluminium alloys., Proceedings International Symposium on Engineering Alloys (1977) 131–145.

[34] D. Manitsas, J. Andersson, S. Pantelakis, S. Koubias, Hot Cracking Mechanisms in Welding Metallurgy, MATEC Web Conf. 188 (2018) 3018.

[35] M. Rappaz, J.-M. Drezet, M. Gremaud, A New Hot-Tearing Criterion, Metallurgical and Materials Transactions A 30 (1999) 449–455.

[36] N. Wang, S. Mokadem, M. Rappaz, W. Kurz, Solidification cracking of superalloy single- and bi-crystals, Acta Materialia 52 (2004) 3173–3182.

[37] C. Huang, G. Cao, S. Kou, Liquation Cracking in Aluminum Welds, MSF 539-543 (2007) 4036–4041.

[38] J.C. Lippold, T. Böllinghaus, C.E. Cross (Eds.), Hot Cracking Phenomena in Welds III, 2011.

[39] C. Huang, S. Kou, Liquation Cracking in Full-Penetration AI-Mg-Si Welds, Welding Journal 84 (2004) 111–122.

[40] A.J. Ramirez, J.C. Lippold, High temperature behavior of Ni-base weld metal, Materials Science and Engineering: A 380 (2004) 259–271.

[41] M.G. Collins, J.C. Lippold, An investigation of ductility dip cracking in nickel-based filler materials-Part I, Welding Journal 82 (2003).

[42] G.D. Janaki Ram, T.K. Mitra, V. Shankar, S. Sundaresan, Microstructural refinement through inoculation of type 7020 Al–Zn–Mg alloy welds and its effect on hot cracking and tensile properties, Journal of Materials Processing Technology 142 (2003) 174–181.

[43] J.L. Dossett, G.E. Totten, Properties and Selection: Nonferrous Alloys and Special-Purpose Materials, 10th ed., ASM International, Materials Park, Ohio, 1990.

[44] W. Stopyra, K. Gruber, I. Smolina, T. Kurzynowski, B. Kuźnicka, Laser powder bed fusion of AA7075 alloy, Additive Manufacturing (2020) 101270.

[45] Q.L. Bai, Y. Li, H.X. Li, Q. Du, J.S. Zhang, L.Z. Zhuang, Roles of Alloy Composition and Grain Refinement on Hot Tearing Susceptibility of 7××× Aluminum Alloys, Metall and Mat Trans A 47 (2016) 4080–4091.

[46] D. Warrington, D.G. Mccartney, Hot-cracking in Aluminium Alloys 7050 and 7010—a Comparative Study, Cast Metals 3 (2016) 202–208.

[47] M. EASTON, H. Wang, J. Grandfield, D. St John, E. Sweet, An analysis of the effect of grain refinement on the hot tearing of aluminium alloys., Materials forum 28 (2004) 224–229.

[48] G. Timelli, G. Camicia, S. Ferraro, Effect of Grain Refinement and Cooling Rate on the Microstructure and Mechanical Properties of Secondary Al-Si-Cu Alloys, J. of Materi Eng and Perform 23 (2014) 611–621.

[49] M. Dehnavi, M. Haddad-Sabzevar, M.H. Avazkonnadeh-Gharavol, Cooling curve analysis in binary Al-Cu alloys, Metall Mater Eng 21 (2015) 207–222.

[50] S. Dev, A.A. Stuart, R.R.D. Kumaar, B.S. Murty, K.P. Rao, Effect of scandium additions on microstructure and mechanical properties of Al–Zn–Mg alloy welds, Materials Science and Engineering: A 467 (2007) 132–138.

[51] V.I. Elagin, V.V. Zakharov, T.D. Rostova, Effect of scandium on the structure and properties of alloy Al-5.5% Zn-2.0% Mg, Metal Science and Heat Treatment 36 (1994) 375–380.

[52] M.G. Mousavi, C.E. Cross, Ø. Grong, Effect of scandium and titanium–boron on grain refinement and hot cracking of aluminium alloy 7108, Science and Technology of Welding and Joining 4 (2013) 381–388.

[53] G. Madhusudhan Reddy, A.K. Mukhopadhyay, A. Sambasiva Rao, Influence of scandium on weldability of 7010 aluminium alloy, Science and Technology of Welding and Joining 10 (2013) 432–441.

[54] N. Qbau, N.D. Nam, N.X. Ca, N.T. Hien, The crack healing effect of scandium in aluminum alloys during laser additive manufacturing, Journal of Manufacturing Processes 50 (2020) 241–246.

[55] W. Wang, Y. Pranolo, C.Y. Cheng, Metallurgical processes for scandium recovery from various resources, Hydrometallurgy 108 (2011) 100–108.

[56] N. Coniglio, C.E. Cross, Mechanisms for Solidification Crack Initiation and Growth in Aluminum Welding, Metall and Mat Trans A 40 (2009) 2718–2728.

[57] P. Berube, Weldability of Aluminum Alloys, Aluminum Science and Technology 2 (2018).

[58] T.S. Srivatsan, T.S. Sudarshan, Welding of Lightweight Aluminum-Lithium Alloys, Welding Journal 70 (1991) 173–184.

[59] N. Coniglio, C.E. Cross, T. Michael, Lammers M., Defining a Critical Weld Dilution to Avoid Solidification Cracking in Aluminum, Welding Journal 87 (2008) 237-s.

[60] N. B. POTLURI, P. K. GHOSH, P. C. GUPTA AND Y. S. REDDY, Studies on Weld Metal Characteristics and Their Influence on Tensile and Fatigue Properties of Pulsed-Current GMA Welded AI-Zn-Mg Alloy.

[61] S. Kou, Y. Le, Grain structure and solidification cracking in oscillated arc welds of 5052 aluminum alloy, MTA 16 (1985) 1345–1352.

[62] N. S. Biradar, Effect of transverse mechanical arc oscillation on hot cracking (solidification & liquation) and weld metal properties of AA2014 T6 TIG welds, AIMS Materials Science 3 (2016) 1544–1560.

[63] V. Balasubramanian, V. Ravisankar, G.M. Reddy, Effect of pulsed current and post weld aging treatment on tensile properties of argon arc welded high strength aluminium alloy, Materials Science and Engineering: A 459 (2007) 19–34.

[64] V. Balasubramanian, V. Ravisankar, G. Madhusudhan Reddy, Influences of pulsed current welding and post weld aging treatment on fatigue crack growth behaviour of AA7075 aluminium alloy joints, International Journal of Fatigue 30 (2008) 405–416.

[65] Marcos PEREITA, Célio TANIGUCHI, Sérgio D. BRANDI, Susumu MACHIDA, Analysis of Solidification Cracks in Welds of Al-Mg-Si A6351 Type Alloy Welded by High Frequency Pulsed TIG Process, QUARTERLY JOURNAL OF THE JAPAN WELDING SOCIETY 12 (1994) 342–350.

[66] Y.P. Yang, P. Dong, J. Zhang, X. Tian, Hot-cracking mitigation technique for welding high-strength aluminum alloy, Welding Journal 79 (1999) 9–17.

[67] C.C. Doumanidis, D.E. Hardt, Simultaneous in-process control of heat affected zone and cooling rate during arc welding, Welding Journal 69 (1990) 186s-196s.

[68] G.M. Goodwin, Test methods for evaluating hot cracking: Review and perspective, 1. U.S.-Japan symposium on advances in welding metallurgy; 1. United States - Japan symposium on advances in welding metallurgy, Yokohama (Japan) (1990).

[69] T. Nelson, J.C. Lippold, W.A. Baeslack, W. Lin, Evaluation of the circular patch test for assessing weld solidification Cracking, part I - Development of a test method, Welding Journal 76 (1997) 111–119.

[70] J.J. Vagi, R.P. Meister, Weldment Evaluation Methods, Columbus, Ohio, 1968.

[71] P.T. Houldcroft, A simple cracking test for use with argon-arc welding., ritish Welding Journal 2 (1955) 471–475.

[72] S. Lampman (Ed.), Weld Integrity and Performance, 1997.

[73] M. KATOH, K. NISHIO, S. MUKAE, A Comparison of the Conventional and Reverse Houldcroft Type Hot Cracking Tests in A5052 Aluminum Alloy Sheet, Quarterly Journal of Japan Welding Society 12 (1994) 179–185.

[74] C.D. Lundin, W.F. Savage, Varestraint test(Varestraint test used to evaluate base metal weldability and influence of particular welding process and welding variables on hot cracking)., Welding International 44 (1965).

[75] M. Thomas, F. Vollert, J. Weidemann, J. Gibmeier, A. Kromm, T. Kannengießer, Surface- and volume-based investigation on influences of different Varestraint testing parameters and chemical compositions on solidification cracking in LTT filler metals, Weld World 64 (2020) 913–923.

[76] F. Vollert, M. Thomas, A. Kromm, J. Gibmeier, Solidification Cracking Assessment of LTT Filler Materials by Means of Varestraint Testing and μCT, Materials (Basel, Switzerland) 13 (2020).

[77] Y. Arata, F.K. Matsuda, Sasaki Ichiro, Solidification Crack Susceptibility of Aluminum Alloy Weld Metals (Report I) Characteristics of Ductility Curves during Solidification by Means of the Trans-Varestraint Test, JWRI 5 (1976).

[78] Fraunhofer-Gesellschaft, New process to prevent cold cracking in high-strength steel, physics.org (SEPTEMBER 6, 2012), SEPTEMBER 6, 2012. phys.org/news/2012-09-cold-high-strength-steel.html.

[79] S. Moeinifar, A.H. Kokabi, H.R.M. Hosseini, Effect of tandem submerged arc welding process and parameters of Gleeble simulator thermal cycles on properties of the intercritically reheated heat affected zone, Materials & Design 32 (2011) 869–876.

[80] L.-Y. Chen, J.-Q. Xu, H. Choi, M. Pozuelo, X. Ma, S. Bhowmick, J.-M. Yang et al., Processing and properties of magnesium containing a dense uniform dispersion of nanoparticles, Nature 528 (2015) 539–543.

[81] G. Cao, H. Choi, H. Konishi, S. Kou, R. Lakes, X. Li, Mg–6Zn/1.5%SiC nanocomposites fabricated by ultrasonic cavitation-based solidification processing, J Mater Sci 43 (2008) 5521–5526.

[82] G. Cao, H. Konishi, X. Li, Mechanical properties and microstructure of SiC-reinforced Mg-(2,4)Al-1Si nanocomposites fabricated by ultrasonic cavitation based solidification processing, Materials Science and Engineering: A 486 (2008) 357–362.

[83] M. Estruga, L. Chen, H. Choi, X. Li, S. Jin, Ultrasonic-assisted synthesis of surface-clean TiB2 nanoparticles and their improved dispersion and capture in Al-matrix nanocomposites, ACS applied materials & interfaces 5 (2013) 8813–8819.

[84] S. Jia, Y. Xuan, L. Nastac, P.G. Allison, T.W. Rushing, Microstructure, mechanical properties and fracture behavior of 6061 aluminium alloy-based nanocomposite castings fabricated by ultrasonic processing, International Journal of Cast Metals Research 29 (2016) 286–289.

[85] Y. Xuan, L. Nastac, The role of ultrasonic cavitation in refining the microstructure of aluminum based nanocomposites during the solidification process, Ultrasonics 83 (2018) 94–102.

[86] S.C. Tjong, Novel Nanoparticle-Reinforced Metal Matrix Composites with Enhanced Mechanical Properties, Adv. Eng. Mater. 9 (2007) 639–652.

[87] R. Lee-Desautels, Theory of van der Waals forces as applied to particlate materials, Educ. Reso. for Part. Techn 51 (2005) 1–5.

[88] J.N. Israelachvili, Intermolecular and Surface Forces: Revised Third Edition, 3rd ed., Elsevier Science, Burlington, 2011.

[89] L. Bergstrom, A. Meurk, H. Arwin, D.J. Rowcliffe, Estimation of Hamaker Constants of Ceramic Materials from Optical Data Using Lifshitz Theory, Journal of the American Ceramic Society 79 (1996).

[90] Yousefian, R., Emadoddin, E., & Baharnezhad, S., Manufacturing of the aluminum metal-matrix composite reinforced with micro-and nanoparticles of TIO2 through accumulative roll bonding process (ARB), Reviews on Advanced Materials Science 55 (2018).

[91] R. Casati, J. Fiocchi, A. Fabrizi, N. Lecis, F. Bonollo, M. Vedani, Effect of ball milling on the ageing response of Al2618 composites reinforced with SiC and oxide nanoparticles, Journal of Alloys and Compounds 693 (2017) 909–920.

[92] Z. Li, G. Fan, Z. Tan, Q. Guo, D. Xiong, Y. Su, Z. Li et al., Uniform dispersion of graphene oxide in aluminum powder by direct electrostatic adsorption for fabrication of graphene/aluminum composites, Nanotechnology 25 (2014) 325601.

[93] H.-m. DING, X.-f. LIU, Influence of Si on stability of TiC in Al melts, Transactions of Nonferrous Metals Society of China 21 (2011) 1465–1472.

[94] A. Javadi, C. Cao, X. Li, Manufacturing of Al-TiB 2 Nanocomposites by Flux-Assisted Liquid State Processing, Procedia Manufacturing 10 (2017) 531–535.

[95] A. Javadi, S. Pan, X. Li, Fabrication of High Strength Al Nanocomposites with Populous TiB2 Nanoparticles, Procedia Manufacturing 26 (2018) 629–632.

[96] S. Lei, X. Li, Y. Deng, Y. Xiao, Y. Chen, H. Wang, Microstructure and mechanical properties of electron beam freeform fabricated TiB2/Al-Cu composite, Materials Letters 277 (2020) 128273.

[97] Z. Li, D. Chen, H. Wang, E.J. Lavernia, A. Shan, Nano-TiB 2 reinforced ultrafine-grained pure Al produced by flux-assisted synthesis and asymmetrical rolling, J. Mater. Res. 29 (2014) 2514–2524.

[98] C. Xia, J. Huang, J. Tao, S. Wang, L. Cai, M. Wang, D. Chen et al., The Preparation and Properties of the Brown Film by Micro-arc Oxidized on In-Situ TiB2/7050Al Matrix Composites, Coatings 10 (2020) 615.

[99] H. Yang, S. Tian, T. Gao, J. Nie, Z. You, G. Liu, H. Wang et al., High-temperature mechanical properties of 2024 Al matrix nanocomposite reinforced by TiC network architecture, Materials Science and Engineering: A 763 (2019) 138121.

[100] H. Yang, T. Gao, Y. Wu, H. Zhang, J. Nie, X. Liu, Microstructure and mechanical properties at both room and high temperature of in-situ TiC reinforced Al–4.5Cu matrix nanocomposite, Journal of Alloys and Compounds 767 (2018) 606–616.

[101] R. Arpón, J. Narciso, E. Louis, C. García-Cordovilla, Interfacial reactions in Al/TiC particulate composites produced by pressure infiltration, Materials Science and Technology 19 (2013) 1225–1230.

[102] J. Fjellstedt, A.E.W. Jarfors, L. Svendsen, Experimental analysis of the intermediary phases AlB2, AlB12 and TiB2 in the Al–B and Al–Ti–B systems, Journal of Alloys and Compounds 283 (1999) 192–197.

[103] X. Wang, Q. Han, Relationships of diboride phases in Al–Ti(Zr)–B alloys, Materials Science and Technology 31 (2014) 874–879.

[104] R.G. Lye, E.M. Logothetis, Optical Properties and Band Structure of Titanium Carbide, Phys. Rev. 147 (1966) 622–635.

[105] Y. Wang, J. Shi, X. Deng, S. Lu, Contribution of Different Strengthening Effects in Particulate-Reinforced Metal Matrix Nanocomposites Prepared by Additive Manufacturing (2016) V002T02A047.

[106] N. Hansen, Hall–Petch relation and boundary strengthening, Scripta Materialia 51 (2004) 801–806.

[107] V.C.Nardone, K.M.Prewo, On the strength of discontinuous silicon carbide reinforced aluminum composites, Scripta Metallurgica 20 (1986) 43–48.

[108] C. Cao, L. Chen, J. Xu, J. Zhao, M. Pozuelo, X. Li, Phase control in immiscible Zn-Bi alloy by tungsten nanoparticles, Materials Letters 174 (2016) 213–216.

[109] C. Cao, G. Yao, L. Jiang, M. Sokoluk, X. Wang, J. Ciston, A. Javadi et al., Bulk ultrafine grained/nanocrystalline metals via slow cooling, Science advances 5 (2019) eaaw2398.

[110] E. Guo, A.B. Phillion, Z. Chen, H. Kang, T. Wang, P.D. Lee, In Situ Tomographic Observation of Dendritic Growth in Mg/Al Matrix Composites, in: C. Chesonis (Ed.), Light Metals 2019, Springer International Publishing, Cham, 2019, pp. 1561–1567.

[111] K. Wang, H. Jiang, Q. Wang, B. Ye, W. Ding, A Novel Method to Achieve Grain Refinement in Aluminum, Metall and Mat Trans A 47 (2016) 4788–4794.

[112] H. Choi, H. Konishi, X. Li, Al2O3 nanoparticles induced simultaneous refinement and modification of primary and eutectic Si particles in hypereutectic Al–20Si alloy, Materials Science and Engineering: A 541 (2012) 159–165.

[113] H. Choi, X. Li, Refinement of primary Si and modification of eutectic Si for enhanced ductility of hypereutectic Al–20Si–4.5Cu alloy with addition of Al2O3 nanoparticles, J Mater Sci 47 (2012) 3096–3102.

[114] K. Wang, H.Y. Jiang, Y.W. Jia, H. Zhou, Q.D. Wang, B. Ye, W.J. Ding, Nanoparticle-inhibited growth of primary aluminum in Al–10Si alloys, Acta Materialia 103 (2016) 252–263.

[115] M. Sokoluk, C. Cao, S. Pan, X. Li, Nanoparticle-enabled phase control for arc welding of unweldable aluminum alloy 7075, Nature communications 10 (2019).

[116] L.-Y. Chen, J.-Q. Xu, X.-C. Li, Controlling Phase Growth During Solidification by Nanoparticles, Materials Research Letters 3 (2014) 43–49.

[117] M. Fattahi, M. Abbasi, H. Zalaghi, A. Eynalvandpour, A.R. Dabiri, Y. Fattahi, Reduction of weld metal diffusible hydrogen content by adding colloidal nanosilica to the electrode coating, International Journal of Hydrogen Energy 41 (2016) 13294–13298.

[118] C. Vimalraj, P. Kah, B. Mvola, J. Martikainen, Effect of Nanomaterial Addition Using GMAW and GTAW Processes, Reviews on Advanced Materials Science 44 (2016) 370–382.

[119] D.S. Kartsev, E.A. Zernin, Use of Refractory Nanoparticles as a Component of Welding Materials in Welding and Surfacing With Coated Electrodes and Flux Cored Wires, IOP Conf. Ser.: Mater. Sci. Eng. 142 (2016) 12008.

[120] A.R. Dabiri, R. Yousefi Mojallal, E. Ahmadi, M. Fattahi, S. Amirkhanlou, Y. Fattahi, Effect of ZrO2 nanoparticles on the impact properties of shielded metal arc welds, Materials Letters 158 (2015) 325–328.

[121] C. Chen, H. Xue, H. Peng, L. Yan, L. Zhi, S. Wang, Inclusions and Microstructure of Steel Weld Deposits with Nanosize Titanium Oxide Addition, Journal of Nanomaterials 2014 (2014) 1–7.

[122] K.-H. Tseng, P.-Y. Lin, UNS S31603 Stainless Steel Tungsten Inert Gas Welds Made with Microparticle and Nanoparticle Oxides, Materials 7 (2014) 4755–4772.

[123] M. Fattahi, A. Ghaheri, N. Arabian, F. Amirkhanlu, H. Moayedi, Applying the ultrasonic vibration during TIG welding as a promising approach for the development of nanoparticle dispersion strengthened aluminum weldments, Journal of Materials Processing Technology 282 (2020) 116672.

[124] K.R. Ramkumar, S. Natarajan, Retardation of Grain Growth in Al 3003 Nanocomposite Weldment Using ARB Filler Metal, Met. Mater. Int. 727 (2020) 51.

[125] W. Liu, C. Cao, J. Xu, X. Wang, X. Li, Molten salt assisted solidification nanoprocessing of Al-TiC nanocomposites, Materials Letters 185 (2016) 392–395.

[126] Y. Ma, Z. Chen, M. Wang, D. Chen, N. Ma, H. Wang, High cycle fatigue behavior of the in-situ TiB2/7050 composite, Materials Science and Engineering: A 640 (2015) 350–356.

[127] A.R. KENNEDY, A.E. KARANTZALI, S.M. WYATT, The microstructure and mechanical properties of TiC and TiB2-reinforced cast metal matrix composites, JOURNAL OF MATERIALS SCIENCE (1999).

[128] C. Mallikarjuna, S.M. Shashidhara, U.S. Mallik, K.I. Parashivamurthy, Grain refinement and wear properties evaluation of aluminum alloy 2014 matrix-TiB2 in-situ composites, Materials & Design 32 (2011) 3554–3559.

[129] Z. Chen, T. Wang, Y. Zheng, Y. Zhao, H. Kang, L. Gao, Development of TiB2 reinforced aluminum foundry alloy based in situ composites – Part I, Materials Science and Engineering: A 605 (2014) 301–309.

[130] ASM International. Handbook Committee, ASM Handbook: Heat Treating of Aluminum Alloys, 1991.

[131] L. Gao, Y. Harada, S. Kumai, Microstructural characterization of aluminum alloys using Weck's reagent, part I, Materials Characterization 107 (2015) 426–433.

[132] T. Anderston, Welding aluminum: Questions and answers a practical guide for troubleshooting aluminum welding-related problems, 2nd ed., Americal Welding Society, Miami, FL, 2010.

[133] C.D. Ridgeway, C. Gu, A.A. Luo, Predicting primary dendrite arm spacing in Al–Si–Mg alloys, J Mater Sci 54 (2019) 9907–9920.

[134] F. Liu, X. Zhu, S. Ji, Effects of Ni on the microstructure, hot tear and mechanical properties of Al–Zn–Mg–Cu alloys under as-cast condition, Journal of Alloys and Compounds 821 (2020) 153458.

[135] G.M. Reddy, A.A. Gokhale, K. Prasad Rao, Effect of filler metal composition on weldability of Al-Li alloy 1441, Science and Technology of Welding and Joining 3 (2013) 151–158.

[136] T. Böllinghaus, H. Herold, C.E. Cross, J.C. Lippold, Hot Cracking Phenomena in Welds II, 1st ed., Springer-Verlag, s.l., 2008.

[137] V. Anjos, R. Deike, C.S. Ribeiro, The use of thermal analysis to predict the dendritic coherency point on nodular cast iron melts, Ciência & Tecnologia dos Materiais 29 (2017) e27-e33.

[138] M.B. Djurdjevic, J.H. Sokolowski, Z. Odanovic, Determination of dendrite coherency point characteristics using first derivative curve versus temperature, J Therm Anal Calorim 109 (2012) 875–882.

[139] N. Coniglio, Aluminium alloy weldability: Identification of weld solidification cracking mechanisms through novel experiment technique and model development. Zugl.: Magdeburg, Univ., Fak. für Maschinenbau, Diss., 2008, Bundesanstalt für Materialforschung und -prüfung (BAM), Berlin.

[140] T. Böllinghaus, J. Lippold, C.E. Cross (Eds.), Hot Cracking Phenomena in Welds III: [This conference was the third in a series of workshops that started in 2004 … the third workshop was held in Columbus, Ohio in March 2010 and hosted by The Ohio State University and Edison Welding Institute ;

dedicated in memory of Prof. Dr.-Ing. habil. Dr. E. h. Horst Herold], Springer-Verlag Berlin Heidelberg, Berlin, Heidelberg, 2011.

[141] Veldman, N. L., Dahle, A. K., StJohn, D. H., & Arnberg, L., Dendrite coherency of Al-Si-Cu alloys, Metallurgical and Materials Transactions A 32 (2001) 147–155.

[142] A.H. Ahmad, S. Naher, D. Brabazon, Thermal Profiles and Fraction Solid of Aluminium 7075 at Different Cooling Rate Conditions, Key Engineering Materials (2013).

[143] K.D. Carlson, C. Beckermann, Determination of solid fraction–temperature relation and latent heat using full scale casting experiments, International Journal of Cast Metals Research 25 (2013) 75–92.

[144] S. Farahany, M.H. Idris, A. Ourdjini, F. Faris, H. Ghandvar, Evaluation of the effect of grain refiners on the solidification characteristics of an Sr-modified ADC12 die-casting alloy by cooling curve thermal analysis, J Therm Anal Calorim 119 (2015) 1593–1601.

[145] J.W. Gibbs, P.F. Mendez, Solid fraction measurement using equation-based cooling curve analysis, Scripta Materialia 58 (2008) 699–702.

[146] D. Larouche, C. Laroche, M. Bouchard, Analysis of differential scanning calorimetric measurements performed on a binary aluminium alloy, Acta Materialia 51 (2003) 2161–2170.

[147] D. Zhang, H.V. Atkinson, H. Dong, Q. Zhu, Differential Scanning Calorimetry (DSC) and Thermodynamic Prediction of Liquid Fraction vs Temperature for Two High-Performance Alloys for Semi-Solid Processing (Al-Si-Cu-Mg (319s) and Al-Cu-Ag (201)), Metall and Mat Trans A 48 (2017) 4701–4712.

[148] D.M. Stefanescu, Science and Engineering of Casting Solidification, 2015.

[149] P. Marchwica, J.H. Sokolowski, W.T. Kierkus, Fraction solid evolution characteristics of AlSiCu alloys - dynamic baseline approach, Journal of Achievements in Materials of Achievements in Materials and Manufacturing Engineering and Manufacturing Engineering 47 (2011) 115–136.

[150] S.G. Shabestari, M. Malekan, Assessment of the effect of grain refinement on the solidification characteristics of 319 aluminum alloy using thermal analysis, Journal of Alloys and Compounds 492 (2010) 134–142.

[151] G. Mrówka-Nowotnik, J. Sieniawski, Analysis of Intermetallic Phases in 2024 Aluminium Alloy, SSP 197 (2013) 238–243.

[152] A. Boag, A.E. Hughes, A.M. Glenn, T.H. Muster, D. McCulloch, Corrosion of AA2024-T3 Part I, Corrosion Science 53 (2011) 17–26.

[153] G. Mrówka-Nowotnik, J. Sieniawski, M. Wierzbińska, Analysis of intermetallic particles in AlSi1MgMn aluminium alloy, Journal of Achievements of Materials and Manufacturing Engineering 20 (2006).

[154] S.N. Samaras, G.N. Haidemenopoulos, Modelling of microsegregation and homogenization of 6061 extrudable Al-alloy, Journal of Materials Processing Technology 194 (2007) 63–73.

[155] J.Q. Xu, L.Y. Chen, H. Choi, X.C. Li, Theoretical study and pathways for nanoparticle capture during solidification of metal melt, Journal of physics. Condensed matter an Institute of Physics journal 24 (2012) 255304.

[156] J. Lippold, T. Böllinghaus, C.E. Cross (Eds.), Hot Cracking Phenomena in Welds III: [This conference was the third in a series of workshops that started in 2004 … the third workshop was held in Columbus, Ohio in March 2010 and hosted by The Ohio State University and Edison Welding Institute ; dedicated in memory of Prof. Dr.-Ing. habil. Dr. E. h. Horst Herold], Springer-Verlag Berlin Heidelberg, Berlin, Heidelberg, 2011.

[157] L. Bäckerud, E. Król, J. Tamminen, Solidification Characteristics of AluminiumAlloys, Vol. 1., Skanaluminium, Oslo, 1986.

Attachments

Attachment A: XRD-analysis of extruded filler metal

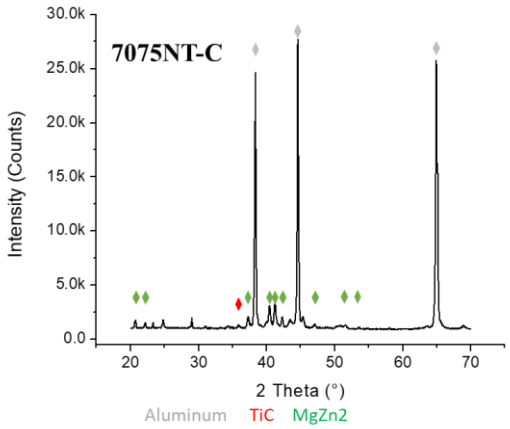

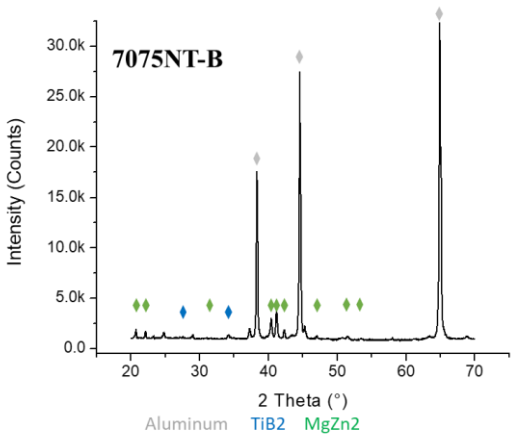

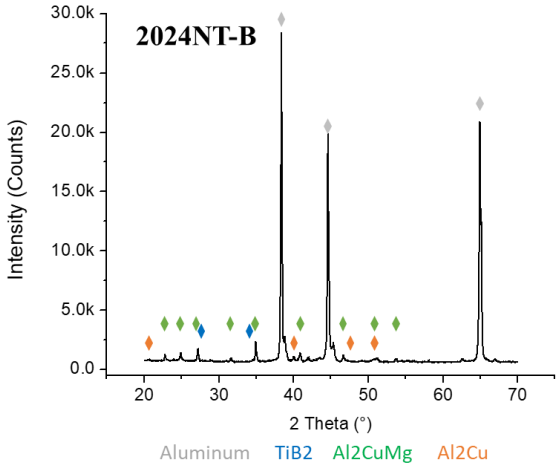

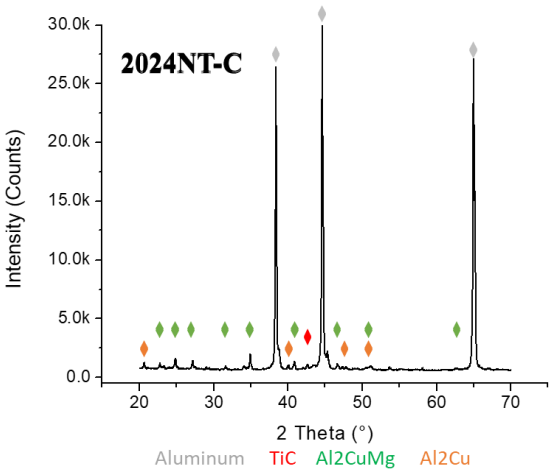

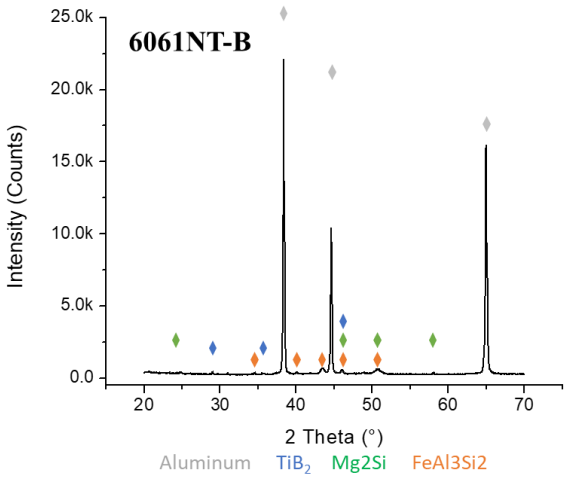
6061NT-B
Intensity (Counts)
25.0k
20.0k
15.0k
10.0k
5.0k
0.0
20
30
40
50
60
70
2 Theta (°)
Aluminum
TiB2
Mg2Si
FeAl3Si2

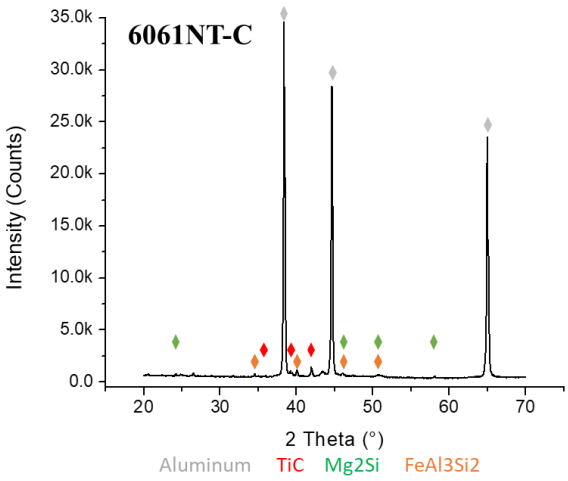
6061NT-C
Intensity (Counts)
35.0k
30.0k
25.0k
20.0k
15.0k
10.0k
5.0k
0.0
20
30
40
50
60
70
2 Theta (°)
Aluminum
TiC
Mg2Si
FeAl3Si2

Attachment B: Hobart filler metal selection chart